ABSTRACT

Title of Dissertation: STUDIES OF ULTRAFAST PROCESSES IN THIN FILM HIGH TEMPERATURE SUPERCONDUCTOR AND FERROELECTRIC MATERIAL

Jinjin Li, Doctor of Philosophy, 2004

Dissertation directed by: Professor Chi H. Lee

Department of Electrical & Computer Engineering

This Ph.D. thesis covers two projects, namely the study of optical responses of high temperature superconductor thin films and the study of polarization switching dynamics in ferroelectric materials, both using a femtosecond laser.

We employed the improved Transient Photoimpedance Response method with high signal-to-noise ratio to conduct systematic investigations of the dependence of femtosecond optical responses of YBCO films on current, average laser power, temperature, and film thickness. All of the physical processes embedded in the optical responses were observed. Feature waveforms associated with different physical processes, namely the kinetic inductance, 2-T, and thermal model, were obtained. Taking advantage of the direct relationship between the optical response and the Cooper pair breaking rate, we studied the photon energy dependence of the fast optical response of YBCO films. A resonance around 1.5 eV was observed with a total width of ~100 meV. This narrowness of a spectrum-width has not been reported in the literature. The results

are well interpreted by stripe phase theory. We also developed a superconducting sampling gate to perform the *electrical* correlation measurement of the fast optical response of YBCO films. An estimated ~8 ps pulse was obtained.

For the application of ferroelectric materials as high-speed nonvolatile random access memories, the issue of how fast the polarization can be switched is of great importance. The goal of our research is to obtain the intrinsic polarization switching time. By simulating the pulse method utilized in our experiments, we concluded that the rise-time of the input electric pulse and the capacitor size are two limiting factors of this method. We therefore proposed and realized a novel approach for generating jitter-free, sub-100 ps rise-time step-function-like electric pulses, using a femtosecond laser-activated semiconductor photoconductive switch. Quantitative measurements yielded a polarization switching time t_s of ~220 ps for a 4.5×5.4 μm^2 PNZT capacitor, which is to our knowledge the fastest one ever reported. Modeling of the switching transient using the Ishibashi-Merz model gave a characteristic switching time t_0 of ~70 ps. Moreover, polarization switching behaviors for various sizes of capacitors and various rise-times of input electric pulses were also investigated.

STUDIES OF ULTRAFAST PROCESSES IN THIN FILM HIGH TEMPERATURE SUPERCONDUCTOR AND FERROELECTRIC MATERIAL

by

Jinjin Li

Dissertation submitted to the Faculty of the Graduate School of the
University of Maryland at College Park in partial fulfillment
of the requirement for the degree of
Doctor of Philosophy
2004

Advisory Committee:

Professor Chi. H. Lee, Chairman/Advisor
Professor Julius Goldhar
Professor Robert Newcomb
Professor Christopher Davis
Professor Lourdes Salamanca-Riba

ACKNOWLEDGEMENTS

I would like to express my sincere thanks to my dissertation advisor, Prof. Chi H. Lee, for giving me the opportunity to work in his group and for his guidance and support throughout this thesis work. I will always remember his good advice and constructive criticism. Above all, his devotion to knowledge and creation, and his never-satisfied desire for perfection are truly invaluable for my future career as a researcher.

I would like to thank Prof. Ramesh for his guidance and technical insight throughout the ferroelectrics project. His enthusiasm for research will always inspire me.

I would like to thank Prof. Venkatesan and Eric Li in the Superconductor Research Center for providing me with the superconductor samples and the good ideas as well.

I would like to thank Dr. Weilou Cao for training me and helping me in my research. I would like to thank Hongye Liang for his support and for the fruitful discussions during the experiments. I would like to thank Junghwan Kim for teaching me and helping me on the clean room techniques. I would like to thank Michael Bowen for revising my paper. Special thanks to Min Du for her encouragement and support during my Ph.D. study. I would like to thank those whom I have worked with during my graduate research work in Prof. Lee's group including Amr Safwat, Sukanya Tachatraiphop, Yonggu Kim, Alen Lo and Yi-Hsing Peng.

I would like to thank Zhengkun Ma and Tong Zhao in the Material Research Science and Engineering Center who helped me cut and anneal the PZT samples.

I would like to thank all my friends who made my life in a foreign country colorful and enjoyable.

I would like to thank my family for their encouragement and support during my Ph.D studies.

TABLE OF CONTENTS

LIST OF FIGURES……..viii

Chapter 1 General Introduction 1

1.1 Ultrafast Processes in Materials 1

1.2 Contributions 5

1.3 Organization of the Thesis 6

Chapter 2 Introduction to the Ultrafast Optical Response of Thin Film High Temperature Superconductor 7

2.1 Introduction to Superconductivity 7

2.1.1 Superconductivity 7

2.1.2 Research Development of Superconductors 10

2.1.3 $YBa_2Cu_3O_{7-\delta}$ 12

2.2 Study of the Optical Response of YBCO Films and its Motivation 13

Chapter 3 Experimental Techniques: Femtosecond Laser System, Superconductor Device Preparation, and Experimental Setup 16

3.1 Femtosecond Laser System 16

3.2 Thin Film Deposition 27

3.3 Device Design 30

3.4 Device Fabrication 34

3.5 Experimental Setup 35

Chapter 4 Study of the Optical Response of YBCO Thin Films 40

4.1 Theoretical Background of Optical Response 40

4.1.1 Qualitative Description of the Physical Mechanisms Inherent in the Optical Response 41
4.1.2 Theoretical Models for Optical Response..... 46
4.2 Optical Response of YBCO Films with Various Thicknesses..... 57
4.2.1 Waveforms of the Optical Response in YBCO Thin Films..... 57
4.2.2 Current Dependence of the Optical Response 69
4.2.3 Power Dependence of the Optical Response 70
4.2.4 Temperature Dependence of the Optical Response 76
4.3 Photon Energy Dependence of the Fast Optical Response of YBCO Films 80
4.3.1 Motivation..... 80
4.3.2 Experimental Results 82
4.3.3 Discussion..... 84
4.4 Pump-probe Correlation Measurement of the Fast Optical Response of YBCO Films 89
4.4.1 Introduction..... 89
4.4.2 Theory and Experimental Arrangement..... 94
4.4.3 Experimental Results 98
4.4.4 A Potential Application of the Superconductor Sampling switch 100
4.5 Application of a Superconductor Opening Switch to a Current Charged Transmission Line (CCTL) System 102

Chapter 5 Conclusion and Future Work on the Study of the Optical Response of High Temperature Superconductor Materials 109
Chapter 6 Introduction to the Ultrafast Polarization Switching in Thin Film Ferroelectrics 115
6.1 Introduction to Ferroelectricity 115
6.2 Application of Ferroelectric Thin Films to Non-volatile Memory Devices 121
6.2.1 Ferroelectrics as a Non-volatile Memory Device 121
6.2.2 History of the Development of the FeRAM 123
6.3 Study of Polarization Switching Dynamics in Ferroelectrics 126
6.4 Motivation and Organization 129
Chapter 7 Study of the Polarization Switching Dynamics of PNZT Ferroelectric Thin Film Capacitors 132
7.1 Pulse Method and Its Simulation 132
7.2 Experimental Techniques 140
7.2.1 Thin Film Preparation with Sol-gel Technique 140
7.2.2 Experimental Setup 143
7.3 Physical Models for the Dynamic Properties of the Polarization Switching Process of Ferroelectrics 148
7.3.1 Ishibashi-Merz Model 148
7.3.2 Shur Model 153
7.3.3 Calculation of $f(t)$ from Experimental Data 156
7.4 Experimental Results 157

7.4.1 The ≅ 220 ps Polarization Switching Time for a 4.5×5.4 μm^2 PNZT Capacitor 157

7.4.2 Impact of the Capacitor Area on the Measurement 163

7.4.3 Impact of the Rise-time of the Input Step-like Electric Pulse on the Measurement 167

7.4.4 Activation field 171

Chapter 8 Conclusion and Future Work on the Study of Polarization Switching Dynamics of Ferroelectric Thin Film Capacitors 175

Appendix A: Runga-Kutta ……179

Appendix B: Derivation of Initial Condition for R-T Equation Simulation…….181

Appendix C: Derivation of Initial Condition for 2-T Equation Simulation……..183

REFERENCES……184

LIST OF FIGURES

Figure 2-1 A typical resistance versus temperature (R-T) curve of a superconductor. 8

Figure 2-2 Crystal structure of $YBa_2Cu_3O_7$. 12

Figure 2-3 Schematic of Cooper pair breaking with laser illumination. 13

Figure 3-1 Schematic of the femtosecond laser system used in this thesis research. 17

Figure 3-2 Schematic of the Mira 900. 19

Figure 3-3 Mira 900 saturable absorber system. 21

Figure 3-4 Operation of wavelength tuning with a birefringent tuning filter. 22

Figure 3-5 Schematic of the RegA 9000. 23

Figure 3-6 Simplified functional diagram of an AO modulator Bragg cell. 24

Figure 3-7 Schematic of double-pass cavity dumping. 25

Figure 3-8 Schematic of a pulsed laser deposition (PLD) system. 27

Figure 3-9 Device structure of the coplanar waveguide (CPW). 31

Figure 3-10 Schematic of a CPW device (below) and a real image of a CPW device under an optical microscope (above). 34

Figure 3-11 Experimental setup of the Transient Photoimpedance Response (TPR) method. 37

Figure 3-12 Equivalent circuit of the TPR method. 37

Figure 4-1 A schematic illustration of the Cooper pair density as a function of time [72]. 45

Figure 4-2 A schematic of the interactions between photons, Cooper pairs, quasiparticles, and phonons. 49

Figure 4-3 Numerical simulation of the non-equilibrium kinetic inductance model based on the R-T equations. 51
Figure 4-4 A schematic diagram of heat flow in the two-temperature (2-T) model [82]. 53
Figure 4-5 Numerical simulation of the two-temperature model. 55
Figure 4-6 Optical response waveforms of a 100 nm YBCO thin film at various laser powers. 58
Figure 4-7 Optical response waveforms of a 100 nm YBCO thin film at various temperatures. 59
Figure 4-8 Optical response waveforms of a 100 nm YBCO thin film at various bias currents. 60
Figure 4-9 Optical response waveforms of a 100 nm YBCO thin film at laser power of (a) P = 1.28 mW, (b) P = 2.5 mW and (c) P = 7.26 mW, temperature T = 80 K, bias current I = 1.5 mA. 61
Figure 4-10 Illustration of the pulse broadening due to the finite focusing spot and the limited bandwidth of the oscilloscope. Curve A: The assumed optical response signal after considering the dispersion. Curve B: The optical response signal after considering the 2 mm long finite laser focusing spot. Curve C: The expected signal on an oscilloscope. 63
Figure 4-11 The kinetic inductance induced optical response on oscilloscope: a simulation result and an experimental result. 63
Figure 4-12 Optical response waveforms of a 400 nm YBCO thin film at various laser powers. 65

Figure 4-13 Optical response waveforms of a 100 nm YBCO thin film at various temperatures. 66
Figure 4-14 Optical response waveforms of a 100 nm YBCO thin film at various bias currents. 68
Figure 4-15 A typical optical response waveform of an optically thick YBCO film... 69
Figure 4-16 Current dependence of the 1st peak amplitude of the optical responses of a 100 nm YBCO film. 70
Figure 4-17 Laser power dependence of the 1st and 2nd peak amplitudes of the optical response of a 100 nm YBCO film. 73
Figure 4-18 Laser power dependence of the width of the thermal optical response of a 100 nm YBCO film. 73
Figure 4-19 Laser power dependence of the 1st and 2nd peak amplitudes of the optical response of an YBCO thin film with various film thickness. 74
Figure 4-20 Laser power dependence of the 3rd peak amplitude of the optical response of optically thick YBCO films with various thicknesses. 74
Figure 4-21 Laser power dependence of the widths of the thermal optical response of YBCO thin films with various film thicknesses. 75
Figure 4-22 Time separation between the 1st and 3rd peak for optically thick YBCO films with various film thicknesses. 75
Figure 4-23 Temperature dependence of the 1st peak amplitudes of optical responses of a 100 nm YBCO film. 76

Figure 4-24 Temperature dependence of (a) the 1st peak amplitude, (b) the 1st and 2nd peak amplitudes of the optical response of a 100 nm YBCO film for various laser powers. 78

Figure 4-25 Temperature dependence of the 1st and 2nd peak amplitudes of the optical response of optically thin YBCO films with various thicknesses for laser power (a) P = 7 mW, (b) P = 3 mW. 79

Figure 4-26 Temperature dependence of the 1st and 2nd peak amplitudes of the optical response of optically thick YBCO films with various thicknesses. 80

Figure 4-27 Photon energy dependence of the fast optical response in an 100 nm optimally doped YBCO thin film at (a) 80 K, (b) 60 K and (c) 20 K. 82

Figure 4-28 The Cu-O plane in insulating $YBCO_6$. 86

Figure 4-29 A schematic of doping holes in insulating $YBCO_6$. 87

Figure 4-30 A schematic diagram of the pump-probe technique. 90

Figure 4-31 A schematic of the *all-optic*pump -probe technique. 91

Figure 4-32 A schematic of the *E-O* sampling. 92

Figure 4-33 A schematic of the photoconductive sampling configuration. 94

Figure 4-34 (a) The experimental setup for the electrical correlation measurement of the fast optical response of HTS film. (b) The applied HTS device. 96

Figure 4-35 Output signal on the oscilloscope for two cases. Pump electrical transient is (not) blocked at the probe spot. 97

Figure 4-36 Experimental and fitted V as a function of τ. 99

Figure 4-37 Derivative of $V(\tau)$ with respect to τ. 100

Figure 4-38 A proposed schematic of the optical sampling of integrated electrical devices with superconductor sampling switches. 101
Figure 4-39 A schematic diagram of a CCTL system. 103
Figure 4-40 T-shape CPW device utilized as a monolithic CCTL system. 104
Figure 4-41 (a) A junction with two pieces of transmission lines. (b) A junction with three pieces of transmission lines. 107
Figure 4-42 Illustration of the pulse forming in a CCTL system. 107
Figure 4-43 The short electrical pulse generated by a monolithic CCTL system. 108
Figure 6-1 A schematic hysteresis loop of a ferroelectric material. 116
Figure 6-2 Characteristic Gibbs free energy (G) versus polarization curves for ferroelectrics with a first-order transition in different temperature ranges [15]. 118
Figure 6-3 The cubic perovskite unit cell for $Pb(Zr, Ti)_3$ (PZT) [119]. 119
Figure 6-4 The layered perovskite unit cell for $SrBi_2Ta_2O_9$ (SBT) [119]. 120
Figure 6-5 Basic read/write operation of FeRAMs. 122
Figure 6-6 Illustration of (a) 90° and (b) 180° domain walls. 127
Figure 6-7 Illustration of the polarization switching process in ferroelectrics. 128
Figure 7-1 Equivalent circuit of the ‘pulse method’ 132
Figure 7-2 Illustration of the input positive-positive or positive-negative pulse trains of the pulse method. 133
Figure 7-3 The expected current transients shown on the oscilloscope using the pulse method 134

Figure 7-4 An experimentally obtained hysteresis loop of a thin-film PNZT capacitor. $P^{\wedge}$ and P^{*} correspond to the non-switched and switched polarization respectively. 134

Figure 7-5 Simulated output responses $V(t)$ for various (a) capacitances and (b) rise-times of the input electric pulse $V_{input}(t)$. In (a), the rise-time of the input electric pulse is kept constant at 300 ps. In (b), the capacitance is kept constant at 3×10^{-2} nF..... 137

Figure 7-6 Simulated $\Delta V(t)$ responses for various rise-times of input electric pulses. 139

Figure 7-7 SEM image of a fully integrated PNZT ferroelectric capacitor made with the sol-gel technique. 142

Figure 7-8 (a) Schematic and (b) real image of a semiconductor photoconductive switch device..... 143

Figure 7-9 Principle of a semiconductor photoconductive switch. 144

Figure 7-10 Experimental setup of the pulse method using a Si photoconductive switch as a fast pulse generator. 145

Figure 7-11 Time sequences of pulse trains. 147

Figure 7-12 The area covered by the domain started at point P′ [153]. 148

Figure 7-13 (a) One-dimensional and (b) two-dimensional domain expansions [153]. 150

Figure 7-14 Illustration of the Shur model. 154

Figure 7-15 An input 5 V electric pulse generated by a Si photoconductive switch.. 158

Figure 7-16 Voltage responses of P^*, $P^\wedge$, and ΔP processes for a 4.5×5.4 μm^2 PNZT capacitor. 158

Figure 7-17 Plots of $f(t)$ and its fitting curve using (a) the Ishibashi-Merz and (b) the Shur-Merz model for a 4.5×5.4 μm^2 PNZT capacitor. 159

Figure 7-18 Electric field dependence of t_0 for a 4.5×5.4 μm^2 PNZT capacitor. 159

Figure 7-19 Voltage responses of ΔP processes for various amplitudes of input electric pulses for a 4.5×5.4 μm^2 PNZT capacitor. 160

Figure 7-20 Voltage responses of P*, P^, and ΔP processes for various capacitor areas. The amplitude of the input electric pulse is 6 V. 164

Figure 7-21 Plots of measured (dot line) and fitted (solid line) $f(t)$ curves for various capacitor areas. 165

Figure 7-22 Polarization switching timet_s and characteristic switching time t_0 as functions of capacitor area. The inset shows the front part of the curve. 165

Figure 7-23 Dimensionality n as a function of capacitor area. 166

Figure 7-24 Non-switched polarization (P^), switched polarizaiton (P*), and ΔP as functions of capacitor area. 166

Figure 7-25 Voltage responses of the ΔP process for various rise-times of the input electric pulses for a 12.5×14 μm^2 ferroelectric capacitor. The amplitude of the input electric pulse is 5V. 169

Figure 7-26 Polarization switching timet_s and characteristic switching time t_0 as functions of the rise-time of the input electric pulse for a 12.5×14 μm^2 PNZT capacitor. 169

Figure 7-27 Dimensionality *n* as a function of the rise-time of the input electric pulse for a 12.5×14 μm^2 PNZT capacitor. 170

Figure 7-28 Non-switched polarization (P^), switched polarization (P*), and ΔP as functions of the rise-time of the input electric pulse..... 170

Figure 7-29 Current responses of ΔP processes for various amplitudes of input electric pulses for a 36×32 μm^2 capacitor. The inset shows the plot of $\ln(\Delta i_{max})$ vs. $1/V$ and its linear fitting curve..... 172

Figure 7-30 Current responses of ΔP processes for various amplitudes of input electric pulses for a 22.5×25 μm^2 capacitor. The inset shows the plot of $\ln(\Delta i_{max})$ vs. $1/V$ and its linear fitting curve. 172

Figure 7-31 Current responses of ΔP processes for various amplitudes of input electric pulses for a 6.9×9 μm^2 capacitor. The inset shows the plot of $\ln(\Delta i_{max})$ vs. $1/V$ and its linear fitting curve..... 173

Figure 7-32 Current responses of ΔP processes for various amplitudes of input electric pulses for a 4.5×5.4 μm^2 capacitor. The inset shows the plot of $\ln(\Delta i_{max})$ vs. $1/V$ and its linear fitting curve..... 173

Figure 7-33 Activation field α as a function of capacitor area..... 174

Figure 7-34 $f(t_{peak})$ as a function of capacitor area. 174

Chapter 1 General Introduction

1.1 Ultrafast Processes in Materials

This Ph.D thesis covers two projects: the study of the optical responses of the high temperature superconductor (HTS) thin films and the study of the polarization switching dynamics of ferroelectric materials, both using a femtosecond laser.

A. Study of the optical responses of high temperature superconductor thin films

In this thesis, we systematically study the optical response of YBCO thin films. The optical response of a superconductor refers to the ultrafast voltage transient associated with the Cooper pair breaking process due to the ultrafast laser illumination. The discovery of high temperature superconductors (HTS) [1] has stimulated extensive interest in research on their optical response for two reasons: (a) the potential applications of HTS to broadband photodetectors and opening switches; and (b) the possibility of understanding the fundamental physical mechanisms of HTS, which are still open problems. The material we study in this thesis is the YBCO thin film, which is the only known stable four-element HTS discovered with a transition temperature above the boiling point of liquid nitrogen.

Our approach is based on the Transient Photoimpedance Response (TPR) method [2-6], which utilizes three unique capabilities developed for this study by our laboratory. (1) We design the HTS device in a coplanar waveguide (CPW) transmission line structure to preserve the bandwidth of the propagating transient signal. (2) We utilize a

high bandwidth (20 GHz) digital sampling oscilloscope in the experiment. (3) The high-energy of the femtosecond laser pulses (from the Ti:sapphire regenerative amplifier system) gives a high signal to noise ratio for the detected TPR signals. These unique features allow us to successfully observe the ultrafast optical response signals.

We systematically study the dependence of the optical responses of YBCO films on current (I), average laser power (P), temperature (T) and film thickness. All of the physical processes associated with the optical responses are successfully observed. Under appropriate conditions we obtain the featured waveforms that could be well explained by the kinetic inductance model, the 2-T model, and the thermal model. In addition, it is shown that the optical response waveforms of optically thin films are different from those of optically thick films. For optically thick films, a peak that is assumed to be associated with heat diffusion within the superconductor film emerges. This assumption is validated by the observed dependence of the position of this peak on the film thickness.

The mechanism of the Cooper pair formation in HTS is an unsolved problem. W. A. Little proposed that two electrons could form a Cooper pair by interacting with high-energy excitons instead of phonons [7, 8]. By using thermal-difference reflectance (TDR) spectroscopy, Holcomb *et al*. [8-11] observed the deviation of the ratio of the reflectance in the superconducting state to that in the normal state, R_S/R_N, from unity for photon energies around 1.5 eV. Later in 1997 Stevens *et al.* obtained a similar 1.5 eV spectrum using femtosecond time-resolved spectroscopy [12]. These experiments pointed out the possible existence of the 1.5 eV exciton which is essential in forming the Cooper pair. However, we must note that the physical quantities measured in both experiments are changes of dielectric properties; therefore, the relation of the experimental results to the

electronic pairing mechanism is indirect. On the other hand, our TPR method has the unique feature of the direct detection of the electronic properties of HTS − the Cooper pair breaking rate − with a high signal to noise ratio. Taking advantage of this capability, we conduct the study of the photon-energy dependence of the Cooper pair breaking rate. In our experiment, a ≅ 1.5 eV resonance corresponding to the proposed energy of the exciton in YBCO is observed with a total width of ≅100 meV − the narrowest width that has been reported. Moreover, the experimental data can be well interpreted by the stripe phase theory, in which the metallic and insulating phases coexist in the Cu-O plane of HTS [13, 14].

The speed of the fast optical response transient can theoretically be as fast as picoseconds, however, the optical response transient obtained by the TPR method has a ≅ 50 ps pulse-width due to the limited bandwidth of the measurement system (≅ 20 GHz). To overcome this limitation, we develop a sampling technique using the superconducting sampling gate and perform the *electrical* correlation measurement of the fast optical response transient with this gate. An estimated ≅ 8 ps optical response pulse is obtained.

B. Study of the polarization switching dynamics of ferroelectric thin film capacitors

Faster polarization switching time is a desirable property of a ferroelectric material for non-volatile memory applications. The issue of how fast the polarization can be switched is an essential question that attracts extensive attention. Measurement of the polarization switching time is inevitably limited by the time resolution of the experimental setup. Although the theoretically estimated intrinsic polarization switching time could be ≅ 50 ps [15-19], the fastest polarization switching time previously reported is t_s ≅ 390 ps for PZT samples [20, 21]. The goal of our research in the ferroelectric

project is to systematically study the ultrafast polarization switching dynamics of ferroelectric capacitors and try to obtain the intrinsic polarization switching time.

The method we apply in our research is the pulse method. Systematic simulations of the pulse method clearly illustrate that in order to resolve the intrinsic polarization switching process, an electric pulse with an ultrafast rise-time is a necessity. However, it is difficult to generate such a pulse by electronic means. To overcome this difficulty, in this thesis we propose and demonstrate a novel approach of generating ultrafast rise-time, step-function-like electric pulses using a photon-activated semiconductor photoconductive switch. With this experimental setup, we systematically study the fast polarization switching process in fully integrated ferroelectric $Pb(Nb,Zr,Ti)O_3$ (PNZT) capacitors.

The dependence of the polarization switching behavior on circuit parameters, namely the capacitor area and the rise-time of the input electric pulse, are investigated. The experimental results show good agreement with the simulation. Quantitative measurements yield a polarization switching time, t_s, of ≅ 220 ps for a 4.5×5.4 μm^2 PNZT capacitor, which is to our knowledge, the fastest switching time ever reported. Modeling of this switching transient using the Ishibashi-Merz model gives a characteristic switching time, t_0, (representing the extracted intrinsic polarization switching time from the experimental data) of ≅ 70 ps.

The effects of the circuit parameters on the application of the Ishibashi-Merz model, which relates the experimental results of the pulse method to the domain polarization switching dynamics, are comprehensively examined. It is shown that the extracted characteristic polarization switching time t_0 and the domain growth

dimensionality *n* are certainly circuit parameter dependent. This is true since the experimental results of the pulse method are inevitably convoluted with the circuit parameters. Less circuit influence certainly leads to more accuracy of the obtained domain dynamics.

1.2 Contributions

In summary, the contributions of this thesis work include:

(1) We employ a unique ultrafast optoelectronic technique, with a high signal to noise ratio, to the Transient Photoimpedance Response (TPR) method. With this improved TPR method, we conduct systematic investigation of the dependence of the optical responses of YBCO films on current, average laser power, temperature, and film thickness.

(2) We conduct the investigation of the dependence of the optical responses of YBCO films on photon energy. A resonance of ≅ 1.5 eV is observed with a total width of ≅100 meV, which is to our knowledge the narrowest spectrum line width ever reported.

(3) We propose the concept of the superconductor sampling gate. With such gate, an estimated ≅ 8 ps optical response pulse is obtained.

(4) We propose and realize an experimental setup capable of studying the ultrafast polarization switching dynamics of ferroelectric capacitors. A semiconductor photoconductive switch with femtosecond laser illumination is used as a ‘pulse generator’ to produce jitter free, sub-100psec rise-time, step-function-like electric

pulses. Quantitative measurements yield a polarization switching time, t_s, of ≅ 220 ps, which is to our knowledge the fastest one ever reported.

(5) We examine the pulse method, which is utilized to study the polarization switching process in this thesis, from both simulation and experiment. We systematically study the impact of circuit parameters on the experimental results as well as the fitting parameters (the characteristic switching time t_0, the dimensionality of the domain growth n) of the Ishibashi-Merz model.

1.3 Organization of the Thesis

In this thesis, a femtosecond laser is applied to study: (1) the optical response of the high temperature $YBa_2Cu_3O_{7-\delta}$ superconducting thin films, and (2) the ultrafast polarization switching process in $Pb(Nb_{0.04}Zr_{0.28}Ti_{0.68})O_3$ ferroelectric materials. The research on the HTS is presented in Chapter 2 to Chapter 5, while the research on the ferroelectric material is described in Chapter 6 to Chapter 8. The detailed organization of each part will be presented separately at the beginning of each part.

Chapter 2 Introduction to the Ultrafast Optical Response of Thin Film High Temperature Superconductor

The optical response of a superconductor refers to the generated ultrafast voltage transient resulting from the breaking of Cooper pairs by laser illumination. The goal of our research is to systematically study the optical response of the high temperature superconductor (HTS), in an attempt to understand the mechanism of the HTS, and supply fundamental information for future photodetector applications.

For the sake of completeness, we introduce relevant background information on the optical response of HTS in this chapter. Specifically, this introduction chapter explains the following questions. What is a superconductor? What is the history of its development? What is the optical response of a superconductor? What is the motivation to study the optical response of high temperature superconductor thin films?

2.1 Introduction to Superconductivity

2.1.1 Superconductivity

We introduce the concept of superconductivity by discussing its three basic characteristics: zero resistance, Meissner effect, critical magnetic field and critical current density.

A. Zero resistance

Along with the development of low temperature techniques, where liquefied Helium was obtained in 1908, superconductivity was discovered by H. Kamerlingh Onnes in Leiden, Holland in 1911, where a sudden resistance drop of mercury (Hg) to zero at a critical temperature ≅ 4.2 K was observed [22]. The superconducting state, at which the resistance of the material is zero, is a new form of matter. Later on, superconductivity was also achieved in other metals; for example, the critical temperature of lead was found to be ≅ 7.2 K. Figure 2-1 shows a typical resistance versus temperature (R T) curve of superconductors. T_c, at which the resistance transition occurs, is called transition temperature or critical temperature. And ΔT, within which the transition completes, is called the transition width.

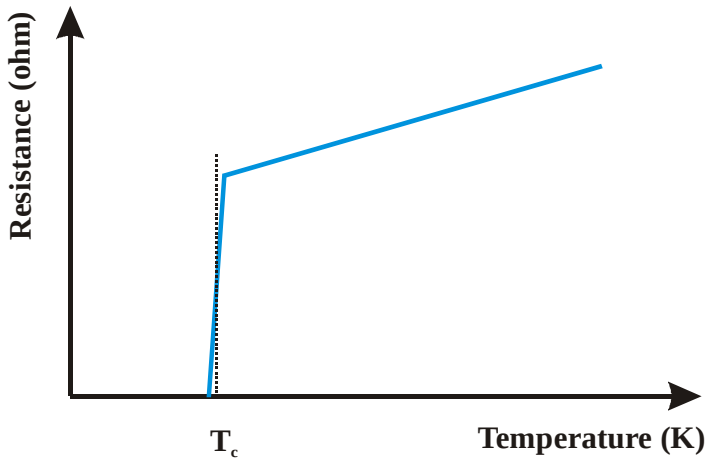

Figure 2-1 A typical resistance versus temperature (R-T) curve of a superconductor.

B. Meissner effect

Superconductivity was treated the same as perfect conductivity until the discovery of the Meissner effect [23]. In 1933, Meissner and Oschsenfeld found that the magnetic field inside a superconductor is zero in the superconducting state. However a magnetic

field inside a perfect conductor can be zero or non-zero because it is the change of magnetic field that is prohibited inside a perfect conductor, or in other words, the magnetic field is conserved. The Meissner effect can be explained with the help of two experiments. In experiment I, one first cools down a perfect conductor to below T_c, then applies a magnetic field to it, and finally removes the applied field. A change of the magnetic field is prohibited. The field is expected not to penetrate the sample since the magnetic field is originally zero. Consequently, the perfect conductor contains no magnetic field inside. In experiment II, a magnetic field is first applied to a perfect conductor, and then cooled down below T_c. Due to the conservation of the magnetic field, the perfect conductor finally does contain a magnetic field inside. Although the final conditions (in terms of temperature and applied magnetic field) of the perfect conductor in both cases are identical, the results are different and history dependent. However, for a superconductor in its superconducting state, independent of history, the magnetic field is zero. This is the Meissner effect. Clearly, except for the zero resistance, a superconductor also possesses special magnetic properties.

C. Critical magnetic field and critical current density

In 1913, H. Kamerlingh Onnes found that when the current density flowing through the superconductor is above a certain value, referred as J_c, the superconductor transits from the superconducting state to the normal state. In other words, superconductivity is destroyed. J_c is called the critical current density, which strongly depends on temperature. It was also found that not only the current density but also the applied magnetic field could destroy the superconductivity by reaching a critical magnetic field, B_c. For a type-I superconductor, there is only one B_c. The superconductor

is in the superconducting state if the applied magnetic field is above B_c, otherwise, it is in the normal state. For a type-II superconductor such as a high temperature superconductor, there are two critical magnetic fields, B_{c1} and B_{c2}. The superconductor is in the superconducting state, vortices state, or normal state when $B_{applied} < B_{c1}$, $B_{c1} < B_{applied} < B_{c2}$, or $B_{applied} > B_{c1}$, respectively.

2.1.2 Research Development of Superconductors

From 1911 to 1986, much effort was directed toward the study of the mechanism of superconductivity. In 1934, Gorter *et al.* proposed the two fluid model to explain the superconductivity [24]. According to this model, electrons inside a superconductor consist of 'normal' electrons and 'super' electrons. At T = 0 K, all electrons behave like super electrons; while at $T = T_c$, all electrons are normal electrons. The fraction of super electrons is temperature dependent and given by

$$\frac{n_s}{n_0} = 1 - (\frac{T}{T_c})^4, \qquad (2.1)$$

where n_s is the density of super electrons and n_0 is the density of total electrons. Super electrons experience no scattering so that the resistance of the material is zero. Based on this model, a superconductor can be represented by two channels in parallel: a superconductive channel and a normal channel. The superconductive channel is represented as an inductor and the normal channel is treated as a conductor. Thus with a *dc* bias, a superconductor shows zero resistance. The remarkable concept of a Cooper pair was brought out by Cooper in 1956 [25], which showed that a pair of electrons with equal moments and opposite spins can be bound together into a new state. The BCS

microscopic theory of superconductivity was established in 1957 [26], which claimed that the superconducting state is a state in which many Cooper pairs exist simultaneously. A minimum energy of $2\Delta(T)$, which can be interpreted as the binding energy between the two electrons of a Cooper pair, is required to break a Cooper pair and create two quasi-particles.

Superconductors were not widely used for practical applications before 1986 because the superconductor transition temperature, T_c, of available superconductors was too low; liquid helium was required to realize superconductivity. Superconductors with low T_c are called low temperature superconductors. The discovery of high temperature superconductors (HTS) occurred in 1986, when Bednorz and Müller found $T_c \cong 35$ K for $La_{2-x}Ba_xCuO_4$ [1]. Shortly afterwards, $YBa_2Cu_3O_{7-\delta}$ with $T_c \cong 90$ K, which is above the boiling temperature of liquid nitrogen (77K), was reported [27-29]. To the present date, the highest observed T_c is $\cong 138$ K in $Hg_{0.8}Tl_{0.2}Ba_2Ca_2Cu_3O_{8.33}$ at normal pressure [30]. The discovery of high temperature superconductive materials leads to numerous applications such as superconducting quantum interference devices (SQUID) [31], microwave devices [32], transmission lines [33], optical opening switches [34], and THz sources [35, 36].

Although the physics of the low temperature superconductor can be well explained by the BCS theory, the physical mechanisms behind high temperature superconductors are not well understood so far and are still under investigation. This is one of the main reasons we conduct research on the optical response of high temperature superconductors in this thesis.

2.1.3 $YBa_2Cu_3O_{7-\delta}$

In this thesis, the high temperature superconductor under study is yttrium barium copper oxide, $YBa_2Cu_3O_{7-\delta}$ (YBCO), which is the only known stable four-element high temperature superconductor discovered with a transition temperature ($T_c \cong 90$ K) above the boiling point of liquid nitrogen ($\cong 90$ K). YBCO was first discovered by Wu *et al*. in 1987 [27] and widely studied afterwards due to its many advantages over other high temperature superconductors such as stability, non-toxic composition, and ease of making of high quality single-phase samples.

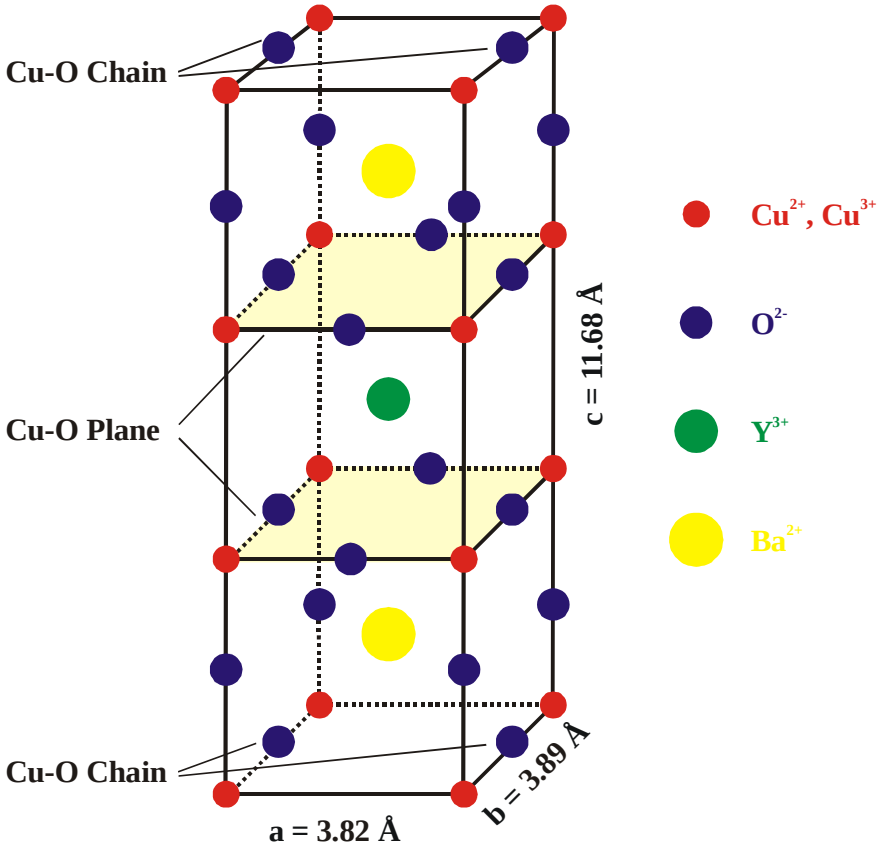

Figure 2-2 Crystal structure of $YBa_2Cu_3O_7$.

The orthorhombic crystal structure of YBCO is shown in Figure 2-2. The lattice constants in *a*, *b* and *c*-directions are *a* = 3.822 Å, *b* = 3.891 Å, and *c* = 11.677 Å, respectively. Its critical current density J_c and energy gap 2Δ are ≅ 10^6 A/cm^2 and ≅ 26 meV at 77 K. One of the most commonly used substrates of YBCO is $LaAlO_3$, which has a rhombohedral perovskite crystal structure with *a* = 3.793 Å. This selection is based on the fact that the lattice constant and the thermal expansion coefficient of YBCO and $LaAlO_3$ are almost identical. The dielectric constant of $LaAlO_3$ is ≅ 24.

2.2 Study of the Optical Response of YBCO Films and its Motivation

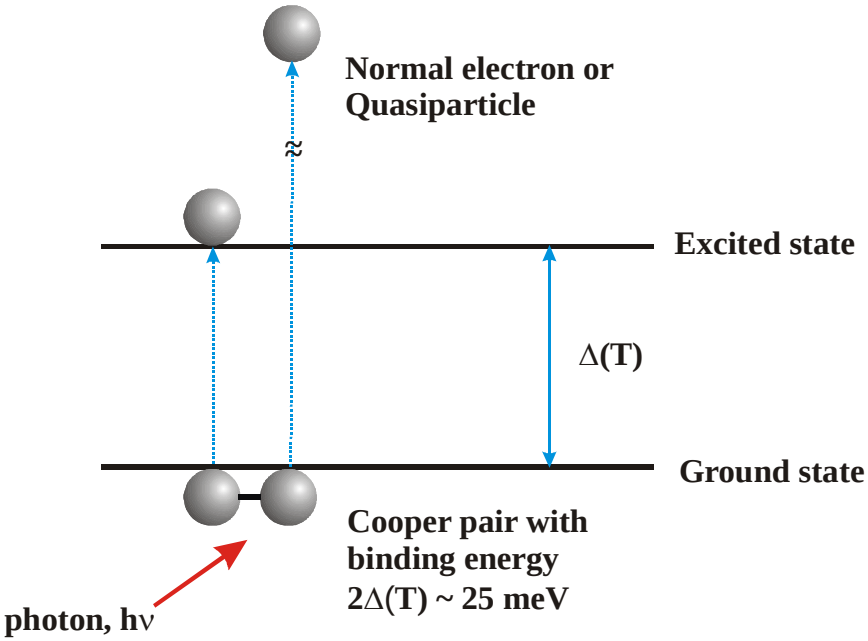

Figure 2-3 Schematic of Cooper pair breaking with laser illumination.

As mentioned earlier, two normal electrons with opposite spins form the so-called Cooper pair in the superconducting state. A Cooper pair is bound together with an energy of $2\Delta(T)$. By applying photons with energy hν ≥ 2Δ(T), the Cooper pair can be broken

and the electrons can be excited to the normal state, as shown in Figure 2-3. We call the excited electrons quasiparticles. The optical response of a biased superconducting device refers to a generated ultrafast voltage transient due to the breaking of Cooper pairs by laser illumination. The first experiment studying the laser activation of a superconductor was performed in 1971 [37]. After the discovery of HTS materials in 1986, the optical response of HTS thin films with pulsed laser illumination has been studied extensively. This is partially due to high temperature superconductors' potential applications as broadband photodetectors and opening switches, partially due to the fact that the optical response can provide a method of studying the non-equilibrium dynamics of quasiparticles, which are of great interest since it may lead to understandings of fundamental physical mechanisms of HTS.

Based on the two considerations above, we carried out research on the optical response of YBCO with femtosecond laser pulse illumination in this thesis. The experimental techniques involving the femtosecond laser system, superconductor device preparation and experimental setup are discussed in Chapter 3. Chapter 4 presents the comprehensive study of the optical response of YBCO. The theoretical background of the optical response is examined first. In addition, the optical responses – temperature dependence, laser power dependence and current dependence, of YBCO films with various film thickness are systematically studied. These studies help us to better understand the physical processes – both non-equilibrium (fast) and quasi-equilibrium (slow, thermal) processes embedded in optical responses. Thirdly, the laser energy dependence of the fast optical response is also discussed. A resonant effect at around 1.5 eV is observed for optimally doped YBCO. Fourthly, a time-resolved pump-probe

measurement of the fast optical response is performed. An 8 ps optical response is observed. Finally, an application of a superconductor opening switch and a superconductor transmission line to a current charged transmission line system (CCTL) is discussed. Chapter 5 gives the summary future work in this field.

Chapter 3 Experimental Techniques: Femtosecond Laser System, Superconductor Device Preparation, and Experimental Setup

3.1 Femtosecond Laser System

Ultrashort laser pulse generation is based on a mode-locking technique, which refers to simultaneously locking the phase of the multi longitudinal modes of a laser cavity. The temporal output of a mode-locked laser is no longer a continuous wave, but a well-defined periodic function of time, or in other words, a pulse train. The pulse duration is determined by the oscillating spectrum of the lasing medium; the wider the bandwidth of the laser gain – that is, covering more longitudinal modes, the shorter the pulse duration. The first active mode-locked laser was a He-Ne laser introduced in 1964 by Hargrove *et al.* with a nanosecond laser pulse achieved [38]. The first picosecond pulse was demonstrated in a passive mode-locked Nd:glass solid state laser using a saturable absorber by DeMarea *et al.* in 1966 [39]. Since then, dramatic advances have been witnessed in pulse generation. In 1974, Shank and Ippen reported the generation of the first optical pulse with less than a picosecond duration and kilowatt peak power using a cavity dumped and passively mode-locked rhodamine 6G dye laser [40]. By 1987, laser pulses with widths as short as 6 fs, which approaches the fundamental limits, had been generated in a ring laser system [41]. The development of faster laser pulses stopped temporarily since a frequency bandwidth larger than 1 PHz is required for attosecond

range laser pulses and such a bandwidth could not be supplied by the gain curve of any of the existing lasing material [42]. It was not until 2000 that two experiments confirmed the feasibility of attosecond pulse generation using the high-order harmonics of femtosecond laser pulses [43, 44].

Although the generation of attosecond laser pulses is still in the laboratory stage, the femtosecond laser system has become commercially available. This is largely due to the advent of Kerr lens self-modelocking in Ti:sapphire lasers in 1991 [45], resulting in simplification of use and stability of the laser output. With an optimized configuration, sub-two-cycle pulses (4-5 fs) can be obtained by a Ti:sapphire laser oscillator [46]. However, commercial system typically provides ≅ 100 fs laser pulses.

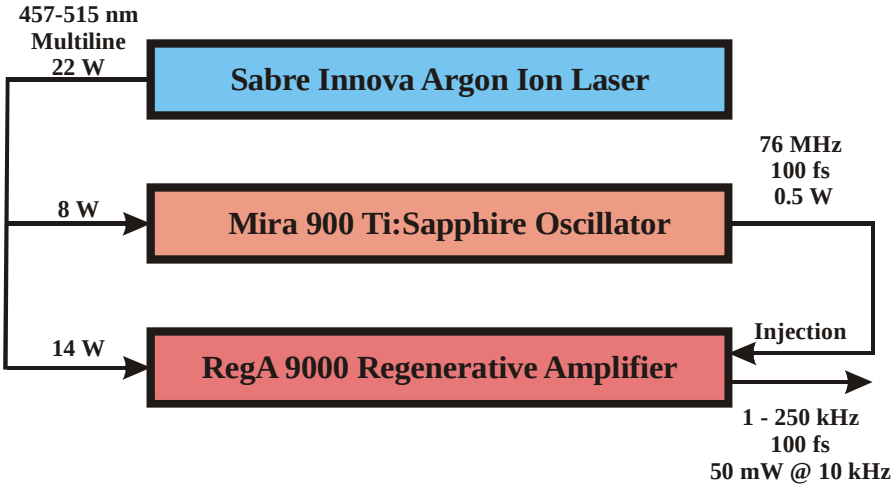

Figure 3-1 Schematic of the femtosecond laser system used in this thesis research.

As a research tool used throughout this thesis, the commercial Coherent femtosecond laser system consisting of a pump laser (Sabre Innova Argon Ion Laser), a Ti:Sapphire oscillator (Mira 900), and a Ti:Sapphire regenerative amplifier (RegA 9000), as shown in Figure 3-1, will be introduced next.

A. Sabre Innova Argon Ion Pump Laser

A *cw* Sabre Innova argon ion laser system is used as the pumping source which can output laser with a variety of wavelengths from 457 nm to 514 nm at 22W, of which 8W pumps the oscillator and 14W pumps the regenerative amplifier.

The pump laser consists of a laser head, a power supply, a remote control module, and a heat exchanger. A plasma tube, which is a sealed cylinder containing argon gas at a low pressure, is placed inside the laser head. With two additional high reflectivity end mirrors, one on each end, a laser cavity is formed. Argon gas, which is the gain medium, is discharged to be the ionized gas particles by applying a *dc* current to the tube. The current density is controlled by applying a magnetic field around the tube, hence forming a sheath to confine the plasma discharge. Higher dc current results in higher laser output. A power supply is used to provide the *dc* current for the argon tube. The Sabre ion laser works in a current regulation mode where a power supply maintains the plasma tube current at a constant value. The laser cavity is optimized automatically by step-motors that control the positions of the end mirrors. This in conjunction with a 'power track' function to maintain such optimized alignment achieves an optimized and stable output. All system functions can be controlled through a remote control module. A heat exchanger provides flowing of cool water through the laser to cool the laser head and the power supply.

B. Mira 900 Oscillator

The Mira 900 oscillator is a modelocked ultrafast laser that uses Ti:sapphire as the gain medium. The schematic layout is shown in Figure 3-2. Mirrors M1-M7 form the laser cavity that defines a 76 MHz repetition rate. An 8 W pump laser beam from the argon ion laser is focused onto the Ti:sapphire gain medium for efficient pumping.

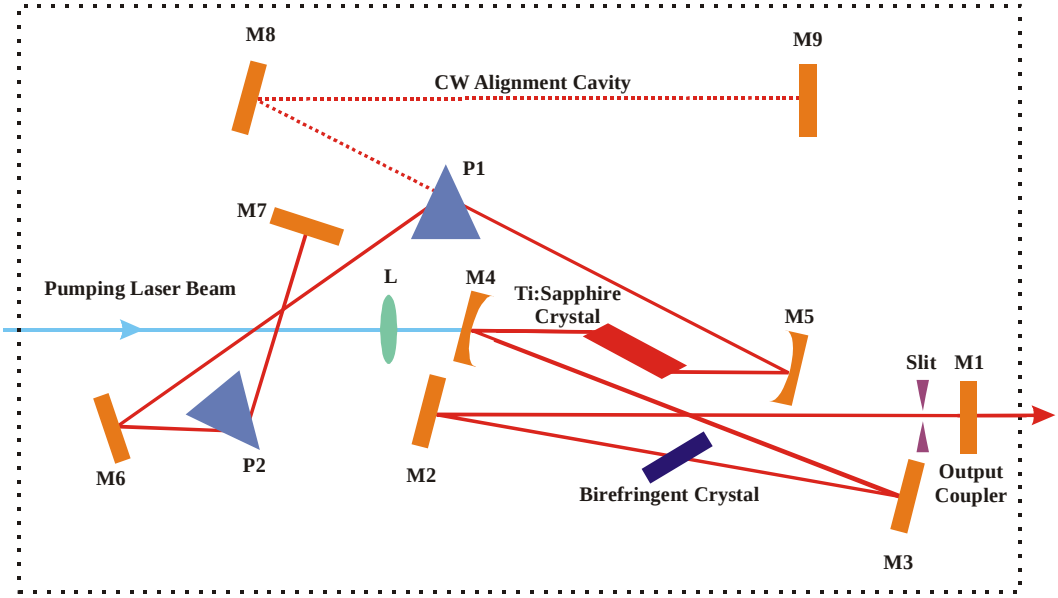

Figure 3-2 Schematic of the Mira 900.

The modelocking of the Mira system is achieved with the passive Kerr Lens Modelocking (KLM) that utilizes the nonlinear optical Kerr effect. The Kerr effect is a light-induced change of the index of refraction, as given by [47]

$$n = n_0 + n_2 I(t), \tag{3.1}$$

where n_0 is the normal index of refraction, n_2 is the intensity dependent non-linear $\chi_{(3)}$ related index of refraction on the order of 10^{-16} cm^2/W, and I is the intensity of the laser. The particular Kerr effect leading to the modelocking is self-focusing. Considering a transverse laser mode in a non-linear medium, the center portion of the mode with higher intensity experiences a larger index of refraction than at the edge. This leads to the formation of a gradient index lens, or Kerr lens, which makes the mode self-focus within the medium. According to (3.1), only when laser intensity is sufficiently high will the second term be non-negligible and hence the Kerr lens is formed. Self-focusing could not

be realized in a *cw* mode due to the weak intensity. As a result, a mechanism has been created that only narrows the modelocked beam. As shown in Figure 3-3, a slit is placed inside the cavity to attenuate the broad beam. Therefore, the modelocked pulses experience less round-trip loss than the *cw* beam. The higher the pulse intensity, the lower the cavity loss. This behavior is similar to that of a fast saturable absorber and results in a passive modelocking. The whole modelocking process is a positive feedback process in the sense that a single initial pulse bouncing back and forth within the laser cavity experiences gain in Ti:sapphire medium and no loss at the slit, allowing the phase of all the longitudinal modes to be locked together. In this way, a modelocked pulse is produced. KLM is the most attractive modelocking technique for practical oscillators since it does not require cavity length stabilization.

However, modelocking based on the Kerr lens effect is not self-starting. Initially, the laser operates in *cw* mode and power fluctuations are not sufficiently high to form a Kerr lens. Hence, a starter, which is a glass plate as shown in Figure 3-2, is introduced to initiate the modelocking process. The starting mechanism can be explained as follows. First we note a prerequisite for high intensity fluctuations is that the laser has to operate simultaneously with as many longitudinal modes as possible. In order to do so, the starter is tipped with an angle through which the beam must pass more or less so that the length of the cavity is changed. In this way, a set of modes satisfying the “integral half waves between reflectors” criterion is selected, leading to a period during which many longitudinal modes coexist simultaneously. Thus a high power fluctuation can be produced to initiate the Kerr lens and consequently the modelocking process. Once the

modelocking starts, it will continue without the starting mechanism. This moving mirror self-starting scheme was first introduced by Rizvi *et al.* [48].

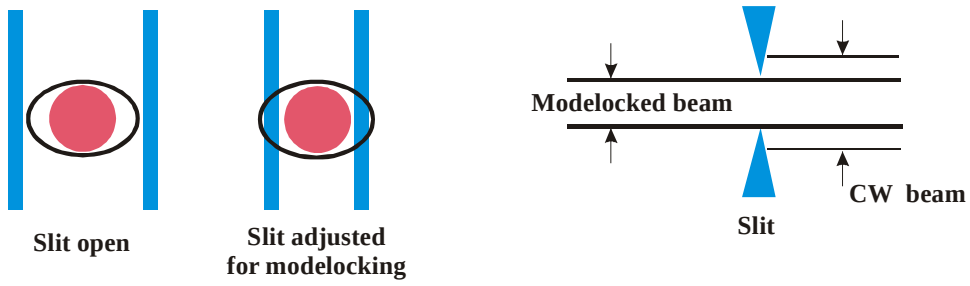

Figure 3-3 Mira 900 saturable absorber system.

An ultrafast pulse always experiences group velocity dispersion (GVD), which is defined as $d^2n/d\lambda^2$, because the index of refraction n depends nonlinearly on wavelength λ for almost all materials. GVD produces the nonlinear phase shift for each wavelength components, resulting in a pulse-shape distortion. Positive GVD, which leads to a positive chirp where red frequency components of the pulse lead blue ones, has to be compensated by negative GVD in order to output stable femtosecond laser. The optical material (Ti:sapphire crystal , dielectric coatings of each mirror, etc.) and the self phase modulation (SPM) in Ti:sapphire crystal are the two main sources of positive GVD in Mira system. The SPM is one of Kerr effects that utilizes the temporal intensity distribution of the laser pulse in time domain. The leading and tailing edges of the pulse experience a smaller index of refraction than the center part where intensity is high, resulting in an altered pulse-shape. A pair of prisms (P1, P2), which are separated by a distance and oriented in a specific direction, are used as negative GVD component [49].

By properly adjusting the prisms the positive GVD cancels the negative one, and hence giving rise to an equilibrium pulse with stable width and amplitude.

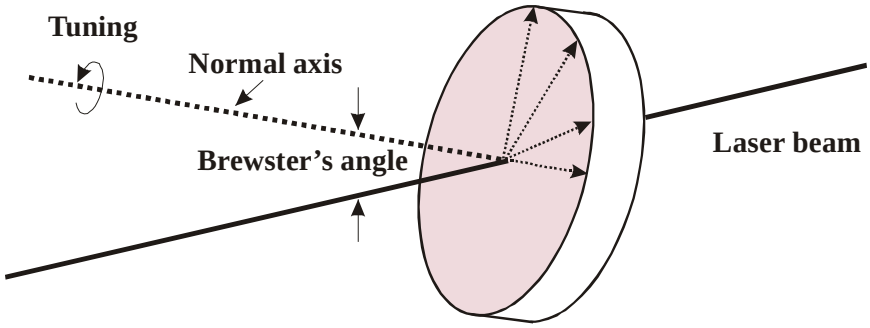

Figure 3-4 Operation of wavelength tuning with a birefringent tuning filter.

For the superconductor project, the wavelength of the femtosecond laser pulse is required to be tunable. We introduce briefly the principle of the wavelength tuning in the following. The wavelength of the output femtosecond laser pulse can be tuned with a birefringent filter (BRF), which is a full-wave plate, as shown in Figure 3-4. A BRF is mounted in the laser cavity at Brewster's angle in order to eliminate reflection of the vertically polarized component while allowing loss on the horizontally polarized component. For linear polarized light at the designed wavelength, the polarization experiences no change when passing through such a full-wave plate; however, for light of other wavelengths the output laser becomes elliptically polarized (because the retardation of the slow wave is not equal to one wavelength anymore) and hence experiences loss in the cavity. Therefore, the laser system can only work at the designed wavelength. The thickness of the BRF is designed to be one full wavelength at Brewster's angle. Rotating the wave plate with respect to its normal axis results in a change in refractive index along Brewster's angle, thereby selecting a new wavelength satisfying the full-wave criteria.

The center wavelength of the laser pulse is tunable from 750 to 850 nm in our experiments.

In conclusion, the Mira 900 modelocked laser system can generate ≅ 120 fs pulses with 76 MHz repetition rate and ≅ 500 mW average power.

C. RegA 9000 Regenerative Amplifier

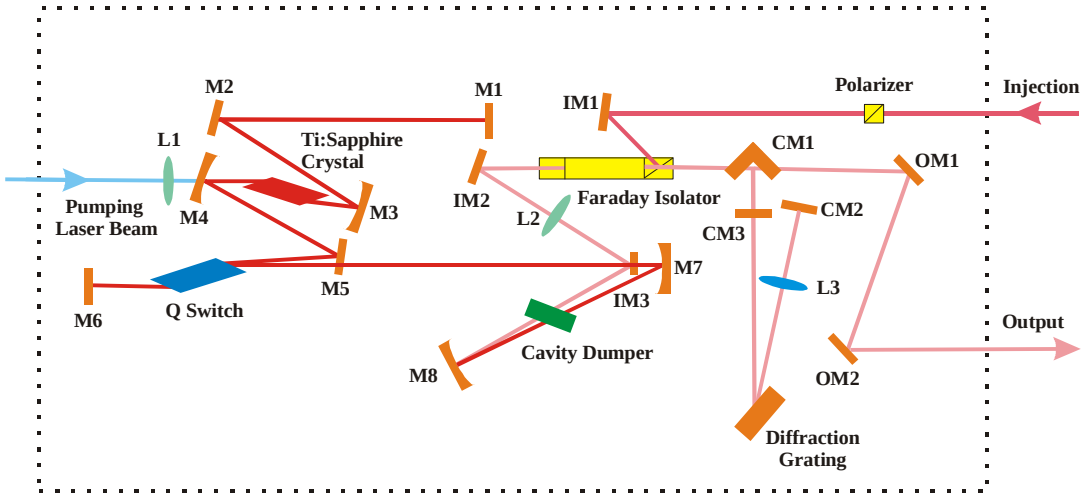

Figure 3-5 Schematic of the RegA 9000.

A regenerative amplifier is one good way to amplify a short pulse in a solid state laser system with a long upper level life time (≅ 2.5 μs for Ti:sapphire). RegA 9000 Ti:sapphire amplifier system, which is a chirped pulse amplification laser system originally designed by Norris [50], can operate over a wide repetition rate from 10 to 300 kHz with a high pulsed energy of ≅ 5 μJ. The schematic layout is shown in Figure 3-5.

The RegA cavity consists of a Q-switch, a Ti:sapphire gain medium, a cavity dumper (CD), a Faraday isolator (FI), and a diffraction grating working as a pulse compressor. The working principle of the RegA can be explained as follows. First, by

turning on the Q-switch loss is introduced in the laser cavity, thereby holding off the lasing. At the same time, gain will be built up to a high value through the continuously pumping of the Ti:sapphire gain medium with the 14 W *cw* output from an argon ion pump laser. Subsequently the Q-switch is turned off and a 120 fs pulse from the Mira oscillator, referred to as a seed pulse, is injected into the RegA cavity through the cavity dumper. The seed pulse is amplified and stretched to 40 ps after traveling back and forth inside the cavity over ≅ 25 roundtrips. Finally the cavity dumper extracts this amplified pulse into a pulse compressor, where the pulse-width is reduced to < 200 fs FWHM.

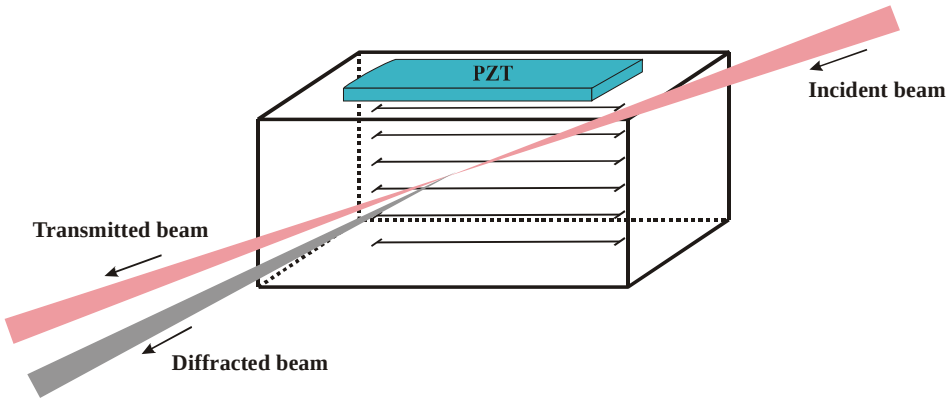

Figure 3-6 Simplified functional diagram of an AO modulator Bragg cell.

In the RegA 9000, the Q-switch is an acousto-optic (AO) modulator made of a 30 mm thick Brewster-angled TeO_2 optically polished slab with an acoustic transducer bonded on one side, as shown in Figure 3-6. An acoustic wave propagating in a medium perturbs the index of refraction because of the photoelastic effect, and hence creates an optical index grating. The grating diffracts the beam out of the resonator beam path and thus lasing is prevented. As a Q-switch, the AO modulator works in a standing wave regime in order to produce a stable diffraction grating pattern. Bragg diffraction, where light diffracts only in one direction if it incidents at the Bragg angle, is realized with an

80 MHz modulation frequency. Based on the highly dispersive property of TeO_2, the Q-switch also serves as a pulse stretcher to stretch the Mira pulse during each roundtrip of amplification. The stretcher is of great importance which ensures that a high peak-power pulse will not be formed inside the laser cavity, and therefore possible damage to the optical components is prevented.

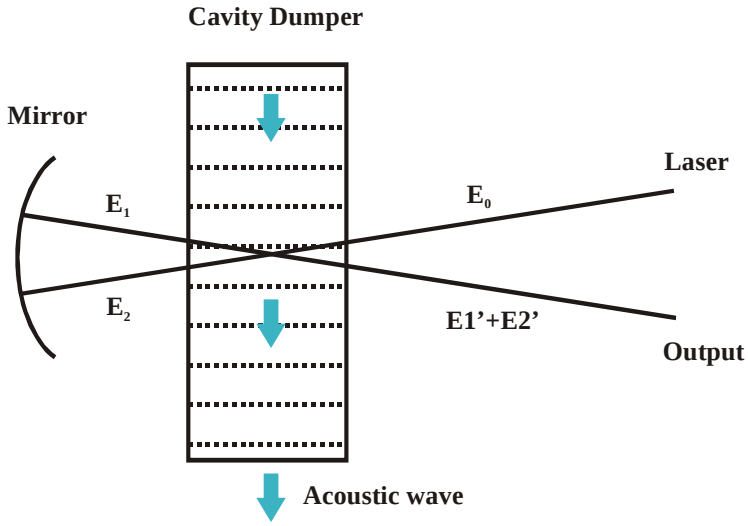

Figure 3-7 Schematic of double-pass cavity dumping.

The cavity dumper is a high-speed AO modulator used to: (1) inject one pulse from the 76 MHz Mira pulse train into the RegA cavity; and (2) eject the amplified pulse out of the RegA cavity. It is made of a fused silica crystal with a transducer. Like the Q-switch, the cavity dumper also works in the Bragg diffraction regime, although a traveling wave is launched into the modulator. Traveling wave operation leads to the formation of a traveling grating that results in a frequency shift of the diffracted light. The diffraction efficiency of the cavity dumper, η, is extremely important since the diffracted beam constitutes the output of the RegA laser. For this purpose, a unique double pass cavity dumping scheme, as shown in Figure 3-7, is introduced. With such a

regime, an injection and ejection efficiency of 100% can be achieved by properly adjusting the phase of the acoustic wave and the special orientation of the cavity dumper.

A Faraday isolator (FI), which is composed of a Faraday rotator, a crystal quartz rotator and a Brewster faced polarizer, is used to direct the input Mira pulse into the RegA cavity while preventing the output RegA pulse from feeding back to the Mira cavity. Both the Faraday rotator and the quartz rotator produce a 45° polarization rotation. However, the rotations are not symmetric; in one direction they add up while in the reverse direction they cancel each other out. The vertically polarized input pulse from the Mira is directed toward the Brewster faced polarizer, and reflected totally to Faraday and quartz rotators, where it experiences a 90° polarization rotation. The resulting horizontal polarized pulse is then injected into the RegA cavity. Reversely, the horizontal polarized RegA output pulse experiences no polarization change when passing through the Farady and the quartz rotator, and thus propagates to the pulse compressor without any attenuation. Therefore, the pulse feeding back to Mira is prevented.

As stated before, the pulse-width of the ejected pulse from the RegA cavity is stretched to ≅ 40 ps; hence, a pulse compressor is required to narrow the output pulse-width back to < 200 fs. A gold-coated holographic diffraction grating in a 4-pass configuration is applied in the RegA 9000 for this purpose. The 4-pass configuration consists of mirrors CM1 – CM3 and lens L3, as shown in Figure 3-5.

Finally, a pulse with the desired high peak power ($\times 10^7$ W) and adjustable repetition rate (10-300 kHz) is obtained.

3.2 Thin Film Deposition

The development of thin film technology gives rise to numerous applications due to the fact that thin films have a wide range of advantages over bulk materials. Most of the measurements conducted on bulk materials can also be performed on thin films, usually with more pronounced results. For this reason, the YBCO devices used for the optical response study are made of thin films.

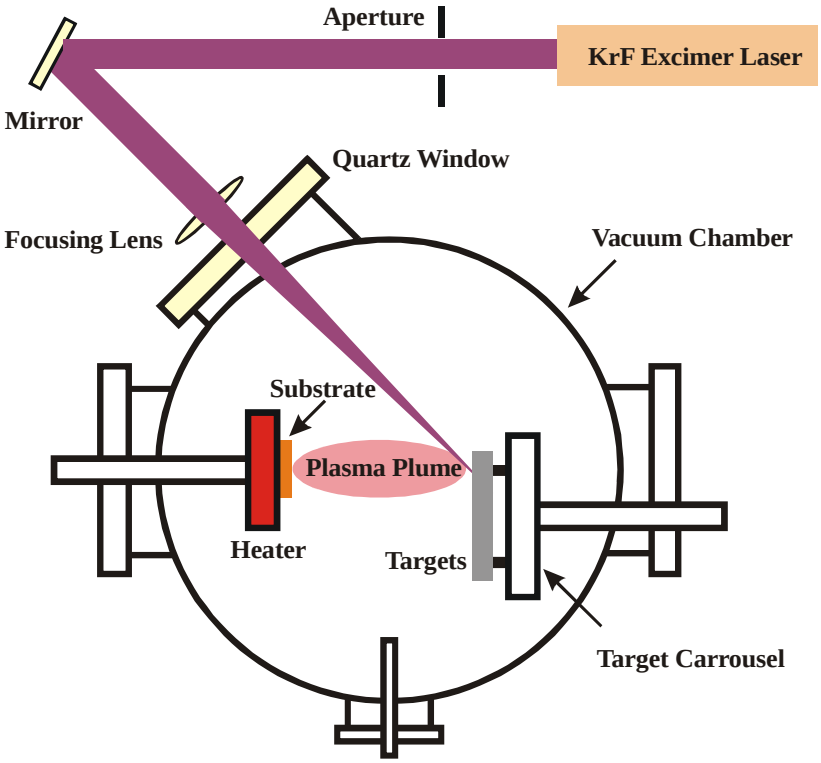

Figure 3-8 Schematic of a pulsed laser deposition (PLD) system.

The requirements of a good quality YBCO thin film include: high transition temperature, narrow transition width, high critical current density, high film uniformity, and low surface resistance at high frequencies. Several techniques such as electron beam evaporation [51, 52], molecular beam epitaxy (MBE) [53, 54], sputtering [55-58], chemical vapor deposition (CVD) [59-62], and pulsed laser deposition (PLD) [63-65]

have been used to grow high temperature superconductive thin films. In our case, YBCO thin films are prepared with the PLD technique.

PLD is an important research tool for growing high quality multi-component oxide ceramic thin films, such as high temperature superconductor films, ferroelectric films, ferromagnetic multi-layers, and colossal magneto-resistive (CMR) films. PLD was invented in the 1960s [66] and has been applied extensively since 1987 when the first YBCO thin film was successfully grown [63]. Figure 3-8 shows the schematic of a PLD system. It consists of a KrF excimer laser, a focusing system and a vacuum chamber inside of which a target and a temperature controlled substrate holder are located. The KrF laser generates UV laser pulses with a 25 ns pulse width, 248 nm wavelength, up to 1 J pulse energy, and 1-30 Hz repetition rate. The optical focusing system, with a focusing lens of ≅ 35 cm focusing-length being the main part, focuses the laser beam into a 1.5 mm × 5.5 mm spot onto the target at an incident angle of ≅ 45°. The typical pulse energy density on the target is ≅ 1 J/cm^2. The target, which is a bulk material of interest (for example, a YBCO target is used to obtain a YBCO thin film), is placed in a target holder which rotates continuously during deposition in order to prevent the formation of deep craters. The substrate holder, which is essentially a hot plate, is positioned ≅ 10 cm away from the target surface. The substrate is mounted onto the heater with silver paste, and is placed perpendicular to the normal of the target and directly facing the target to obtain the maximum film uniformity. The substrate temperature is an important parameter for thin film growth and is controlled by a PID controller. The typical temperature of the substrate for YBCO deposition is ≅ 780°C. When the high-energy laser pulse hits the target, the electrons and the lattice of the target material will absorb

the laser energy, and the target will be heated. When the heating energy is above a certain threshold, the target material is ejected, forming a plasma plume consisting of the target elements. The heated substrate is placed within the plasma plume so that the target elements are deposited onto it. A thin film of the target material is then formed. Deposition is done with an oxygen pressure of ≅ 100 Torr and a deposition rate of ≅ 2 Å/sec. After the deposition, the sample is cooled down to room temperature in a 200 Torr oxygen atmosphere.

There are several advantages of the PLD. First of all, it is a high-energy process. It has the capability to produce films whose elemental compositions are exactly the same as the targets regardless of how complex the composition of the target material is. This unique advantage makes PLD an important approach in growing HTS thin films which possess complex unit cells. In addition, during this high-energy process, species in the plasma plume have such a high kinetic energy that they can diffuse into thermodynamically stable sites, leading to a better crystallization of the deposited thin film. Finally, with such pulse-based technique the film is grown in a growth-relaxation-growth manner, which also results in a good crystallization in deposition. Furthermore, this manner allows for the study of surface kinetics of crystal growth far from equilibrium.

In general, PLD is a good choice for producing HTS thin films. The deposition quality strongly depends on the selection of substrate, laser pulse properties (such as energy density and repetition rate), oxygen pressure, and deposition temperature. In order to grow films of high quality, the lattice constant and the thermal expansion coefficient between the substrate and target materials have to be matched. In our study, an $LaAlO_3$

single crystal, with lattice constant a = 3.793 Å, is selected as the substrate material of YBCO, with lattice constant a = 3.82 Å. Moreover, the energy density of the laser pulse has to be controlled in such a way that it not only provides the target elements enough kinetic energy, but also minimizes the possibility of creating micron-sized particulates which are sputtered out from the target due to the high laser energy density. A certain level of the oxygen pressure is necessary during the deposition to ensure the correct chemical composition of oxygen – since the oxygen is easily lost during the deposition process. The deposition temperature, or temperature of the substrate, is very critical for growing high quality films from a crystallization point of view since a suitable temperature will help locating the deposited elements in their correct positions.

3.3 Device Design

The YBCO device used for the optical response study is a 50 Ω YBCO coplanar waveguide (CPW) made of YBCO thin film. Any spot on the center strip of the CPW can be used as the laser illumination spot. The selected spot is called an opening switch since without laser illumination the superconductor is in superconducting state with zero impedance (switch is closed; circuit is closed); however, with laser illumination the impedance is non-zero (switch is opened). The purpose of the transmission line structure is to transmit the fast optical response transient with both insignificant dispersion and attenuation. In this section, we introduce the design issues of the CPW.

The CPW, which is a coplanar transmission line, was first introduced by Wen in 1969 [67]. The term *coplanar* indicates that all the conductors, namely the signal line and the ground line, are in the same plane. The CPW structure is advantageous in that: (1) the

mounting of lumped components in shunt or series configuration is considerably easier, and (2) the integration with active elements such as MESFETs, which are coplanar in nature, becomes less difficult. The main parameter of a CPW is its characteristic impedance, *Z*. The design of a CPW is essentially to arrange the geometry of the device so that a specific *Z* is obtained. In this thesis, the device is designed to have a 50 Ω characteristic impedance to match the connection cables so as to avoid the signal reflection at each device-cable interconnection. Figure 3-9 shows the device structure of a CPW.

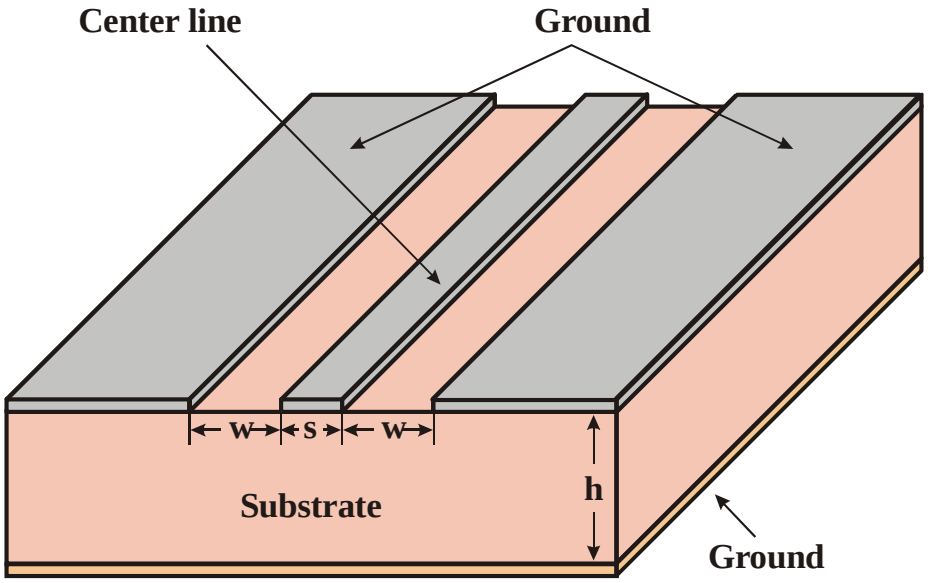

Figure 3-9 Device structure of the coplanar waveguide (CPW).

The characteristic impedance, *Z*, of such a waveguide is given by [68]

$$Z = \frac{60\pi}{\sqrt{\varepsilon_{eff}(f)}} \frac{1}{K(k_1)/K(\sqrt{1-k_1^{\,2}}) + K(k_3)/K(\sqrt{1-k_3^{\,2}})}, \qquad (3.2)$$

where $K(k)$ is the complete elliptic integral of the first kind and $\varepsilon_{eff}(f)$ is the effective dielectric constant. $K(k)$ is defined by

$$K(k) = \int_0^{\pi/2} \frac{d\varphi}{\sqrt{1-k^2\sin^2\varphi}}. \tag{3.3}$$

The constants k_1, k_2, and k_3 are given by

$$k_1 = \frac{s}{s+2w}, \tag{3.4}$$

$$k_2 = \frac{\sinh(\pi s/4h)}{\sinh(\pi(s+2w)/4h)}, \tag{3.5}$$

$$k_3 = \frac{\tanh(\pi s/4h)}{\tanh(\pi(s+2w)/4h)}, \tag{3.6}$$

where s, w, and h are the strip width, slot width, and substrate thickness respectively, as shown in Figure 3-9. The expression of the frequency dependant effective dielectric constant, $\varepsilon_{eff}(f)$, is obtained by fitting the results of numerical simulation, and is given by

$$\sqrt{\varepsilon_{eff}(f)} = \sqrt{\varepsilon_{eff}(0)} + \frac{\sqrt{\varepsilon_r} - \sqrt{\varepsilon_{re}(0)}}{1+G(f/f_{TE})^{-1.8}}, \tag{3.7}$$

where ε_r is the dielectric constant of the substrate, f_{TE} is the cutoff frequency for the TE_0 surface wave mode and is given by

$$f_{TE} = \frac{c}{4h\sqrt{\varepsilon_r - 1}}. \tag{3.8}$$

G is a geometry-defined parameter that is given by

$$\begin{aligned} \ln G &= u \ln(s/w) + v \\ u &= 0.54 - 0.64p + 0.015p^2 \\ v &= 0.43 - 0.86p + 0.54p^2 \\ p &= \ln(s/h) \end{aligned} . \tag{3.9}$$

$\varepsilon_{eff}(0)$ is the effective dielectric constant at zero frequency and takes the form

$$\varepsilon_{eff}(0) = 1 + q(\varepsilon_r - 1), \tag{3.10}$$

where q is a geometry dependent parameter expressed as

$$q = \frac{K(k_3)/K(\sqrt{1-k_3^2})}{K(k_1)/K(\sqrt{1-k_1^2}) + K(k_3)/K(\sqrt{1-k_3^2})} . \tag{3.11}$$

In the thesis work, the CPW structure with strip width s = 30 μm and slot width w = 60 μm is designed to obtain a 50 Ω characteristic impedance. The CPW device is fabricated by patterning a YBCO thin film that is deposited on a 0.5 mm thick $LaAlO_3$ crystal substrate. Gold electrical contact pads with a 3000 Å thickness are deposited to connect the device to outside connectors, K-type or SMA type. The cutoff frequency of a K-type or an SMA connector is 40 or 15 GHz respectively. The sample is clamped tightly on a temperature controlled copper holder, which serves as the ground plane. Figure 3-10 shows a schematic of a CPW device and a real image of a CPW device under an optical microscope.

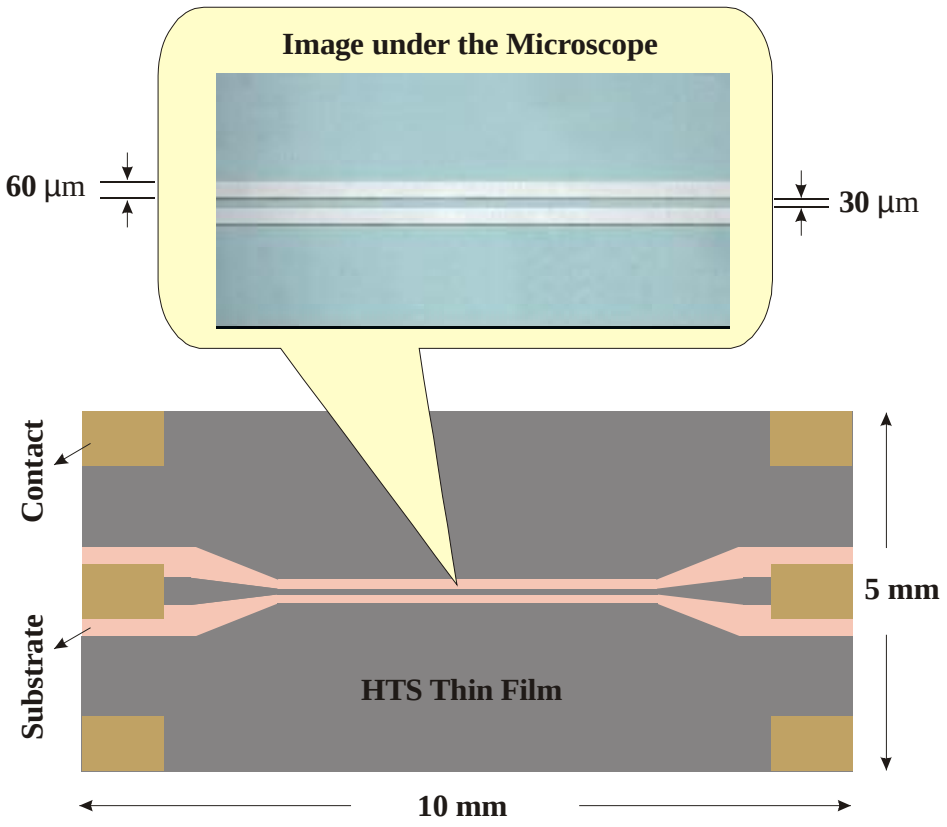

Figure 3-10 Schematic of a CPW device (below) and a real image of a CPW device under an optical microscope (above).

3.4 Device Fabrication

The YBCO films prepared by PLD are patterned into the CPW structure through standard photolithography and wet etching. The procedure is as follows:

1. Clean the thin film sample with trichloroethylene, acetone, and methanol in ultrasound for 5 minutes each. Blow dry the sample with nitrogen gas.

2. Put the sample on a spinner, coat it with photoresist PR-s1813 and spin it at about 4500 rpm for 40 sec. The resulting thickness of photoresist is ≅ 1 μm.

3. Bake the sample in an oven at 90 °C for 3 minutes. The purpose of baking is to improve the adhesion between the photoresist and the sample.

4. Align the mask and expose the sample with UV light with a power density on the order of mW/cm^2 for 11 seconds.

5. Develop the sample for 10 seconds in a Microposit CD-30 solution.

6. Wet-etch the sample with a diluted nitric acid solution of ≅ 0.25%. The typical etching rate for YBCO thin film is ≅ 100 Å/sec.

7. Remove photoresist by soaking the sample in acetone.

8. Deposit ≅ 3000 Å of gold to form electrode contact pads with a contact mask.

The quality of the fabricated device is strongly process-dependent. The above stated parameter values, such as baking time, exposure time, and development time, are only given as a reference. Adjustments have to be made each time of fabrication in order to obtain a satisfactory device.

3.5 Experimental Setup

Figure 3-11 shows the experimental setup of our Transient Photoimpedance Response (TPR) method [2-6] which is employed in this thesis to investigate the optical responses of YBCO thin films. The device was mounted on a cold finger located in a vacuum cryogenic chamber (RC100, CryoIndustries). The vacuum could reach as low as ≅ 10^{-6} Torr with a molecular pump system (Drytel 31, Alcatel). The chamber was refrigerated with liquid helium or liquid nitrogen through a vacuum transfer line. A PID controller (330, Lake Shore) with 0.1 K stability within the range of 10-300 K was used to control the temperature of the YBCO devices. The Ti:sapphire femtosecond regenerative amplifier system described in section 3.1 was utilized to provide laser pulses with ≅ 100 fs pulse width, ≅ 10 kHz repetition rate, energy of up to several μJ per pulse,

and tunable wavelength from 750 nm to 850 nm. With a 10 kHz repetition rate, the time separation between two consequent pulses is 0.1 ms. This time is much larger than the time constant for phonons to escape from the film to the substrate; therefore, the film can be cooled down prior to the arrival of the next laser pulse and heat will not accumulate. On the contrary, higher repetition rate results in significant heat buildup and therefore the difficulty in observing the fast optical response. The laser was split into two beams with a 90/10 beam-splitter. The main beam was focused onto the center strip of the YBCO device through a cylindrical lens with $f \cong 10$ cm. The focusing spot is $\cong 2$ mm × 200 μm, leading to an energy fluence of $\cong$ 25 μJ/cm^2 with a 1 mW average laser power (corresponding to a 10^6 W peak power). A cylindrical lens was selected because it may induce a smaller temperature increase than a spherical lens of the same focal length. The other 10% of the laser beam was guided to a photoconductive switch that provides the trigger signal for the oscilloscope. The YBCO device was dc biased with a programmable current source (224, Keithley). A sampling oscilloscope (54750A, HP) with a 50 Ω input impedance and 20 GHz bandwidth was used to monitor the optical response. The average laser power is continuously adjustable using a neutral density filter, and was measured with a power meter (835, Newport). The spectrum of the laser pulse was measured with an optical spectrometer (PC2000, Ocean Optics).

The equivalent circuit of the experimental setup is shown in Figure 3-12. When the temperature of the superconductor device is below T_c, the resistance of device is zero. With pulsed laser illumination, regardless of its physical origins, a voltage transient is generated by the superconductor switch. Since the superconducting device is connected

in series with the 50 Ω oscilloscope, what we expect to observe on the oscilloscope is the flipped, negative voltage signal with equal amplitude.

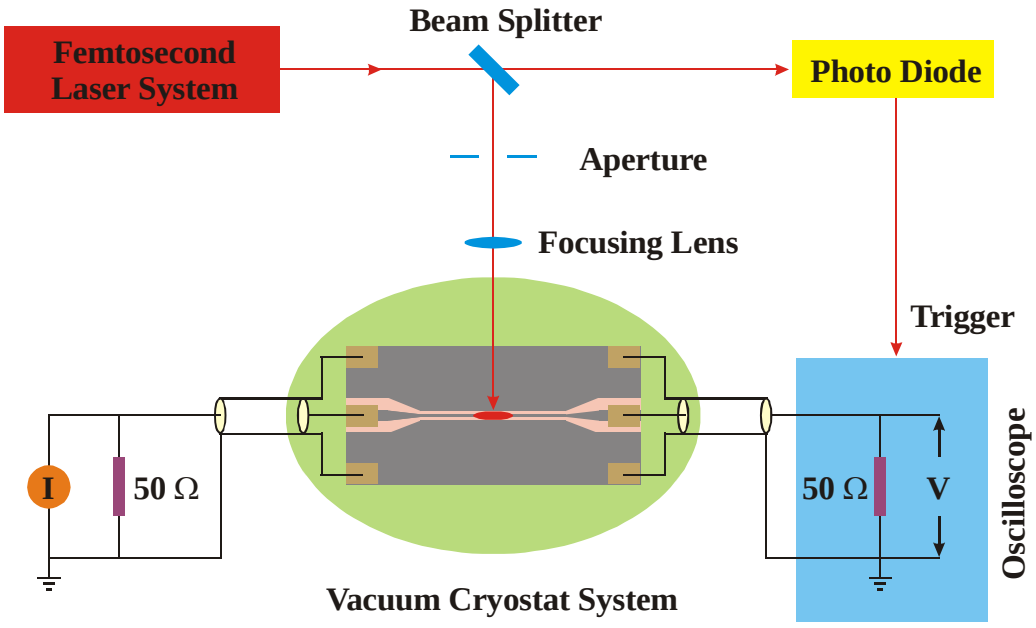

Figure 3-11 Experimental setup of the Transient Photoimpedance Response (TPR) method.

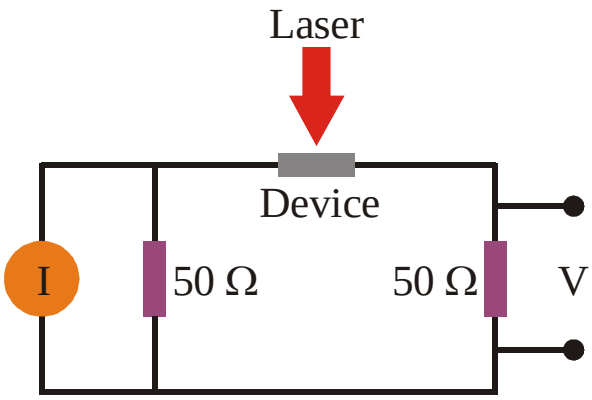

Figure 3-12 Equivalent circuit of the TPR method.

The advantages of our TPR method include: (1) it can directly measure the electrical optical responses due to Cooper pair breaking, which is an issue leading to tremendous research efforts, and (2) it is a simple method with high signal to noise ratio.

Due to the application of high-energy laser pulses from the femtosecond regenerative amplifier system, the signal to noise ratio of our TPR method is improved to a few parts in 10^2. Therefore, this method is suitable to be applied to study the effect of the parameters, such as laser power, substrate temperature, biased current, film thickness, and wavelength, on the optical responses.

As will be revealed in Chapter 4, the theoretical non-equilibrium optical response is a very fast electrical transient – on the order of picoseconds. However, the temporal resolution of the oscilloscope is only ≅ 50 ps. Therefore the signal observed on the oscilloscope, $V(t)$, is a stretched or dispersed version with respect to the intrinsic signal, $V_{intrinsic}(t)$. $V(t)$ can be related to $V_{intrinsic}(t)$ through the impulse response function, $h(t)$, of the electronic measurement system – in our case mainly the oscilloscope [69],

$$V(t) = \int_0^t \dot{V}_{intrinsic}(\tau) h(t-\tau) d\tau , \tag{3.12}$$

where $\dot{V}$ represents the derivative of V. $h(t)$ can be modeled as [70]

$$h(t) = (1 - e^{-\frac{f_H t}{0.35}}) \cdot e^{-\frac{f_L t}{0.35}} . \tag{3.13}$$

f_H and f_L can be obtained by

$$\begin{aligned} \frac{0.35}{f_H} &= \sqrt{\sum_i (\frac{0.35}{F_i})^2} \\ \frac{f_L}{0.35} &= \sqrt{\sum_i (\frac{f_i}{0.35})^2} \end{aligned} , \tag{3.14}$$

where F_i and f_i are the upper and lower band pass frequencies of the electronic components constituting the monitor system. If we only consider the maximum amplitude of the signal, and if the variance of $V_{intrinsic}(t)$ is sufficiently small, then [71]

$$Max[V(t)] = \alpha \cdot Max[V_{intrinsic}(t)], \qquad (3.15)$$

which suggests that the maximum amplitude of the signal observed on the oscilloscope is proportional to that of the intrinsic signal.

In conclusion, this TPR experimental setup allows us to comprehensively study the optical response of YBCO thin films.

Chapter 4 Study of the Optical Response of YBCO Thin Films

4.1 Theoretical Background of Optical Response

The Cooper pairs in a superconductor can be broken with pulsed laser illumination. Consequently, quasiparticles are generated and a voltage transient is produced given that such a superconductor is properly biased. This voltage transient is referred to as the optical response. Optical responses are typically classified into non-equilibrium fast optical responses and bolometric slow optical responses. In the non-equilibrium process, only the electron subsystem is disturbed by the laser pulse radiation, while the phonon subsystem remains in thermodynamic equilibrium with the substrate. However in the bolometric process, laser illumination results in the heating of the superconducting film in which the electron and phonon subsystems can be described by the same temperature shift with respect to the substrate. This thermal process is determined by both the thermal boundary resistance of the film-substrate interface and the heat diffusion within the substrate. In both the non-equilibrium and bolometric processes, the absorption of laser energy causes a re-distribution of quasiparticles and gives rise to a variation of macroscopic parameters such as kinetic inductance and resistance.

This section deals with the theoretical background of optical responses. Physical processes associated with the laser illumination of a superconductor are discussed. Physical models explaining the optical responses are presented.

4.1.1 Qualitative Description of the Physical Mechanisms Inherent in the Optical Response

In this section, we discuss the physical processes leading to the optical response. Essentially, we answer the question "what happens when a laser illuminates a superconducting thin film?". We start with a review of several important time constants: electron-electron (*e*-*e*) interaction time $\tau_{e\text{-}e}$, electron-phonon (*e*-*p*) interaction time $\tau_{e\text{-}p}$, phonon-electron (*p*-*e*) interaction time $\tau_{p\text{-}e}$, phonon diffusion time in film τ_{diff}, phonon diffusion time across a thermal boundary τ_{esc}, and phonon diffusion time in a substrate $\tau_{diff\text{-}sub}$.

$\tau_{e\text{-}e}$ characterizes the *e*-*e* interaction process, which leads to a fast avalanche multiplication of non-equilibrium quasiparticles. For YBCO, it was estimated as [72]

$$\tau_{e-e} \approx \frac{2\times 10^{-17}}{E^2(eV)} \quad (\text{sec}). \tag{4.1}$$

We note that $\tau_{e\text{-}e}$ is inversely proportional to E^2. For an electron with energy E = 1.5 eV, $\tau_{e\text{-}e} \cong 0.01$ fs.

The *e*-*p* interaction time, $\tau_{e\text{-}p}$, is used to model the process of electrons transferring energy to phonons. For YBCO, it was estimated as [72]

$$\tau_{e-p} \approx \frac{3.3\times10^{-19}}{(\hbar\omega)^3(eV)} \quad \text{(sec)}, \tag{4.2}$$

where $\hbar\omega$ represents the phonon energy. For high-energy phonons of ≅ 50 meV, $\tau_{e\text{-}p}$ could be as small as 2.6 fs [73]. While for low-energy phonons, $\tau_{e\text{-}p}$ is on the order of 10 ps. Therefore $\tau_{e\text{-}p}$ is around a few picoseconds on the average.

Converse to $\tau_{e\text{-}p}$ is the *p-e* interaction time, $\tau_{p\text{-}e}$. $\tau_{p\text{-}e}$ is related to $\tau_{e\text{-}p}$ through the so-called energy balance equation

$$\frac{C_e}{\tau_{e-p}} = \frac{C_{ph}}{\tau_{p-e}}, \tag{4.3}$$

where C_e and C_{ph} are the heat capacities of electrons and phonons respectively.

τ_{diff} characterizes the phonon diffusion process within the superconductor film. It is given by [5]

$$\tau_{diff} = \frac{d^2 C}{\kappa}, \tag{4.4}$$

where *d* is the diffusion length (here the thickness of the superconductor film), and *C* and κ are the specific heat capacity and thermal conductivity of the superconductor film, respectively. For diffusion along the *c*-axis of YBCO thin films, $C \cong 1$ J/cm^{3}K and $\kappa \cong$ 0.026 W/cm-K [5] for temperature of 80 K, resulting in $\tau_{diff} \cong 3.9$ ns for a 100 nm film or 15.6 ns for a 200 nm film.

Phonons diffuse through the superconducting film and finally reach the film/substrate boundary. The characteristic time for phonons to cross this boundary is [74]

$$\tau_{esc} = CR_{BD}d\,, \tag{4.5}$$

where R_{BD} is called thermal boundary resistance defined as the ratio of the temperature difference ΔT across the interface to the heat intensity. For YBCO thin films, $R_{BD} \cong 10^{-3}$ Kcm^2/W [74]. Therefore τ_{esc} is $\cong$ 10 ns for a 100 nm film or 20 ns for a 200 nm film.

The last time constant we consider is the phonon diffusion time in the substrate, which is given by

$$\tau_{diff-sub} = \frac{d_{sub}{}^2 C_{sub}}{\kappa_{sub}}\,, \tag{4.6}$$

where C_{sub}, κ_{sub}, d_{sub} are the heat capacity, thermal conductivity, and thickness of the substrate respectively. With C_{sub} = 0.4 J/cm^{3}K, κ_{sub} = 0.35 W/cmK and d_{sub} = 0.5 mm for $LaAlO_3$ substrate [75], $\tau_{diff-sub} \cong$ 3 ms. We note that for most cases this time constant is neglected since after all it is the heat within the superconductor film that is responsible for the optical response.

Based on the above time constants, the physical mechanisms governing the optical response can be described as follows.

First, Cooper pairs are broken into quasiparticles by incoming photons. Each photon with energy E ($E \cong$ 1.5 eV) will break one Cooper pair and create two quasiparticles with respective energies E-2Δ and 2Δ, where 2Δ is the Cooper pair bounding energy which is around 25 meV for YBCO [76]. Being in a non-stable high-energy state, the quasiparticle with a higher energy of E-2Δ tends to relax to a low-energy state. Naturally, a question arises – "Through which interaction will it relax?". As illustrated earlier, for high-energy electrons $\tau_{e\text{-}e}$ ($\tau_{e\text{-}e} \cong$ 0.01 fs for a 1.5 eV electron) is

extremely short, significantly shorter than $\tau_{e\text{-}p}$ (≅ 2 fs at shortest). This means the high-energy quasiparticle tends to relax through the e-e interaction with another Cooper pair. Upon interaction, approximately half of its energy is transferred to another electron. Now a quasiparticle with energy of $E\text{-}2\Delta$ becomes three quasiparticles with energy of $E/2\text{-}2\Delta$, $E/2\text{-}2\Delta$ and 2Δ each. The quasiparticle with energy higher than 2Δ (usually called a hot quasiparticle) continues to break other Cooper pairs through e-e interaction and reduces its energy towards 2Δ by energy steps $E/4\text{-}2\Delta$, $E/8\text{-}2\Delta$, $E/16\text{-}2\Delta$ etc, leading to a fast avalanche multiplication of non-equilibrium quasiparticles. The characteristic time of this process is on the order of femtosecond, which is much faster than the pulse-width of the laser pulse (≅ 100 fs). Therefore, the generation of quasiparticles by laser pulse illumination is regarded as an instantaneous process; and this transient should follow the shape of the laser pulse.

The *e-e* interaction will become slower with decreasing electron energy according to equation (4.1). When the electron energy reaches ≅ 0.1 eV, which corresponds to about four cascading *e-e* interactions by which 16 Cooper pairs are broken by one photon, $\tau_{e\text{-}e}$ is comparable to the smallest $\tau_{e\text{-}p}$ (≅ 2 fs). The thermalization of quasiparticles tends to go through the *e-p* interaction instead of the *e-e* interaction. And the *e-p* interaction will dominate thereafter. Three processes, namely Cooper pair breaking by phonons, quasiparticle recombination by phonon emission, and the phonon escape, are involved in an *e-p* interaction.

In the subsequent process, the electrons and phonons reach equilibrium and are described by the same temperature. A consequential nanosecond decay corresponds to the cooling of the electrons and phonons, and is determined by the phonon escape from the

film to the substrate. If required, on an even longer time scale, film cooling is through phonon diffusion into the substrate.

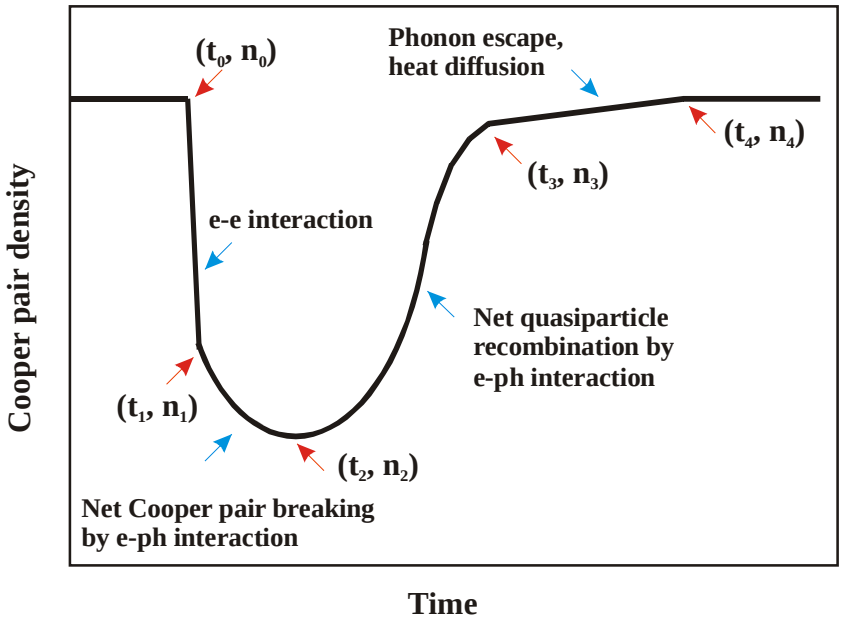

Figure 4-1 A schematic illustration of the Cooper pair density as a function of time [72].

Accompanying the above physical processes is a photon-induced Cooper pair or quasiparticle density variation as a function of time, which is the fundamental origin of the optical response. Figure 4-1 shows qualitatively the variation of Cooper pair density with time. In this illustration, a laser pulse is assumed to have zero pulse-width and hit the sample at time t_0^-. At time t_0, absorbed photons begin breaking Cooper pairs and hot quasiparticles are generated. These hot quasiparticles keep breaking Cooper pairs through *e-e* interaction until time t_1, when *e-p* interaction starts to dominate. As a result, from t_0 to t_1, the Cooper pair density decreases quickly with a time scale on the order of femtoseconds. After t_1, quasiparticles continue to be generated at a slower rate through *e-p* interaction. Finally at t_2, quasiparticle recombination dominates and the Cooper pair

density stops decreasing. At time t_3, electron and phonon subsystems reach the equilibrium. From time t_3 to t_4, the escape of phonons to the substrate dominates the relaxation process and the Cooper pair density increases very slowly with a time scale of nanoseconds. At time t_4, the Cooper pair density is back to n_0. Note that Figure 4-1 is not drawn to the scale and is for illustration purposes only.

4.1.2 Theoretical Models for Optical Response

In this section we introduce three physical models to explain the optical response signals: kinetic inductance model, two-temperature model, and thermal model.

A. Kinetic inductance model

The kinetic inductance is related to the inertial mass of current carriers. This concept arises from the expression of the total energy E associated with an electric current I carried by particles of mass m and number density n [77].

$$E = \iiint_{all\ space} \frac{1}{2}\mu H^2 dxdydz + \iiint_{conductor} \frac{1}{2} mv^2 ndxdydz , \qquad (4.7)$$

where μ is the permeability, H is the magnetic field, and v is the velocity of the particle. If μ, n, m are independent of H and I, and $I = nev\sigma$, we can write the above equation as

$$E = \frac{1}{2} L_m I^2 + \frac{1}{2}[\frac{m}{ne^2}\frac{l}{\sigma}]I^2 , \qquad (4.8)$$

where l, is the length, σ is the cross-sectional area of the device, and L_m is the magnetic inductance. L_m depends only on the geometry of the device [77] and is not affected by laser illumination; hence it will not contribute to the optical response signal given that the

current is constant. The kinetic inductance is defined as the quantity inside the parentheses of the second term in equation (4.8),

$$L_k = \frac{m}{ne^2}\frac{l}{\sigma}. \tag{4.9}$$

The kinetic inductance of a common conductor can be neglected in that compared to resistance, the kinetic inductance induced reactance is very small. The explanation is as follows. From the Drude model, the resistance of a conductor is given by

$$R = [\frac{m}{ne^2}\frac{l}{\sigma}]\cdot\frac{1}{\tau}, \tag{4.10}$$

where τ is the electron collision time. The kinetic reactance of the same conductor is given by

$$\omega L_k = [\frac{m}{ne^2}\frac{l}{\sigma}]\cdot\omega. \tag{4.11}$$

Comparing equations (4.10) and (4.11), we observe that for a conductor only when $\omega > 1/\tau$ will the kinetic reactance dominate the resistance, requiring a frequency as high as 10^{13} s^{-1}. However, for a superconductor where $\tau \to \infty$ and $R = 0$, the kinetic reactance dominates resistance at any frequency ω. Therefore, the kinetic inductance is measurable in a superconductor. It will be shown later that this kinetic inductance is a key component responsible for the fast optical response of superconductor films.

For a superconductor stripe with length *l*, width *w*, and thickness *d*, the kinetic inductance can be expressed as any of the following [5]:

$$L_k = \frac{m}{n_{sc} e^2}[\frac{l}{wd}]$$

$$L_k = \mu_0 {\lambda_L}^2 [\frac{l}{wd}]$$

$$L_k = \frac{1}{\varepsilon_0 {\omega_{p_{sc}}}^2}[\frac{l}{wd}] = \frac{1}{\varepsilon_0 {\omega_p}^2}[\frac{1}{f_{sc}}][\frac{l}{wd}], \tag{4.12}$$

where λ_L is the temperature dependent London penetration depth, ω_p is the plasma frequency, n_{sc} is the Cooper pair density, which can be related to the quasiparticle density n_{qp} by

$$n_{sc} = n_0 - n_{qp}, \tag{4.13}$$

where n_0 is the density of all carriers. f_{sc} is the superfluid fraction and defined as

$$f_{sc} = \frac{n_{sc}}{n_0} = \frac{n_0 - n_{qp}}{n_0}. \tag{4.14}$$

The forms with λ_L and ω_p are useful since both parameters can be determined more accurately than n_{sc} or m [5].

Laser illumination on a superconducting device results in an abrupt drop of the Cooper pair density, and consequently a change of the kinetic inductance. According to the kinetic inductance model, the optical response, V, is generated due to the photon-induced kinetic inductance change [5],

$$V = I \frac{dL_k}{dt}, \tag{4.15}$$

where I is the constant current bias. By substituting equation (4.12) into (4.15), we obtain:

$$V = I\frac{1}{\varepsilon_0 \omega_p{}^2}\frac{l}{wd}\frac{n_0}{n_{sc}{}^2}(-\frac{dn_{sc}}{dt}) = I\frac{1}{\varepsilon_0 \omega_p{}^2}\frac{l}{wd}\frac{n_0}{(n_0 - n_{qp})^2}\frac{dn_{qp}}{dt}. \qquad (4.16)$$

From equation (4.16), we note that the kinetic inductance induced optical response signal is: (1) proportional to the biased current; (2) proportional to the time derivative of quasiparticle density or Cooper pair density; that is, this signal directly measures the Cooper pair breaking rate (dn_{sc}/dt), which is a physical parameter of great interest; (3) characterized by the bi-polar feature since it is proportional to the derivative of Cooper pair density as illustrated in Figure 4-1.

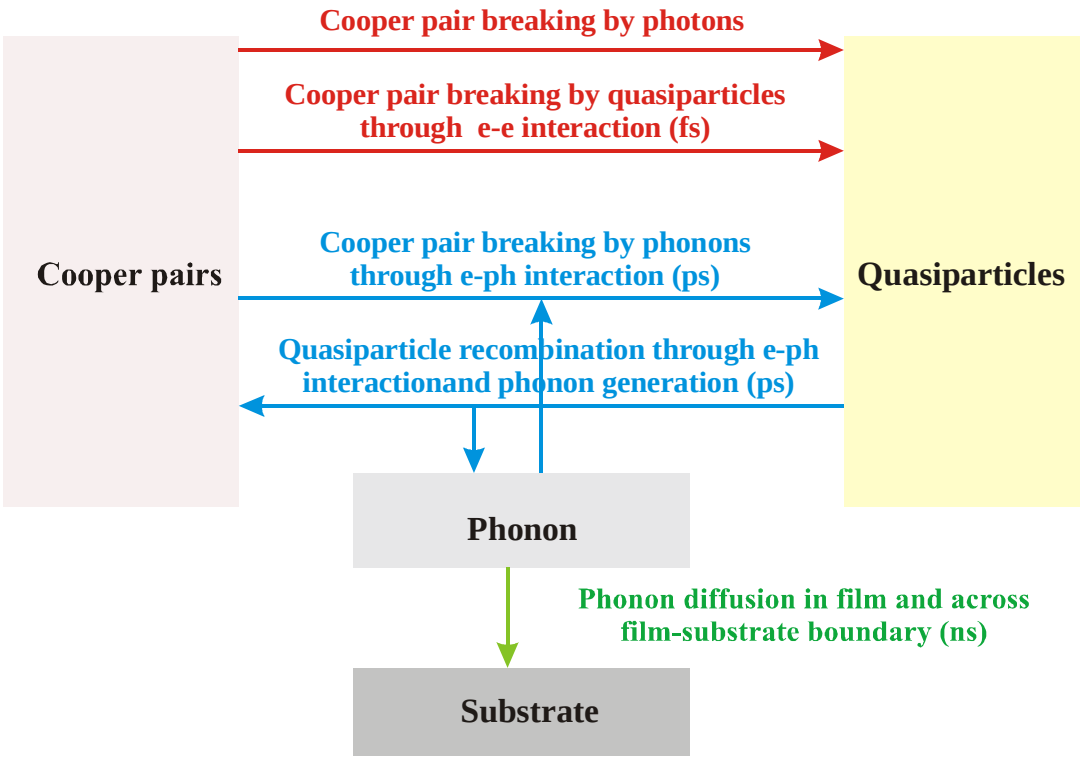

Figure 4-2 A schematic of the interactions between photons, Cooper pairs, quasiparticles, and phonons.

The quasiparticle (or Cooper pair) density as a function of time, $n_{qp}(t)$, needs to be derived in order to obtain the kinetic inductance induced optical response signal. A quantitative solution of $n_{qp}(t)$ can be obtained with the Ruthwarf and Taylor (R-T) equations [78],

$$\begin{aligned} \frac{dn_{qp}}{dt} &= i_{qp}(t) - Rn_{qp}^{\ 2} + \frac{2}{\tau_b} n_\omega \\ \frac{dn_\omega}{dt} &= \frac{1}{2} Rn_{qp}^{\ 2} - \frac{1}{\tau_b} n_\omega - \frac{1}{\tau_{es}} (n_\omega - n_{\omega T}) \end{aligned} . \qquad (4.17)$$

The R-T equations describe the non-equilibrium process embedded in the interactions among quasiparticles, Cooper pairs, and phonons, as illustrated in Figure 4-2. It is well suited for experimental conditions such as a low temperature far below T_c or a low laser power, where the non-equilibrium quasiparticle density is significantly small compared to total carrier density. Here $n_{qp}, n_\omega, n_{\omega T}$ are the density of quasiparticles, phonons and equilibrium phonons respectively. $i_{qp}(t)$ is the quasiparticle generation rate per unit volume due to laser excitation, which is determined by both the Cooper pair breaking by photons and the following cascading process through *e-e* interactions. τ_b and τ_{es} are the Cooper pair breaking time and the phonon escape time respectively. τ_b is on the order of picoseconds [79] and τ_{es} is on the nanosecond level [5]. R is the quasiparticle recombination rate, which is related to the quasiparticle recombination time τ_r through

$$R = \frac{1}{\tau_r n_{qpT}}, \qquad (4.18)$$

where n_{qpT} is the thermal equilibrium quasiparticle density and given by [80]

$$n_{qpT}(T) = n_0[\frac{T}{T_c}]^2 . \qquad (4.19)$$

$n_{\omega T}$ is obtained by solving the R-T equations in steady state in absence of laser illumination,

$$n_{\omega T} = \frac{\tau_b}{\tau_r} n_{qpT} . \qquad (4.20)$$

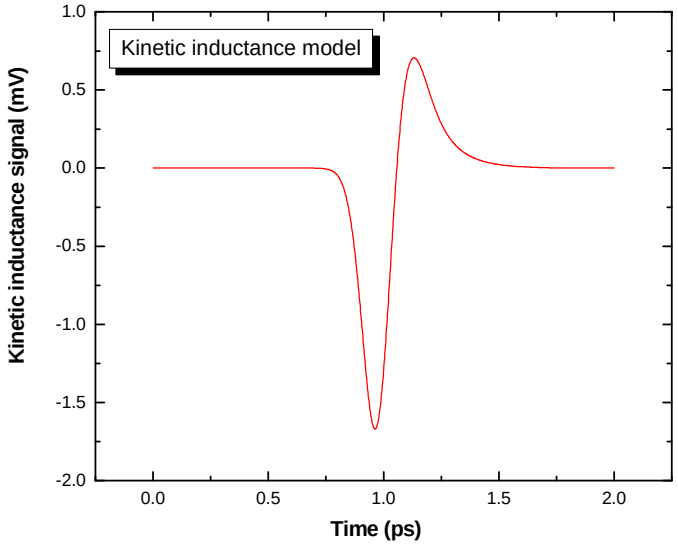

Figure 4-3 Numerical simulation of the non-equilibrium kinetic inductance model based on the R-T equations.

By numerically solving the R-T equations, we obtain the quasiparticle density as a function of time and therefore the kinetic inductance induced optical response signal. Numerical simulation is carried out to solve the R-T equations with the Runga-Kutta method (see Appendix A). In the simulation, the laser pulse is assumed to be Gaussian distributed with a pulse-width of 100 fs. The Cooper pair breaking time τ_b, quasiparticle

recombination time τ_r, and phonon escaping time τ_{es} are 1.0 ps, 0.6 ps, and 3.5 ns respectively [69, 81]. The plasma frequency of YBCO is $\omega_p = 1.67 \times 10^{15}$ s^{-1}. The estimation of the photon-induced quasiparticle generation rate per unit volume, $i_{qp}(t)$ (in unit of $\frac{\#}{s \cdot m^3}$), is discussed in Appendix B.

Figure 4-3 shows a simulated optical response signal according to the non-equilibrium kinetic inductance model based on the R-T equation. Clearly, the characteristic feature of the kinetic inductance induced response is a bi-polar waveform, where negative and positive parts represent the Cooper pair breaking and recombination respectively. The optical response signal takes a negative or positive maximum magnitude when either the Cooper pair breaking or recombination rate reaches its maximum respectively.

We notice that the theoretical simulation shows that the bipolar kinetic inductance induced fast optical response has the time scale of less than one picosecond. Then a consequent question is whether we still can observe such a short bipolar waveform in our experiment with limited detection bandwidth of the electronic detection devices (including the superconductor transmission line, the coaxial cable and the sampling oscilloscope)? The answer is positive. It can be shown that, by taking into account of the dispersion of the transmission line, the bandwidth limitation of the oscilloscope, and the finite laser focusing spot size (a few millimeters), the bipolar transient signal will be stretched to tens of picoseconds in duration but still preserve its bi-polar feature. This will be further discussed when we present the experimental results later in section 4.2.

B. Two-temperature model

When either the laser power or the temperature of the superconductor film increases, the ratio of the photon-induced Cooper pair density change to the total Cooper pair density at equilibrium at a certain temperature T, $\frac{\Delta n_{sc}}{n_{sc}(T)}$, increases. In this case, an abundance of quasiparticles makes the interaction between Cooper pairs and phonons insignificant. For example, there may not be any Cooper pairs left for phonon to break. The R-T equation, which completely depends on the Cooper-pair/phonon interaction, is no longer valid. And the two-temperature model is introduced to describe the optical response.

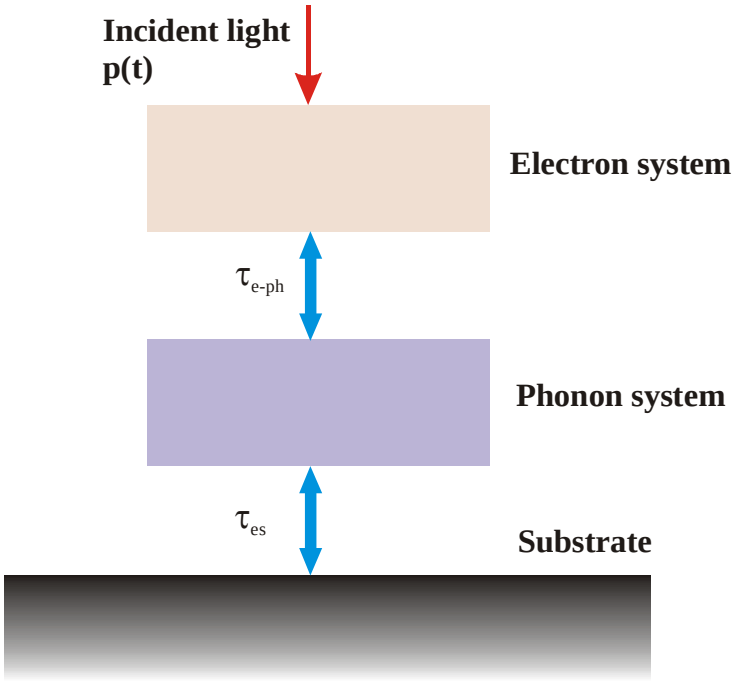

Figure 4-4 A schematic diagram of heat flow in the two-temperature (2-T) model [82].

According to the two-temperature (2-T) model [69], with laser illumination, the superconducting system is split into two sub-systems, electron and phonon sub-systems. Each sub-system has its own temperature, T_e and T_{ph} for the electron and phonon sub-

systems respectively. Electron temperature T_e will relax through *e-p* interaction. This interaction is governed by coupled linear heat balance equations,

$$\begin{aligned} C_e \frac{dT_e}{dt} &= p(t) - \frac{C_e}{\tau_{e-ph}}(T_e - T_{ph}) \\ C_{ph} \frac{dT_{ph}}{dt} &= \frac{C_e}{\tau_{e-ph}}(T_e - T_{ph}) - \frac{C_{ph}}{\tau_{es}}(T_{ph} - T_s) \end{aligned} . \qquad (4.21)$$

C_e and C_{ph} are heat capacities of electrons and phonons respectively, with units of $\frac{J}{m^3 K}$. $p(t)$ is the absorbed optical radiation per unit volume as a function of time, in units of $\frac{W}{m^3}$. $\tau_{e\text{-}ph}$ is the characteristic time of *e-p* interaction. τ_{es} is the time for phonons to escape to the substrate. T_s is the temperature of the substrate which serves as a heat sink. The schematic diagram of heat flow in the 2-T model is shown in Figure 4-4.

By numerically solving the 2-T equation, we obtain T_e as a function of time, which is easily related to the optical response signal. The explanation is as follows. When T_e is above T_c, superconductor film is pushed into its resistive state, leading to a voltage drop across the superconductor device. Assuming that the electron temperature (T_e) dependence of the resistance R and the thermal equilibrium temperature (T) dependence of the resistance R of the superconducting thin film in the transition region are the same, we obtain [69],

$$R = \frac{R_n}{1 + e^{-4(T_e - T_c)/\Delta T_c}}, \qquad (4.22)$$

where R_n is the resistance of the film in normal state and ΔT_c is the width of the transition temperature. Thus the resulting optical response signal can be expressed as

$$V = IR\,. \qquad (4.23)$$

We note the optical response based on 2-T model is: (1) proportional to the biased current; and (2) characterized by a uni-polar feature in that the larger the T_e, the larger the V according to equations (4.22) and (4.23).

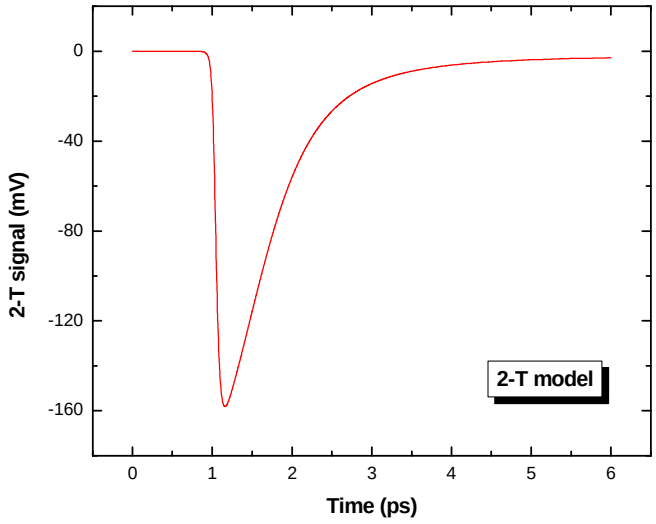

Figure 4-5 Numerical simulation of the two-temperature model.

Numerical simulations of the optical response based on 2-T equations are carried out with Runga-Kutta method. The estimation of the initial condition, the absorbed optical radiation per unit volume as a function of time $p(t)$, is discussed in Appendix C. In the simulations, the heat capacities C_e and C_{ph} are taken to be 0.022 and 0.836 J/cm^{3}K respectively [69]. $\tau_{e\text{-}ph}$ and τ_{es} are 2.0 and 3.5 ns respectively [69]. The width of the superconducting transition temperature ΔT_c is 2 K. Normal state resistance R_n is assumed to be 1 kΩ.

Figure 4-5 shows a simulated optical response signal according to the 2-T model. Clearly, a characteristic feature of the optical response based on the 2-T model is the uni-polar waveform of optical response, which is slightly delayed with respect to the onset of laser illumination.

C. Thermal model

The kinetic inductance model and the two-temperature model are used to explain the non-equilibrium optical response associated with the non-equilibrium process with laser illumination. After this non-equilibrium process, electrons and phonons reach equilibrium and are at an equal temperature. If this equilibrium temperature is higher than T_c, the superconductor film is pushed to its resistive state. Thus the thermal process, which is related to the relaxation of the equilibrium temperature through phonon diffusion, takes over. Basically, there are three processes associated with the thermal diffusion: (1) phonon diffusion within the film, (2) phonon diffusion across the film/substrate boundary, and (3) phonon diffusion within the substrate. In section 4.1.1, we have already introduced the time constants corresponding to these three thermal processes, τ_{diff}, τ_{esc}, and $\tau_{diff\text{-}sub}$. Process (3) is insignificant since for optical response it is the temperature of the superconductor film that matters. The heat diffusion in the film is a very complicated process since heat can diffuse in any direction. Together with the fact that the current distribution in a thick film is non-uniform, it is very difficult to develop a numerical solution to the thermal model.

For optically thin films, where the film thickness is less than the optical penetration depth, the laser is absorbed at any depth through out the whole film.

Therefore process (1) is not notable and only process (2) is important. However, for optically thick films, both processes (1) and (2) are important.

4.2 Optical Response of YBCO Films with Various Thicknesses

In this section, optical responses of YBCO thin films with different thicknesses will be studied systematically. Five films with thicknesses of 50 nm, 100 nm, 200 nm, 400 nm, and 700 nm are deposited to study the laser power, temperature, and current dependence of the optical responses.

4.2.1 Waveforms of the Optical Response in YBCO Thin Films

In experiments, we observe that the shapes of the waveforms of the optical response vary with laser power *P*, temperature *T*, and current *I*. Moreover, the waveforms exhibit different features for optically thin and thick films. It is shown that the waveforms, specifically the thermal component of the optical response, can be classified into two groups according to the film thickness. The waveforms of the 50 and 100 nm films with thickness less than the optical penetration depth ($\delta \cong 120$ nm for YBCO) exhibit identical style, while the waveforms of the 200, 400, and 700 nm films are similar.

For comparison, experimentally obtained waveforms of a 100 nm and a 400 nm YBCO film are presented. The evolution of waveforms with *P*, *T*, and *I* is illustrated. In the meantime we present three featured waveforms and relate them to the theoretical predictions discussed in section 4.1. Good agreement between theoretical models and experimental results is observed.

A. Waveforms of a 100 nm YBCO thin film

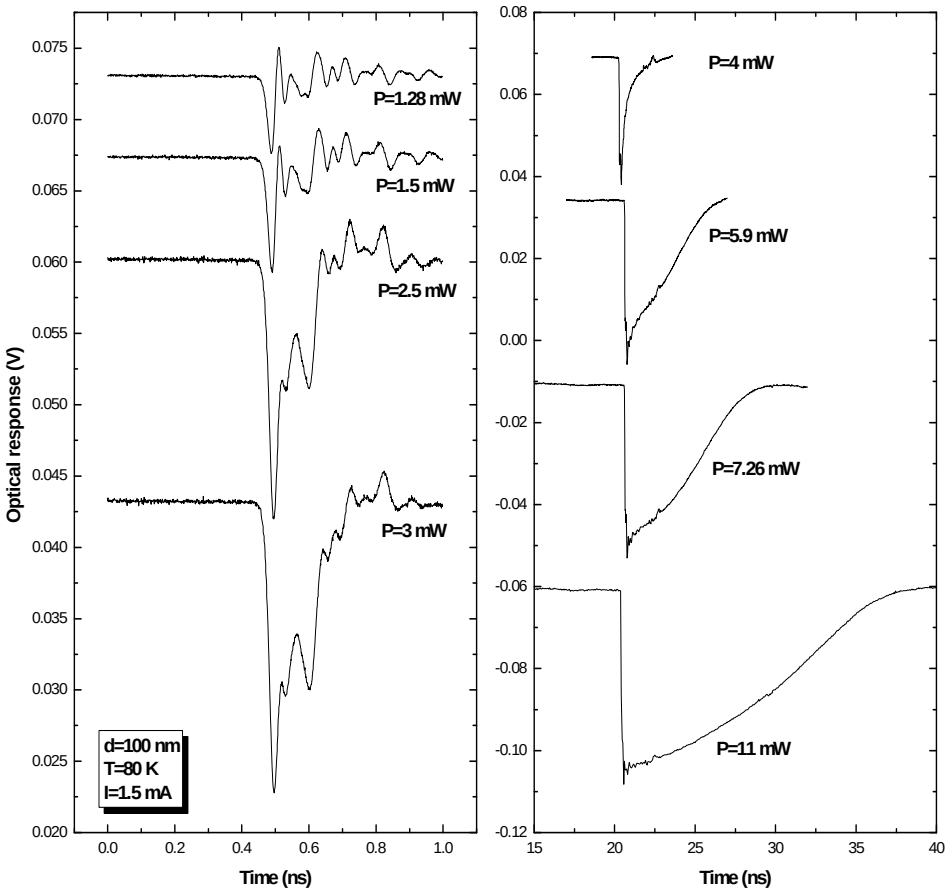

Figure 4-6 Optical response waveforms of a 100 nm YBCO thin film at various laser powers.

Figure 4-6, Figure 4-7, and Figure 4-8 show the observed waveforms for a 100 nm YBCO thin film with different *P*, *T*, and *I*. At a low *P* the optical response shows a bi-polar transient; with an increase of *P* the second peak grows; and finally the thermal signal becomes increasingly prominent and the width of the thermal signal increases with *P*. The temperature dependence waveforms are shown to behave in a similar manner. However, the waveforms do not change significantly for different currents, which can be

explained as follows. Commonly, the bias current influences the waveforms of the optical responses through the T_c of the superconductor device. A higher I results in a reduced T_c [83]. Throughout our experiments, the current change is not significantly large (less than 20 mA), leading to an almost un-changed T_c. Thus, a similar current dependence of the optical response waveforms results.

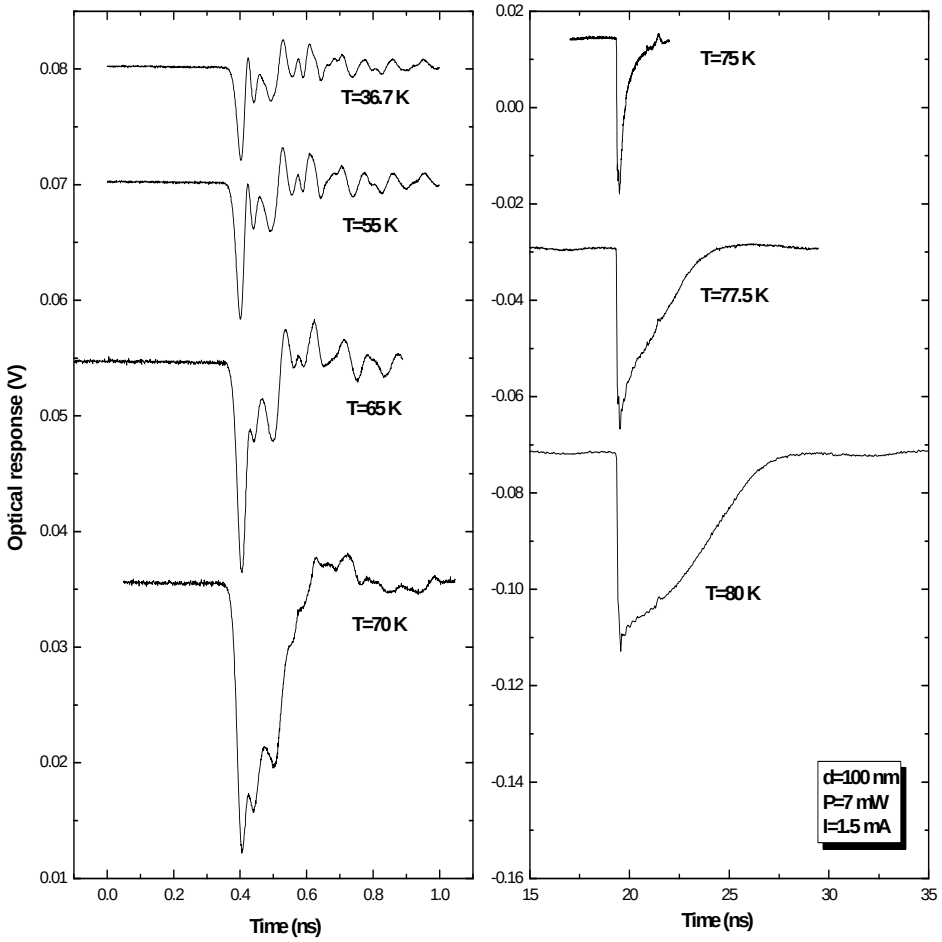

Figure 4-7 Optical response waveforms of a 100 nm YBCO thin film at various temperatures.

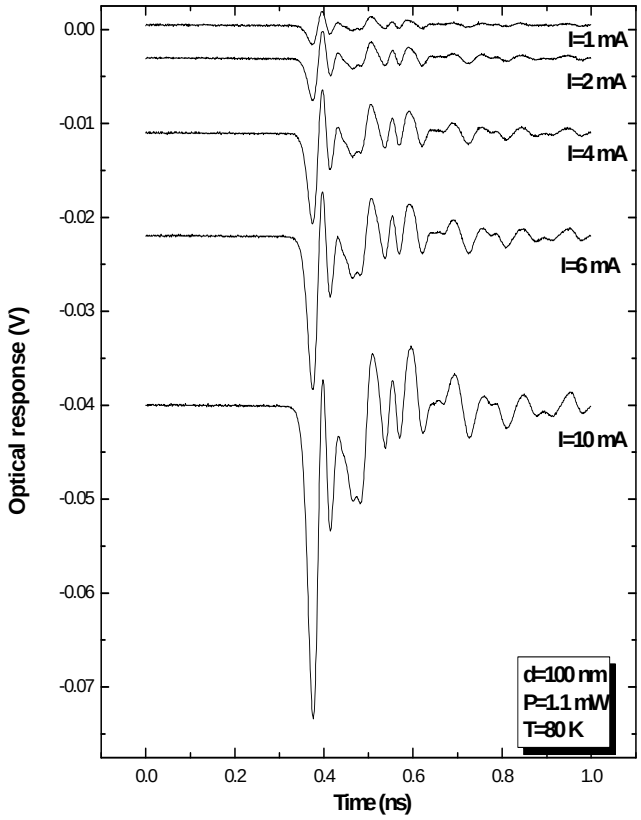

Figure 4-8 Optical response waveforms of a 100 nm YBCO thin film at various bias currents.

Three featured waveforms are picked up from the *P*-series for the following discussion to illustrate their physical origins. Figure 4-9 (a) shows an optical response waveform at a low laser power of P = 1.28 mW. Its bi-polar feature closely matches the characteristic of the kinetic inductance model. The oscillations after the main pulse have also been observed by other groups [5, 79, 84]; however their origins are not well understood. A possible reason is signal reflection at the discontinuities, after all the characteristic impedance of the transmission line might not be perfectly 50 Ω.

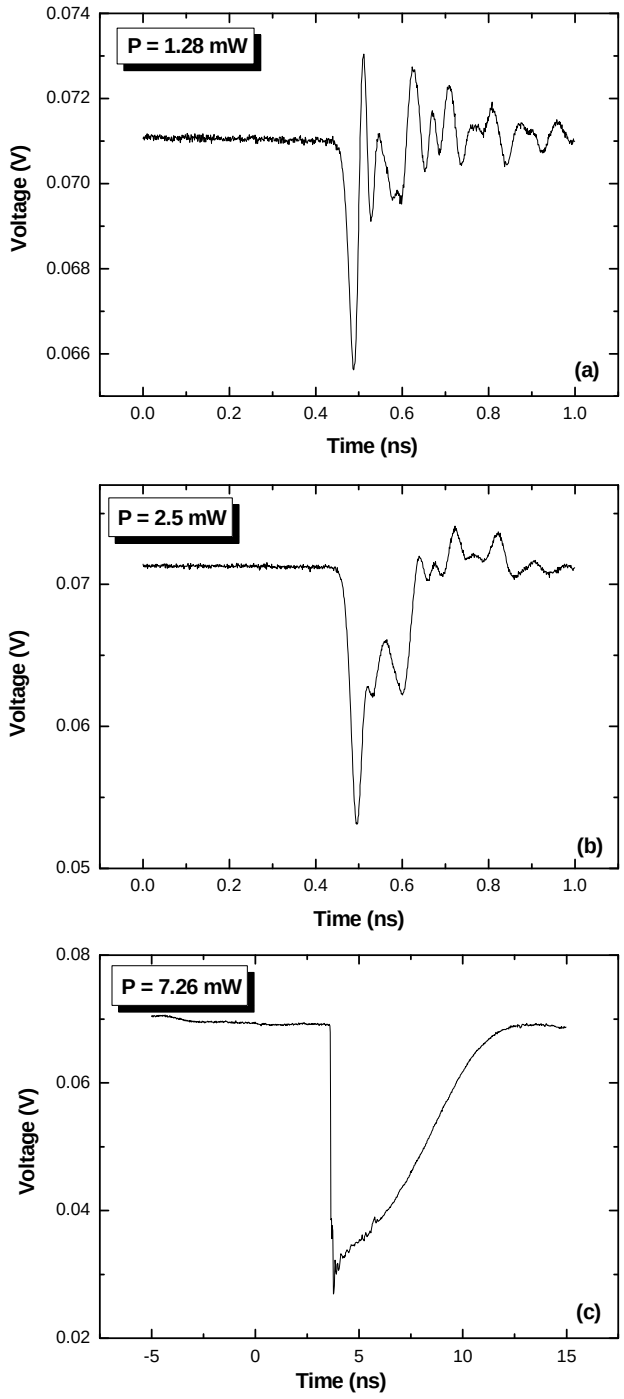

Figure 4-9 Optical response waveforms of a 100 nm YBCO thin film at laser power of (a) P = 1.28 mW, (b) P = 2.5 mW and (c) P = 7.26 mW, temperature T = 80 K, bias current I = 1.5 mA.

Figure 4-9 (a) clearly illustrates that although the kinetic inductance induced fast optical response signal is stretched or broadened due to the dispersion of the transmission line, the finite width of the laser spot, and the limited time resolution of the oscilloscope, its bipolar feature is still preserved. In the following we carry out simple simulations to illustrate this point. We first consider the dispersion of the signal. The fast optical response signal is inevitably broadened while propagating along the transmission line – including both the superconductor transmission line and the 20 GHz cable. Calculations in reference [85] revealed that short pulses with a FWHM width of 1 ps or 400 fs are stretched to several picoseconds after traveling for several millimeters along a coplanar superconductor transmission line. The 20 GHz high-speed cable causes additioanl dispersion. Therefore we assume that after taking into account the dispersion of the transmission line, the original optical signal (refer to Figure 4-3) is stretched to tens of picoseconds. Here we select pulse-width of ≅ 15 picoseconds (curve A, Figure 4-10) to best fit the experimentally obtained result. In addition, the finite length of the focusing spot (≅ 2 mm) could further stretch the optical response pulse (curve B, Figure 4-10). Finally, the finite bandwidth of the digital sampling oscilloscope makes its own contribution to the broadening of the pulse. We use equations (3.12)-(3.14) to simulate this oscilloscope induced pulse broadening, with f_H = 20 GHz. The simulation result is shown in curve C, Figure 4-10. Clearly the bipolar structure is preserved. We compare this simulated output optical response on oscilloscope with a real experimental observed signal. A reasonable qualitative agreement was obtained, as shown in Figure 4-11, for a 100 nm YBCO film with laser power P = 1.28 mW, I = 1.5 mA, T = 80 K.

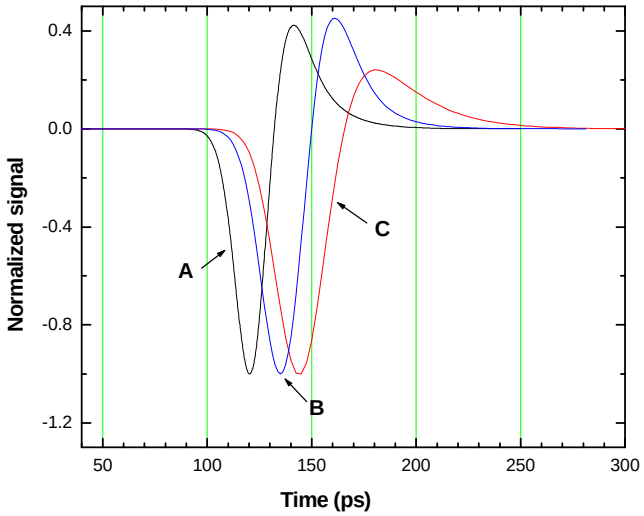

Figure 4-10 Illustration of the pulse broadening due to the finite focusing spot and the limited bandwidth of the oscilloscope. Curve A: The assumed optical response signal after considering the dispersion. Curve B: The optical response signal after considering the 2 mm long finite laser focusing spot. Curve C: The expected signal on an oscilloscope.

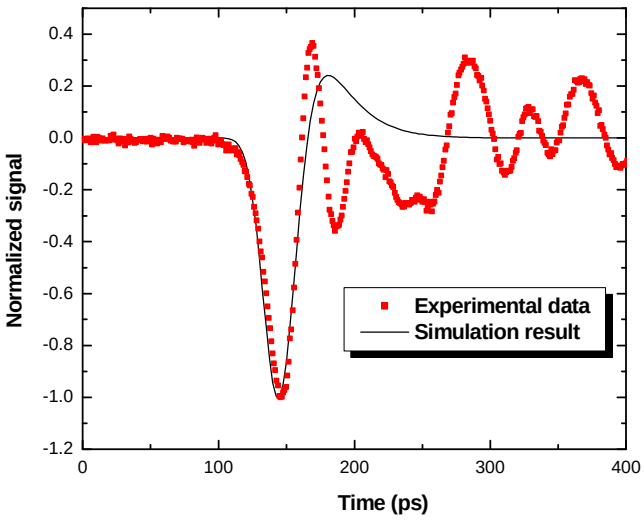

Figure 4-11 The kinetic inductance induced optical response on oscilloscope: a simulation result and an experimental result.

When laser power increases to an intermediate level such as P = 2.5 mW, a second peak appears, as shown in Figure 4-9 (b). Such a waveform can be regarded as the superposition of a kinetic inductance waveform and a 2-T waveform. The 2nd peak is therefore corresponding to the 2-T response. Can this 2nd peak be due to the thermal diffusion process within the film? The answer is no. Compared to both the ≅ 100 ps time separation between the 1st and 2nd peak and the hundreds of picoseconds of the pulse-width of the optical response signal, the nanoseconds time constant of a thermal process [86] is considerably large. Furthermore, if this 2nd peak does relate to heat diffusion, it should vary as a function of film thickness. However, this dependence is not observed in our experiments. The position of this 2nd peak is the same for all 50, 100, 200, 400, and 700 nm films. Therefore our conclusion is that the 1st peak is explained by the kinetic inductance model while the 2nd peak is accounted for by the 2-T model. This is the explanation most consistent with all of our experimental results.

At a higher average laser power of P = 7.26 mW, the signal with a long tail is observed, as shown in Figure 4-9 (c). The nanosecond time scale of this signal indicates its thermal origin. With a high average laser power, the thermal equilibrium temperature of both quasiparticles and phonons is above T_c. Such high temperature has to relax back to the substrate temperature through the phonon escape. For a thin film with a thickness of 100 nm, which is less than the optical penetration depth, the whole film is illuminated and quasiparticles are generated from the top to the bottom of the film; hence there is almost no heat diffusion within the film. The heat diffusion within the film can be ignored; and the heat relaxation is determined only by the thermal boundary resistance.

Such a slow, long-tail component appears only when the thermal equilibrium temperature is above T_c; therefore high laser power is always required.

In conclusion, the experimentally obtained optical response waveforms for optically thin films are in a good agreement with physical mechanisms discussed in section 4.1. All the physical processes involved in the laser illumination of superconductor film are observed.

B. Waveforms of a 400 nm YBCO thin film

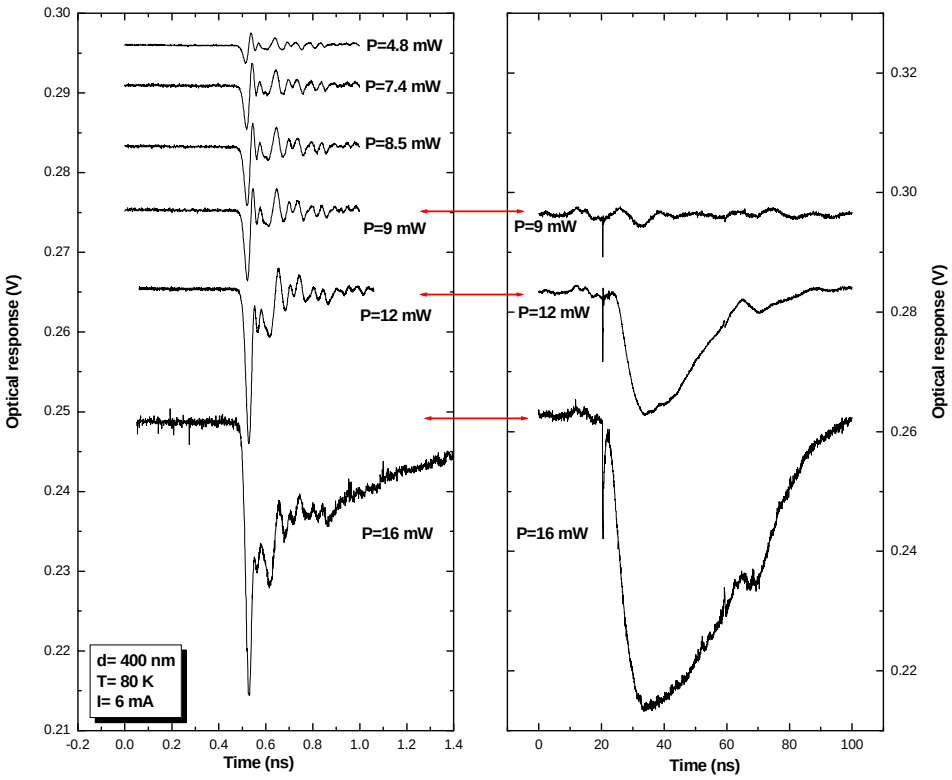

Figure 4-12 Optical response waveforms of a 400 nm YBCO thin film at various laser powers.

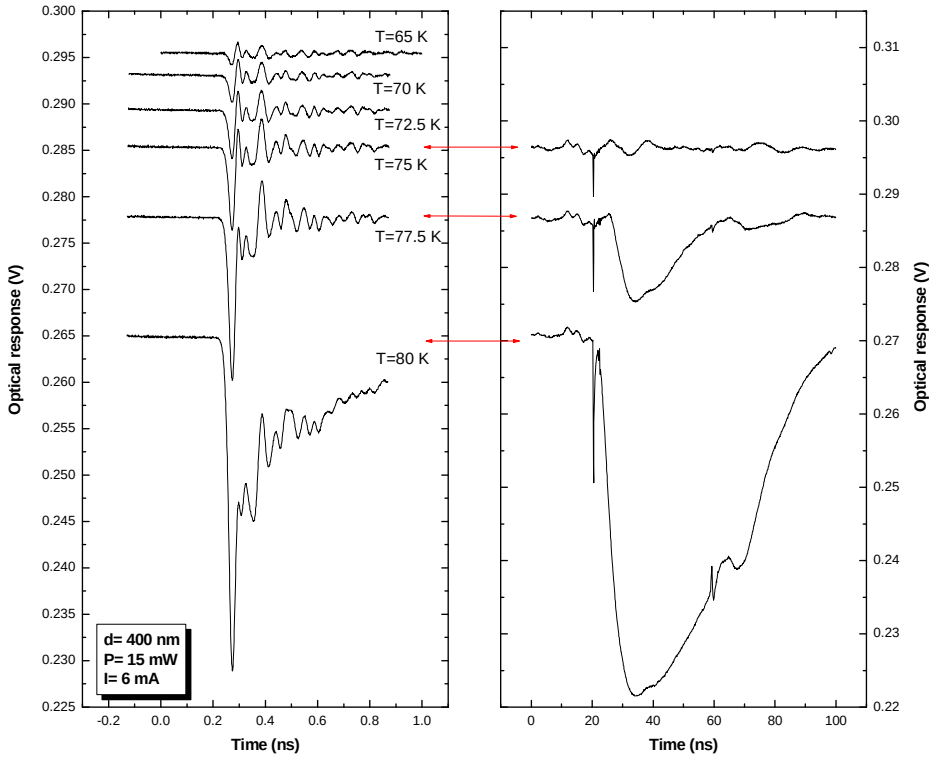

Figure 4-13 Optical response waveforms of a 100 nm YBCO thin film at various temperatures.

Figure 4-12, Figure 4-13, and Figure 4-14 show the *P*, *T* and *I* dependence of the optical response waveforms for a 400 nm YBCO film respectively. The 400 nm thickness is significantly thicker than the 120 nm optically penetration depth so that it is a good representative of optically thick films. Compared with that of optically thin films, the waveforms of optically thick films show different features. Although if only concerning the variation trend of the waveforms, these three figures are consistent with Figure 4-6, Figure 4-7, and Figure 4-8 of a 100 nm film. As shown in Figure 4-12, waveforms at low *P* are similar to those of an optically thin film, showing the bi-polar feature. With an increase of *P*, the bi-polar transient transforms to a 2-peak transient, as we have discussed

for an optically thin film. The difference is in the 3rd peak, which appears when the laser power is ≅ 8 mW. For the waveforms corresponding to P = 8, 12, 18 mW, the figure on the right shows the overall waveform, and the one on the left gives the front part of each waveform. Figure 4-15 shows a typical optical response waveform for an optically thick film, along with definitions to be used in the following discussion. This 3rd peak, which represents the thermal diffusion process, does not exist for an optically thin film because there is no heat diffusion process within the film. Phonons will directly pass across the film/substrate boundary and relax. However for thick films, the generated phonons at the surface of the film have to diffuse all the way down to the bottom of the film and then pass across the film/substrate boundary. It is the heat diffusion within the film that results in the 3rd peak. In Figure 4-15, the part where resistance increases represents a net phonon accumulation, while the one where resistance decreases corresponds to a net phonon escape out of the film. Our experimental data show that the width of the resistance increasing part is almost the same for various laser powers, and the width of the resistance decreasing part increases with an increase in laser power. Assuming the rate of heat diffusion out of the film is constant, a higher laser power requires a longer time to get rid of the heat, and results in a longer resistance decreasing part (or tail). We note that there exists a laser power threshold for the 3rd peak to appear. This phenomenon can be interpreted as follows. An increase in laser power results in an increase in temperature of the superconducting film. If this temperature increase is not sufficiently high, as when the film temperature is below T_c, then no effect can be observed. However, if the film temperature becomes higher than T_c, it is not superconducting any more, and

has a finite resistance. Eventually a voltage signal, which is the 3rd peak, can be observed on the oscilloscope.

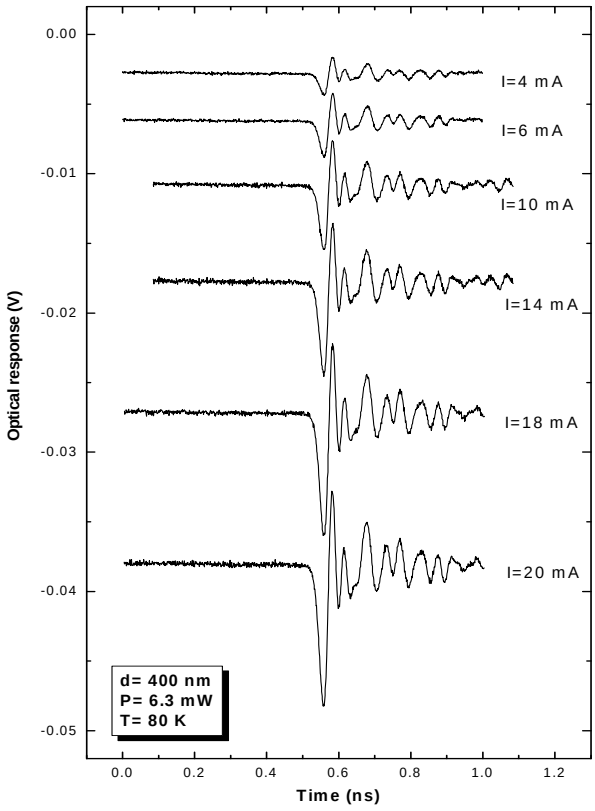

Figure 4-14 Optical response waveforms of a 100 nm YBCO thin film at various bias currents.

It is generally believed that a bi-polar kinetic inductance induced response can only be obtained at a temperature far below T_c, while a thermal response can occur whenever the temperature is close to T_c. However, our *P*, *T*, and *I* data clearly show that this is not true. Actually, even at $T \cong T_c$, we can still obtain a bi-polar response, given low laser power; and at $T << T_c$, a thermal response can also be observed if the laser power is high. Then, what is the parameter that determines the shape of the optical response waveform? Or in other words, through which parameter do *P*, *T*, and *I* affect the shape of

the waveform? We conclude that the shape of the waveform is a function of *P*, *T* and *I*. These three factors together determine the initial condition that finally defines the waveform. This initial condition is based on the ratio of the number of photon-induced changes of Cooper pairs to that of the total number of Cooper pairs originally in the superconducting thin film, $\frac{\Delta n_{sc}}{n_{sc}(T)}$.

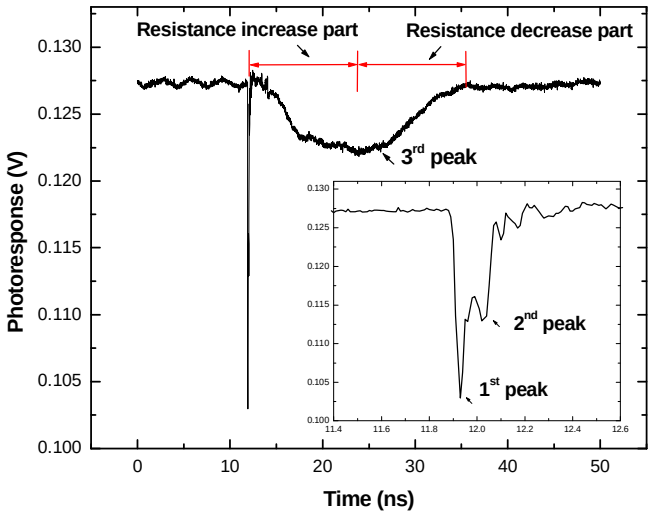

Figure 4-15 A typical optical response waveform of an optically thick YBCO film.

In conclusion, with the TPR experimental setup we observe all of the potential physical processes associated with optical responses. These waveforms show good agreement with theoretical models.

4.2.2 Current Dependence of the Optical Response

Figure 4-16 shows the current dependence of the optical response of an YBCO thin film. The film thickness is 100 nm. The substrate temperature is 80 K. The laser power is either 1.1 mW or 6.3 mW respectively. We measure the amplitude of the 1st

peak. The experimental data is fitted with a linear function. It is evident that the optical response is proportional to the current, which is predicted by the kinetic inductance mode (4.16).

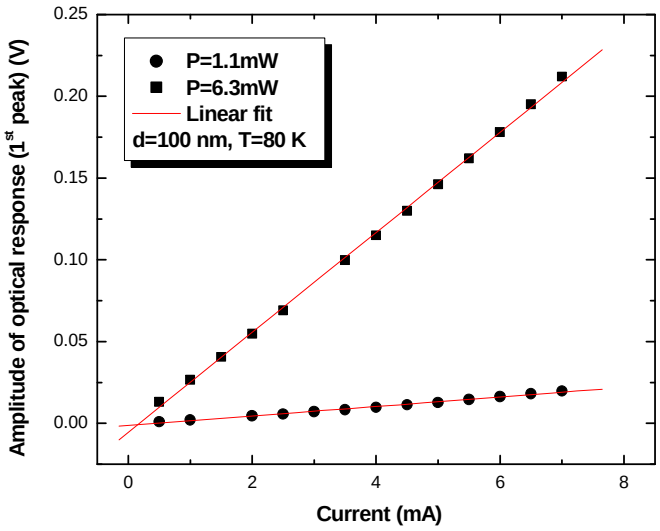

Figure 4-16 Current dependence of the 1st peak amplitude of the optical responses of a 100 nm YBCO film.

4.2.3 Power Dependence of the Optical Response

Figure 4-17 depicts the laser power dependence of the 1st and 2nd peak amplitude of the optical response of a 100 nm YBCO thin film. The amplitude of both peaks initially increases very fast with *P* at a low laser power range, then increases slower when *P* increases, and eventually saturates with a sufficiently high *P*. The physical mechanism behind this observation is as discussed earlier. At low *P*, the number of Cooper pairs broken by laser illumination is much less than the total number of Cooper pairs. The increase in *P* results in the breaking of more Cooper pairs, consequently increasing the 1st peak amplitude. However, when *P* is high enough so that almost all the Cooper pairs are

broken, the increase in *P* will not result in a prominent increase of the 1st peak. Therefore what we observe is a saturated curve. Such a high *P* gives rise to a thermal signal. Although the thermal signal's peak amplitude is almost constant with increased *P*, its width increases with *P*, as clearly shown in Figure 4-18.

Figure 4-19 shows the laser power dependence of the 1st and 2nd peak amplitudes of the optical response of YBCO thin films with different film thicknesses. A similarity is evident for the optical responses of films with different thicknesses. We first examine data for optically thin films – 50 and 100 nm films. Assuming the optical penetration depth δ is 120 nm and the input laser power is P_0, the total power absorbed by a 100 nm or 50 nm film is $0.5654P_0$ and $0.3407P_0$ respectively according to $P_{absorbed} = P_0(1-e^{-\frac{d}{\delta}})$. It's reasonable to assume $\frac{\Delta n_{sc}}{\Delta t} \propto P_0$, therefore $(\frac{\Delta n_{sc}}{\Delta t})_{100nm} = 0.41(\frac{\Delta n_{sc}}{\Delta t})_{50nm}$. We note that the 1st peak amplitude is determined by the kinetic inductance model, where *V* is proportional to $\frac{dn_{ns}}{dt}$ according to equation (4.16). Therefore, at low *P*, the 1st peak amplitude for a 100 nm film should be ≅ 0.41 of that of a 50 nm film. From Figure 4-19 we observe that in the range of low *P* (the initial, linear part of the curve), the slopes of this linear part of the 100 and 50 nm data are 20 and 49.2 mV/mW respectively. The ratio is 0.4, which perfectly matches the above analysis. Our experimental data reaffirm the validity of the kinetic inductance model. On the other hand, the calculations for optically thick films are not feasible due to their high complexity. First, current in a thick film is not uniformly distributed, so that the kinetic inductance equation (4.16) may be invalid. Second, the laser illuminates only the top part of the thick film; and the calculation of the kinetic inductance in this circumstance is a question. Therefore we could not obtain the

numerical relationship among the 200, 400, and 700 nm films. From Figure 4-19, the slopes for the 200, 400, and 700 nm films are 3.65, 1.74, and 0.176 mV/mW respectively. From a responsivity point of view, thinner films are more advantageous being used as a photodetector. Figure 4-20 shows a laser power dependence of the 3rd peak amplitude for YBCO films with different film thicknesses.

We show the total width of the thermal signal as a function of average laser power for films of different thicknesses in Figure 4-21. If we assume that the rate of heat escaping out of the film is the same for both 100 and 50 films, then the width of the thermal signal, which represents the time needed for heat to escape, will be proportional to the laser power. As estimated earlier, the 100 nm film absorbs more laser power than the 50 nm film, and we expect the thermal width of the optical response of the 100 nm film to be less than that of the 50 nm film. For optically thick films where the film thickness is larger than δ, the total absorbed laser power is the same. However, the time required for heat diffusion varies with the thickness of the film. It takes longer to dissipate heat in a 700 nm film than in either a 400 nm or a 200 nm film. Accordingly, the thermal width of a 700 nm film is larger than that of a 400 nm or a 200 nm film.

Figure 4-22 shows the time separation between the 1st and 3rd peak with respect to film thickness. Since the 3rd peak is diffusion related, its position must be scaled with film thickness, which is exactly what we have observed. The curve possesses a highly non-linear feature which may be due to any aspect associated with the diffusion process in an optically thick film, such as the non-uniform distribution of the current density.

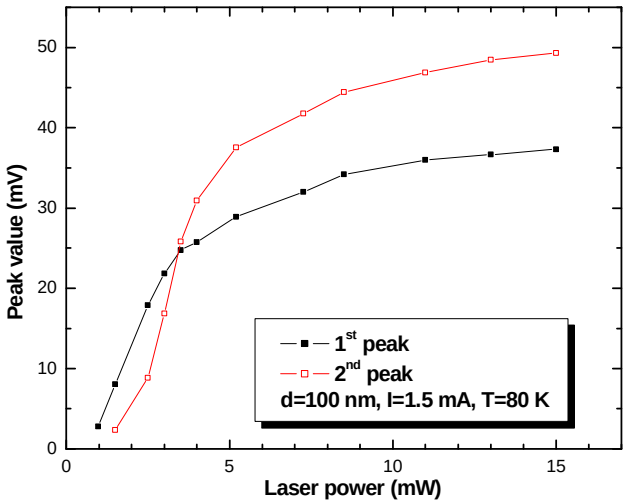

Figure 4-17 Laser power dependence of the 1st and 2nd peak amplitudes of the optical response of a 100 nm YBCO film.

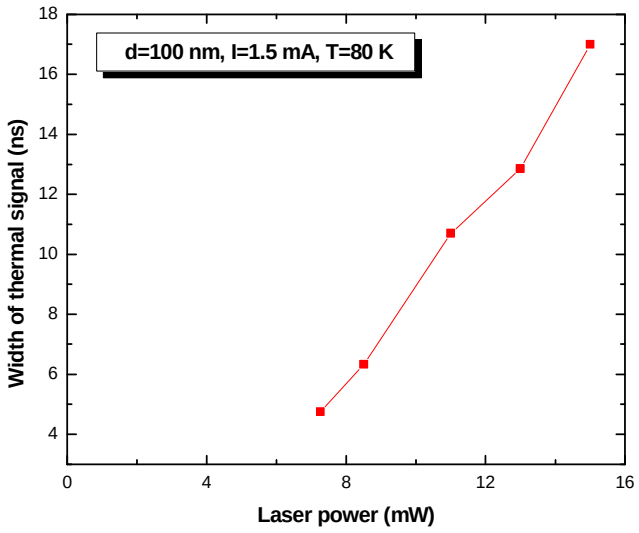

Figure 4-18 Laser power dependence of the width of the thermal optical response of a 100 nm YBCO film.

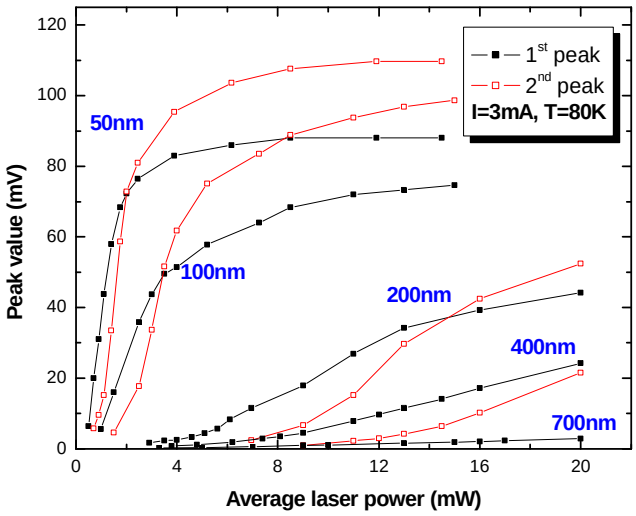

Figure 4-19 Laser power dependence of the 1st and 2nd peak amplitudes of the optical response of an YBCO thin film with various film thickness.

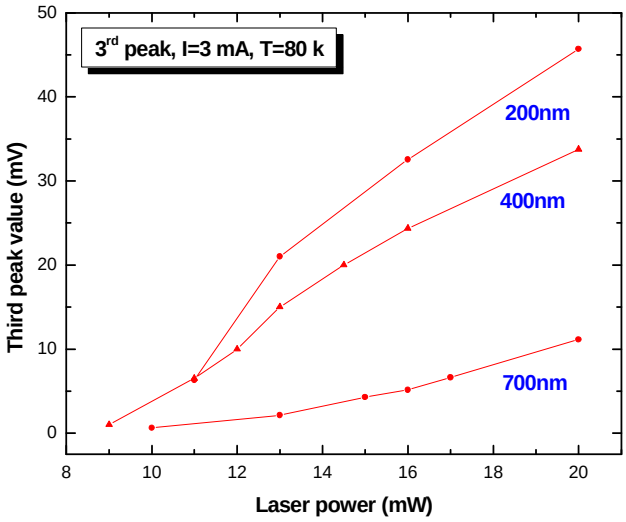

Figure 4-20 Laser power dependence of the 3rd peak amplitude of the optical response of optically thick YBCO films with various thicknesses.

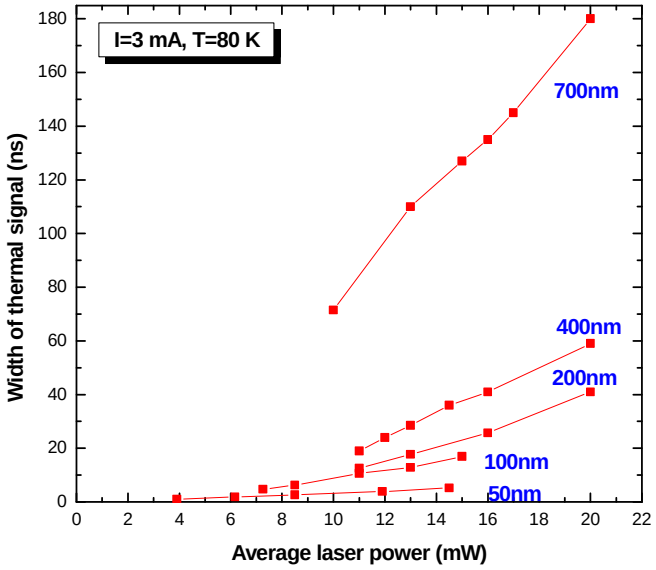

Figure 4-21 Laser power dependence of the widths of the thermal optical response of YBCO thin films with various film thicknesses.

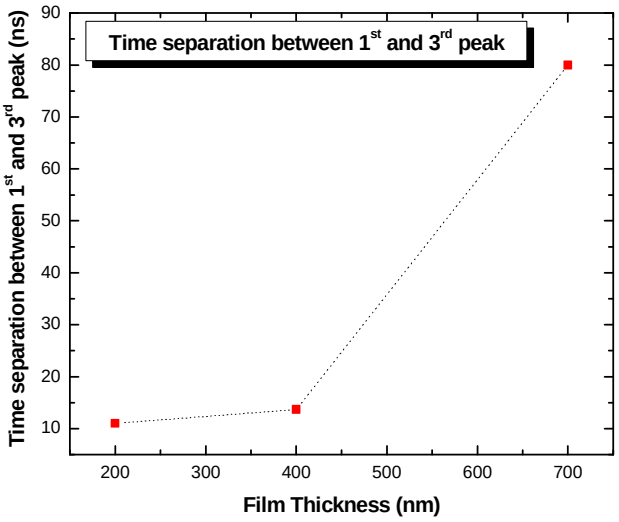

Figure 4-22 Time separation between the 1st and 3rd peak for optically thick YBCO films with various film thicknesses.

4.2.4 Temperature Dependence of the Optical Response

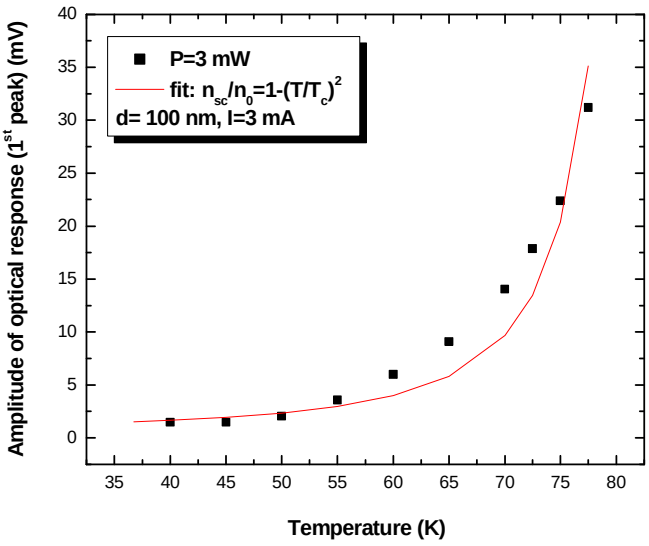

Figure 4-23 Temperature dependence of the 1st peak amplitudes of optical responses of a 100 nm YBCO film.

Figure 4-23 shows the temperature dependence of the 1st peak amplitudes of the optical response for a 100 nm YBCO film. The laser power is carefully controlled so that the kinetic inductance optical response signal dominates. In this figure, the square represents experimental data and the line is a fitting curve. According to the kinetic inductance model, the optical response signal is proportional to $\frac{1}{n_{sc}^{\ 2}}\frac{dn_{sc}}{dt}$. For YBCO, the temperature dependence of the Cooper pair density is given by [80, 87]

$$n_{sc}(T) = n_0 \cdot [1-(\frac{T}{T_c})^2], \qquad (4.24)$$

where n_0 is the density of all carriers. Therefore the relationship between the optical response V and the temperature T can be obtained

$$V \propto \frac{1}{[1-(\frac{T}{T_c})^2]^2}\frac{dn_{sc}}{dt}. \qquad (4.25)$$

If we assume $\frac{dn_{sc}}{dt}$ is a constant – which is reasonable since dn_{sc} is the number of photon-induced broken Copper pairs primarily determined by the input laser power, the experimental data can be fitted to the above equations. The theoretical fitting curve and the experimental data are in a good agreement. High temperatures close to T_c result in a large optical response signal. For this specific sample, T_c is 85 K.

Figure 4-24 (a) shows the 1st peak amplitude of the optical response for a 100 nm YBCO thin film as a function of temperature given various laser powers. It is clear that for a higher laser power, where the thermal optical response signal dominates, the temperature dependence curve is flatter. This is similar to the flat region of the power dependence curve in Figure 4-17. When laser power is low, the kinetic inductance optical response signal dominates. Therefore the temperature dependence curve with P = 3 mW is similar to the front region of the curve in Figure 4-17. For comparison, Figure 4-24 (b) shows the temperature dependence of both the 1st and the 2nd peak amplitudes. It exhibits the same trend as the power dependence data illustrated in Figure 4-19.

Figure 4-25 illustrates the temperature dependence of the 1st and the 2nd peak amplitudes of the optical response of optically thin YBCO films with laser power (a) P = 7 mW (b) P = 3 mW. Figure 4-26 shows the corresponding data for optically thick YBCO films with laser power P = 15 mW. Comparing these figures with Figure 4-19, we note that they show good similarity. This confirms our conclusion: regarding the optical

response, it makes no difference to change P or T. It is the initial value of $\frac{\Delta n_{sc}}{n_{scT}(T)}$ that determines the optical response signal, as stated in section 4.1.2.

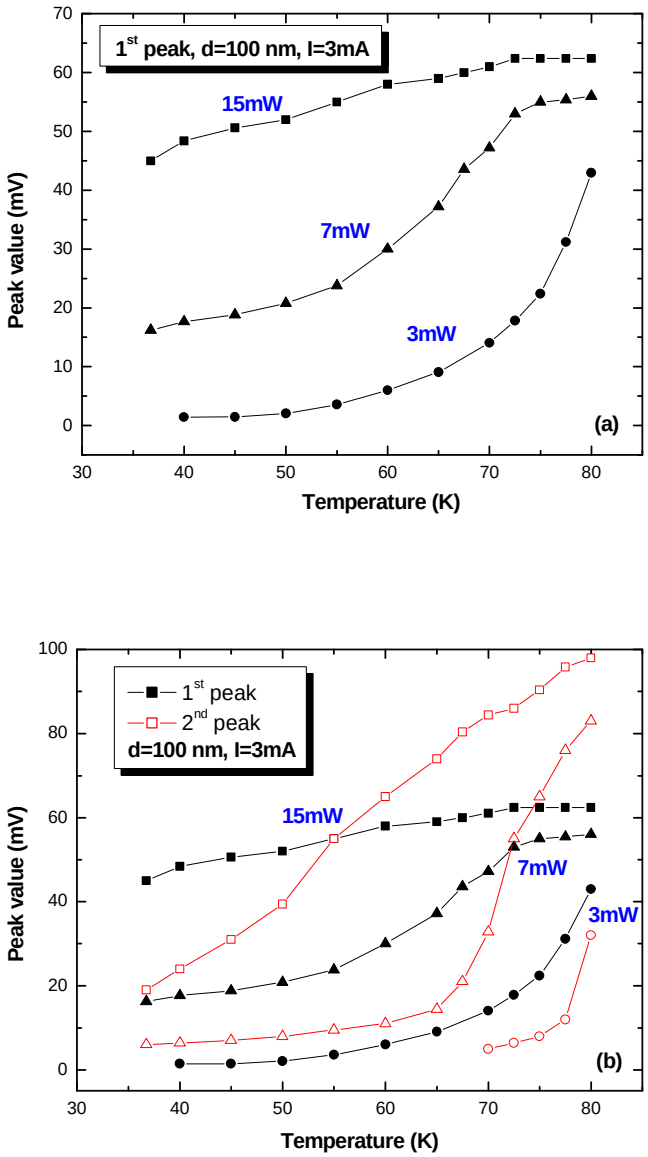

Figure 4-24 Temperature dependence of (a) the 1st peak amplitude, (b) the 1st and 2nd peak amplitudes of the optical response of a 100 nm YBCO film for various laser powers.

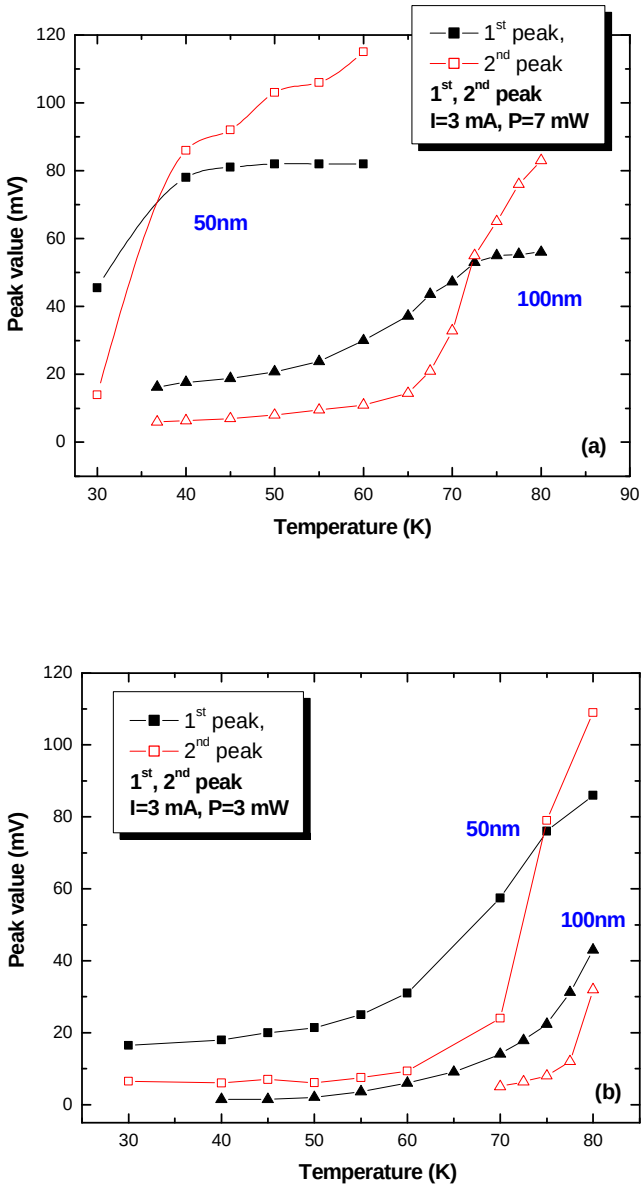

Figure 4-25 Temperature dependence of the 1st and 2nd peak amplitudes of the optical response of optically thin YBCO films with various thicknesses for laser power (a) P = 7 mW, (b) P = 3 mW.

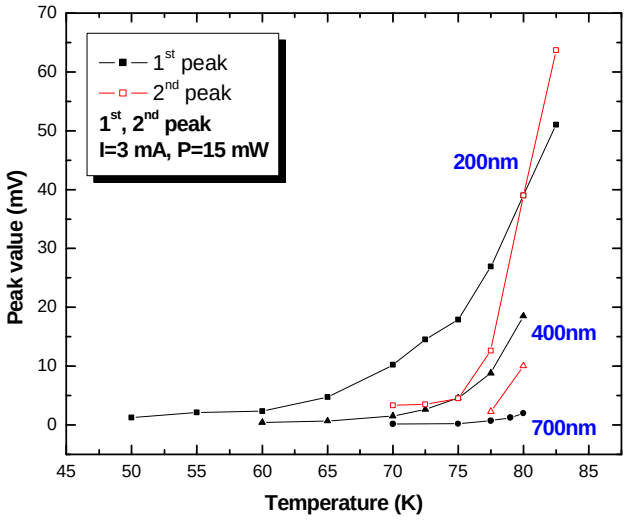

Figure 4-26 Temperature dependence of the 1st and 2nd peak amplitudes of the optical response of optically thick YBCO films with various thicknesses.

4.3 Photon Energy Dependence of the Fast Optical Response of YBCO Films

4.3.1 Motivation

Normal BCS theory, which is based on electron-phonon interaction, does not explain the high superconducting transition temperature of high temperature superconductor materials. According to BCS theory, T_c increases with the energy gap 2Δ, and 2Δ increases with phonon energy [88]; therefore T_c increases with phonon energy. Low-energy phonons are unable to result in a high T_c (for example, above 80 K). W. A. Little proposed that two electrons could form a Cooper pair by interacting with high-energy excitons instead of phonons [7]. This electron-exciton interaction could result in a

much higher superconducting energy gap and hence a high transition temperature. The question is – does this electron-exciton interaction really exist?

From 1994 to 1999, Holcomb *et al.* [8-11] applied thermal-difference reflectance (TDR) spectroscopy to measure the ratio of reflectance in the superconducting state to that in the normal state, R_S/R_N, for photon energies up to ~5 eV in different superconducting materials. A considerable deviation of this ratio from unity is observed for photon energies around 1.5 eV. They claimed that an electron-phonon coupling plus a coupling with an intermediate electronic excitation near 1.5 eV might explain the data. Later in 1997 Stevens *et al.* obtained a similar 1.5 eV spectrum with femtosecond time-resolved spectroscopy, although only limited experimental points were obtained within the energy region of interest [12]. If this 1.5 eV high-energy excitation is indeed associated with Cooper pair formation, will the pairing be strongly affected by illumination of photons with energy close to 1.5 eV? In Holcomb's experiment, the measured quantities are changes of the dielectric constant, which relate to the electron pairing indirectly. Then, is there an approach to observe this high-energy excitation directly, instead of deducing it from dielectric properties? Moreover, in deed what is the mechanism of this 1.5 eV high-energy excitation? All these questions motivate us to conduct the photon energy dependence experiment [89-92].

This part of the thesis work is in collaboration with the Superconductor Research Center at the University of Maryland.

4.3.2 Experimental Results

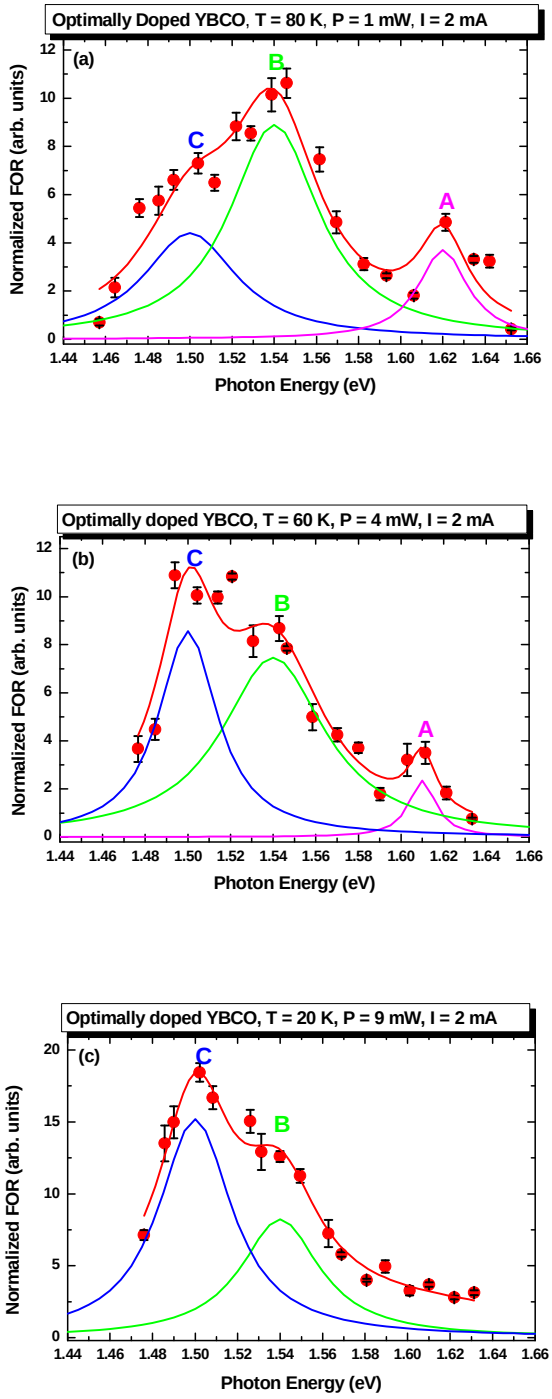

Figure 4-27 Photon energy dependence of the fast optical response in an 100 nm optimally doped YBCO thin film at (a) 80 K, (b) 60 K and (c) 20 K.

The purpose of our work is to conduct a direct *electrical* measurement of Cooper pair breaking with various photon energies. The method we use is the TPR method introduced in Chapter 3. Of our concern is the non-equilibrium Cooper pair breaking process, where optical responses are described by the kinetic inductance model. According to this model, the amplitude of the signal on the oscilloscope is proportional to the Cooper pair breaking rate $\frac{\Delta n_{sc}}{\Delta t}$. Therefore what we measure is the photon energy dependence of the Cooper pair breaking rate. The advantages of this method are: (1) Any other process that is irrelevant to pair breaking has been excluded. (2) Experimental results are directly related to the pairing of the electrons. (3) The experimental setup is simple and has a high signal to noise ratio. The input laser power *P* and substrate temperature *T* are carefully controlled so that only the kinetic inductance based *fast* optical response is obtained. The wavelength of the laser pulse is tuned in an interval of ≅ 5 nm, which corresponds to a 10 meV interval in the photon energy unit. The full width half maximum (FWHM) of the spectrum of the femtosecond laser pulse is ≅ 8 nm, or 15 meV; therefore a small change in wavelength of less than 10 meV is unnecessary. The wavelength is carefully monitored throughout the measurement.

Figure 4-27 (a), (b) and (c) show the photon energy dependence of the fast optical response in a 100 nm optimally doped YBCO thin film at temperatures of 80 K, 60 K, and 20 K, and average laser powers of 1 mW, 4 mW, and 9 mW respectively [89]. The photon energy is tuned ≅ 1.44-1.65 eV, corresponding to a wavelength range ≅ 750-850 nm. The *dc* bias current is 2 mA. Clearly a resonance of the Cooper pair breaking rate with respect to photon energy is observed. Three sub-resonance peaks, A, B, and C, can

be identified in each figure. The solid lines are obtained by fitting the data with an equation modeled as the summation of three Lorentzian functions,

$$Signal = \frac{P_1}{P_2 + (E - E_A)^2} + \frac{P_3}{P_4 + (E - E_B)^2} + \frac{P_5}{P_6 + (E - E_C)^2}. \qquad (4.26)$$

The dotted lines in the figures represent individual Lorentzian functions. At T = 80 K, the peak positions are at E_A = 1.62 eV, E_B = 1.54 eV, and E_C = 1.50 eV. While at T = 60 K and T = 20 K the positions of the peaks remain unchanged within a 10 meV experimental resolution, although the spectral weight of each peak varies. With the decrease of temperature, the contribution of peak C (A) grows (diminishes) with respect to that of B. These resonance features are extremely strong and sharp. The overall resonance range is ≅ 100 meV and the fine structure is ≅ 20-50 meV.

4.3.3 Discussion

We experimentally observe the sharp resonances around 1.5 eV in an optimally doped YBCO thin film. Then, what are these resonances? Why are they so sharp?

For a conventional metal, it is hard to observe such a sharp resonance structure since the electronic bandwidth of metal is on the same order as the Fermi energy, which is hundreds meV or more. However, a narrow spectral width has been reported for excitonic transitions in semiconductors and insulators. Therefore we conjecture that the observed resonances might be related to this phenomenon. If this is true, two questions naturally arise. (1) Is it possible there exist some insulator regions in an optimally doped YBCO, which is supposedly a good conductor? (2) If the answer to question (1) is yes, then is there a ≅ 1.5 eV excitonic transition in those insulator regions in YBCO? The

answer to question (1) is positive according to stripe phase theory. The answer to question (2) is positive as well according to the study of an excitonic transition in an insulator YBCO.

A. Stripe phase theory

A common feature of all high temperature superconductor materials is the Cu-O plane, which is believed to be the reason of a high T_c. The optimally doped $YBCO_7$ is achieved by doping the parent insulating $YBCO_6$ with oxygen. The Cu-O plane of $YBCO_6$ is an anti-ferromagnetic (AFM) insulator, as shown in Figure 4-28. In the Cu-O plane, the oxygen ion is O^{2-} with full *2p* orbit, while the copper ion is Cu^{2+}, with an unpaired electron in *3d* orbit. The reason for being insulator is that the hopping between unpaired electrons is blocked by the on-site Coulomb repulsion. Such AFM ordering has been confirmed experimentally with elastic neutron scattering experiments [93, 94]. When oxygen is doped, some of the Cu^{2+} in the Cu-O plane changes to Cu^{3+}. Compared with Cu^{2+}, Cu^{3+} has one more electron lost, which is analogous to saying that holes are doped into the Cu-O plane. Now the material is no longer an insulator. Conductivity is achieved because electrons can hop from one site to another without fighting the Coulomb repulsion energy. A consequent question is where these holes are doped? Or in other words, where are the Cu^{3+} located? Figure 4-29 illustrates hole doping in insulating $YBCO_6$. Four AFM bonds have to be broken in order to dope one hole. Then how many bonds are broken to dope two holes? There are two possible answers. If these two holes are separated far from each other then eight AFM bonds need to be broken. While if they are adjacent neighbors then only 7 bonds are broken. From an energy point of view, the doped holes tend to gather together in order to minimize the energy required to break the

AFM bonds. Thus, both a hole-rich region and a hole-absence region form. However, on the other hand, doped holes could not be bound together due to the long-range Coulomb repulsion among them [13]. Due to the competition of these two processes, it is more likely that in a doped superconductor some regions are occupied by holes, and some are occupied by AFM insulators. This is the so-called electronic phase separation (EPS). EPS implies an in-homogeneous charge distribution in high temperature superconductors. The stripe phase picture [14] is one form of EPS theory in which holes are assumed to form periodic arrays of one-dimensional charged stripes. These charged stripes are separated by AFM insulator stripes. The fluctuation of the stripes is thought to be essential to superconductivity. The stripe phase theory is supported by experimental results and numerical simulations [95-99].

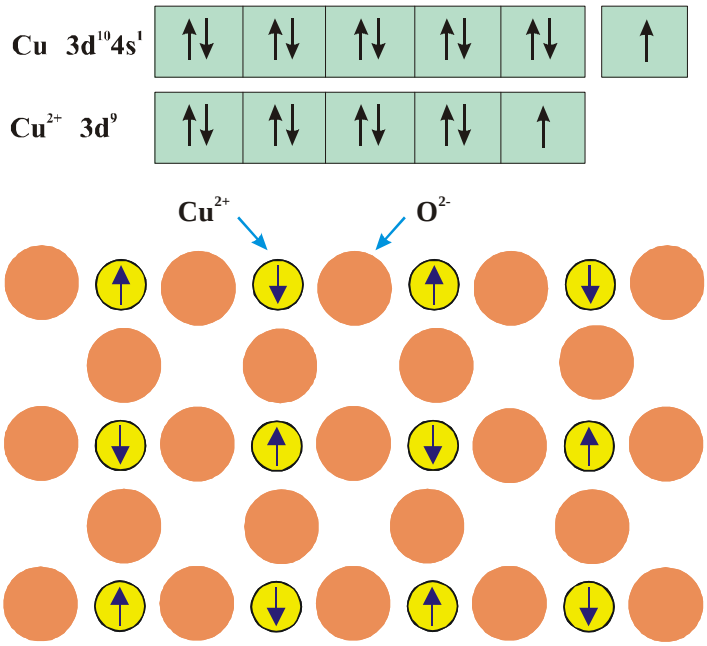

Figure 4-28 The Cu-O plane in insulating $YBCO_6$.

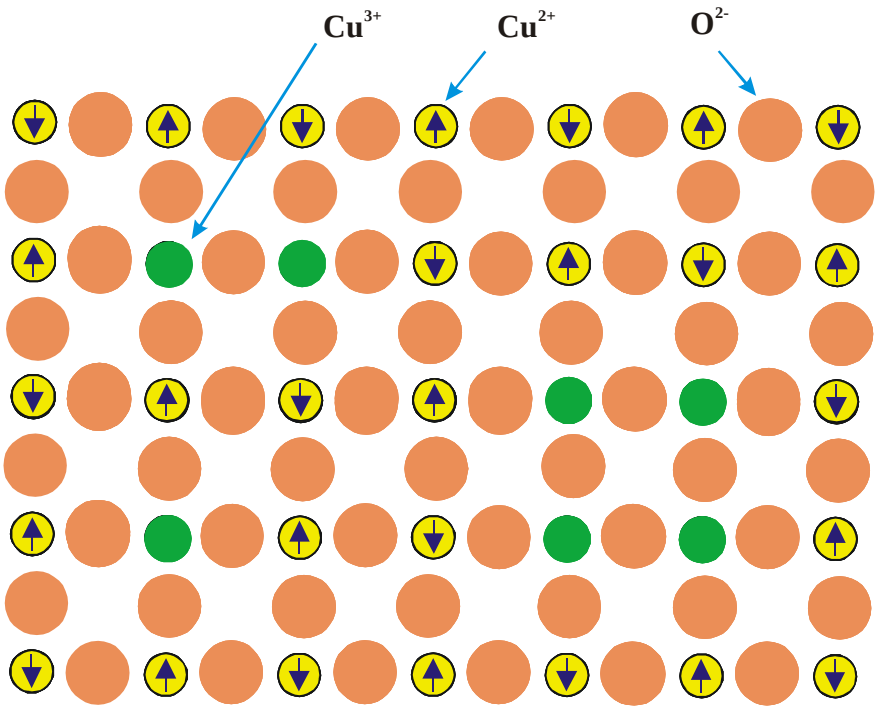

Figure 4-29 A schematic of doping holes in insulating $YBCO_6$.

According to the stripe phase theory, the stripes can move very fast, on the order of 10^{-13} to 10^{-10} s [100, 101]. In our experiment, the ≅ 100 fs laser pulse width is much shorter than this order, giving us the possibility to snapshot these stripes.

In conclusion, stripe phase theory describes a scheme that gives insulator properties to high temperature superconductors that are metallic in nature.

B. Excitonic excitation in insulating $YBCO_6$

For an $YBCO_6$ insulator, an optical absorption measurement indicates that a sharp absorption peak appears at a photon energy around ≅ 1.7 eV [12]. This feature is identified as a charge transfer excitation in which an electron from the oxygen *p* orbit is transferred to the copper *d* orbit in the Cu-O plane. Moreover, a 1.6 eV exciton has been

both calculated [102, 103] and observed [104]. Therefore there does exit an excitonic transition in an insulating $YBCO_6$.

C. Data explanation

With the assumptions that:

(a) The stripe phase theory of high temperature superconductor is accurate and the AFM insulator phase exists in an optimally doped superconducting $YBCO_7$;

(b) An excitonic transition in an insulating $YBCO_6$ exists;

(c) The charge transfer process in AFM stripes in an optimally doped $YBCO_7$ is similar to that in an insulating $YBCO_6$;

(d) AFM stripes in an optimally doped $YBCO_7$ play an important role in the forming of Cooper pairs so that our experimentally obtained Cooper pair breaking rate can be affected by the properties of those stripes,

we conclude that peak A, which is located at 1.62 eV that is slightly below the 1.7 eV charge transfer gap and just at the 1.6 eV excitonic excitation, is associated with this excitonic charge transfer transition.

It is interesting to note that in Figure 4-27 the difference between peak B and peak C is ≅ 40 meV for all three temperatures. This 40 meV separation is notably close to the 41 meV magnetic resonance peak with a 10 meV width observed in the YBCO system [105]. The difference between peak A and peak B is ≅ 75 meV, which is consistent with the energy of longitudinal optical (LO) phonons of ≅ 70-80 meV in the Cu-O plane [106]. The LO phonon is also a sharp excitation with a width on the order of ≅ 10 meV. Therefore peak B can be interpreted as a coupled excitation of the exitonic charge transfer and an ≅ 80 meV LO phonon in the Cu-O plane. Peak C can be explained as a

coupled excitation of the exitonic charge transfer, an ≅ 80 meV LO phonon, and a ≅ 40 meV magnetic resonance.

To ensure that this resonance effect is only associated with Cu-O plane, we also explore the photon energy dependence of the optical response for an oxygen depleted YBCO and a Zn doped YBCO [89]. The resonance of the oxygen depleted YBCO sample shows no difference from that of the optimally doped YBCO. This agrees with our theory since oxygen is only doped in the Cu-O chain, but not on the Cu-O plane of the YBCO. However, the resonance of the Zn doped YBCO shows a 20 meV peak shift with respect to the optimally doped YBCO. This is also expected since Zn is doped in the Cu-O plane, which may affect the resonance process. As an additional proof, a photon energy dependence experiment is carried out to study $La_{1.85}Sr_{0.15}CuO_4$ (LSCO) films. No resonance peak is observed. It can be well explained by the fact that the energy of the charge transfer excitation in LSCO is ≅ 2.0 eV (corresponding to 600 nm) [107], which is far below the tunable range, of ≅ 750-850 nm, of our femtosecond laser system.

4.4 Pump-probe Correlation Measurement of the Fast Optical Response of YBCO Films

4.4.1 Introduction

In section 4.2 we applied the transient photoimpedance response (TPR) method to systematically study optical responses of YBCO thin films. According to the study the optical response can be classified into two categories: kinetic inductance induced fast optical response and thermal effect based slow optical response. In this section we

concern about the measurement of this fast optical response. The theories (refer to section 4.1) predict that the speed of such a fast optical response transient could be as fast as a picosecond. However, the TPR-obtained optical response transient has a ≅ 50 ps pulse-width observed with a sampling oscilloscope. The temporal resolution of the TPR measurement is limited by the bandwidth of this oscilloscope (≅ 20 GHz) and the dispersion of the cable or transmission line. Therefore, the pump-probe technique that offers the ability to time-resolve the ultrafast electrical signal is applied to measure the fast optical response. The pump-probe method is a widely applied method in studying fast phenomena in materials.

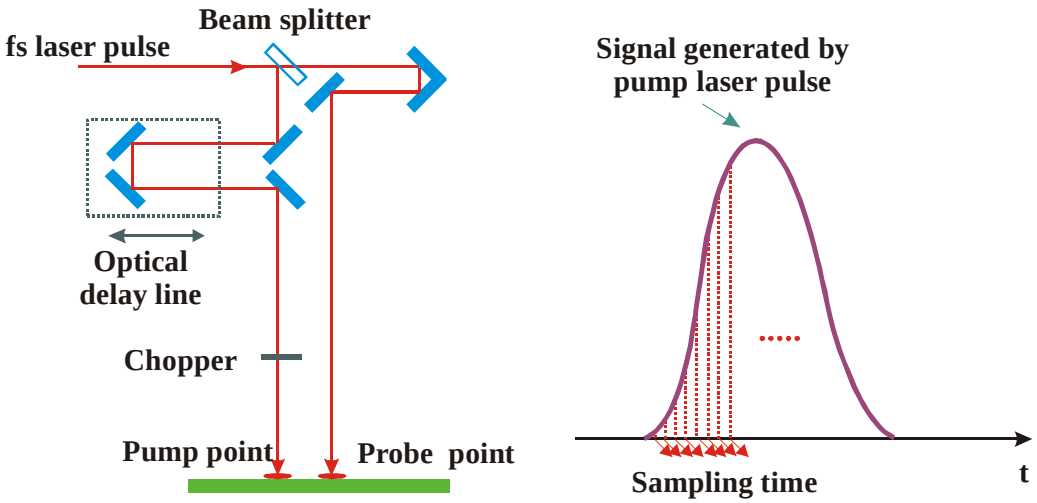

Figure 4-30 A schematic diagram of the pump-probe technique.

A schematic diagram of the pump-probe technique is shown in Figure 4-30. A femtosecond laser pulse is split into two pulses – pump laser pulse and probe laser pulse. The pump laser pulse generates a signal of interest, while the probe laser pulse snapshots such signal at a series of time points with the help of a translator that provides the optical delay between the pump and probe laser pulses. In other words, the function of the probe

laser pulse is to sample. Depending on the specific sampling technique, various pump-probe methods have been utilized to study the fast optical response of high temperature superconducting (HTS) films.

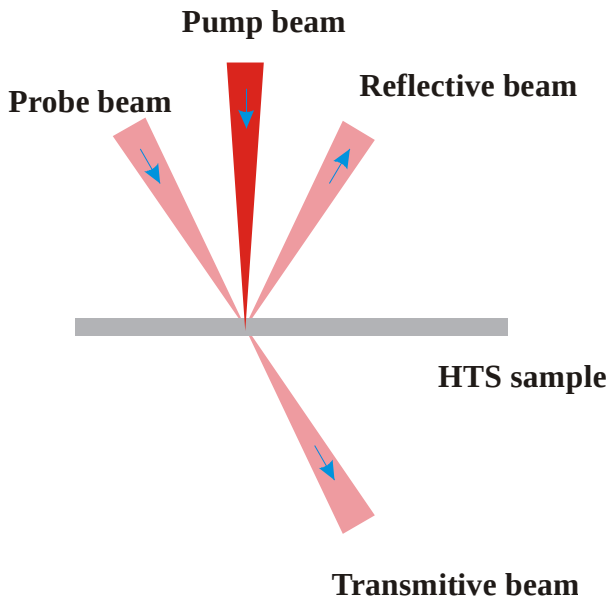

Figure 4-31 A schematic of the *all-optic* pump-probe technique.

One sampling technique is the so-called *all-optic* pump-probe method [108-110], as depicted in Figure 4-31. In this method, the pump laser generates a fast optical response. This optical response induces a fast transient of the dielectric constant change at the pump point of the HTS film, which affects the reflectivity (or transmitivity) of the probe beam. By measuring the reflectivity (or transmittivity) with respect to time delay, such dielectric constant transient can be captured. One disadvantage of this method is the difficulty in data interpretation. Since what people are interested is the Cooper pair breaking with laser illumination; however what the experiment probes is the dielectric constant change of the HTS film. And there is no direct bridge connecting these two parameters.

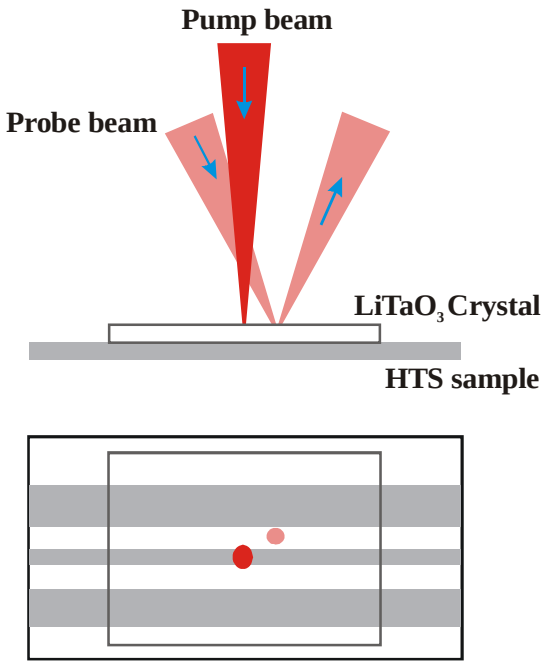

Figure 4-32 A schematic of the *E-O* sampling.

Electro-optical (*E-O*) sampling [111] is another optical sampling method, as shown in Figure 4-32. In this method, a fast optical response voltage transient generated by a pump laser pulse is converted into an optical signal through the linear electro-optic or Pockels effect. The electric field associated with the optical response transient perturbs the dielectric constant of the *EO* crystal, and consequently the polarization of the probe laser pulse changes. Since the Pockels effect is an ultrafast process, the time resolution of *E-O* sampling is only limited by the laser pulse duration, which is usually in the sub-picosecond region. *E-O* sampling is a good method of studying any ultrafast phenomena in any material. A 0.86 ps fast optical response signal has been attained for YBCO films [79].

The method we use for our experiment is the *electrical* correlation measurement. The idea of this method comes from the photoconductive sampling method which is

widely applied to the measurement of an ultrafast optical response of semiconductor materials [112, 113]. The essential feature of this method is that a semiconductor photoconductive switch is used as a sampling gate to probe the ultrafast optical response generated by another (pump) photoconductive switch, as shown in Figure 4-33. Basically a photoconductive switch is a gap on which the laser illuminates. If the two photoconductive switches are identical, the measurement is referred to as the auto-correlation of the ultrafast optical response. A straightforward question is whether or not this method can be applied to measure the fast optical response of HTS films? Specifically, can the superconductor material serve as a sampling gate? The answer is positive. We will show how to achieve it in the following. We first examine the fundamental difference between a superconductor and a semiconductor. Without laser illumination, a superconductor in its superconducting state is a perfect conductor with zero resistance, while a semiconductor is an insulator. With laser illumination, a superconductor is in a high-impedance state, while a semiconductor is in a conductive state. In this sense, a superconductor is referred to as an opening switch and a semiconductor is regarded as a closing switch. Based on the above facts, a semiconductor switch is made of a gap and a superconductor switch is made of any point in a superconductor line, as described in Chapter 2. To implement the *electrical* correlation measurement of the fast optical response of the HTS film, we propose a novel T-shape coplanar waveguide device. In our experiment, a superconductor switch is used as a sampling gate to sample the fast optical response transient. This method is advantageous in that it is a direct measurement of the *electrical* optical response transient which is

directly related to the Cooper-pair breaking. The temporal resolution of this method is limited by the optical response transient itself.

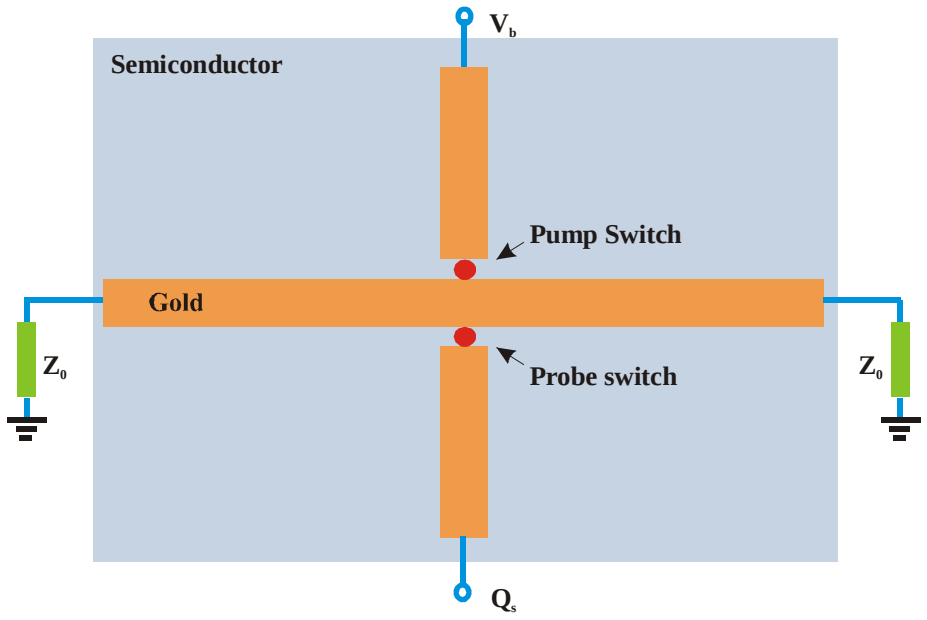

Figure 4-33 A schematic of the photoconductive sampling configuration.

4.4.2 Theory and Experimental Arrangement

The schematics of the experimental setup and a T-shape HTS device employed in our study are shown in Figure 4-34 (a) and (b) respectively. Two laser pulses derived from the same laser pulse illuminate the sample at two spots, a pump spot and a probe spot, with a time delay τ. The *dc* current is shorted through the '|' part (we call it *bridge* hereafter) of the 'T' shape so that only the pump switch, which can be any point on the bridge, is biased. The pump switch is illuminated by a small amount of laser energy so that only a non-equilibrium fast optical response (we call it pump electrical transient hereafter) is generated. This transient travels along the transmission line and reaches the probe switch. The principle of using superconductor switch as a probing switch is based

on the gating technique. In such gating process the probe superconductor switch is illuminated by a laser pulse with relatively high energy. Thus the thermal effect dominates and the superconductor switch acts as an opening switch. Without the laser illumination on the probe switch, the pump electrical transient will transmit through probe switch with no impedance. However, if the pump electrical transient arrives at the probe switch immediately after the illumination of the probe switch, it will be readily blocked at the probe spot. This is due to the fact that with pulsed laser illumination the impedance of the probe switch will be increased due to the Cooper pair breaking, leading to the opening of the probe switch. This opening process is the basis of the gating process and can be described by a step-like function. The rise time of this gating function, which is determined by the cooper-pair breaking time, should be on the same order as the electrical pump transient under test. While the gating time, which is determined by the thermal effect, can sustain hundreds of picoseconds to nanoseconds. This duration is sufficient to cover the whole range of the pump electrical transient (on the order of picoseconds). A sampling oscilloscope is used to monitor the output voltage signal. Figure 4-35 shows the output signal on the oscilloscope for two cases. One is when the pump electrical transient is not blocked at the probe spot, while the other is for the blocked electrical transient. In these two cases the pulse-width measured from the oscilloscope does not change due to the time integration effect of the oscilloscope. In other words, if the pulse-width of an electric pulse is shorter than the time resolution of the oscilloscope, it will be stretched. Therefore the peak value of the output signal is proportional to the time integral of the pump electrical transient modulated by the step-

like gating function. And the amplitude of the output signal on the oscilloscope varies as a function of τ.

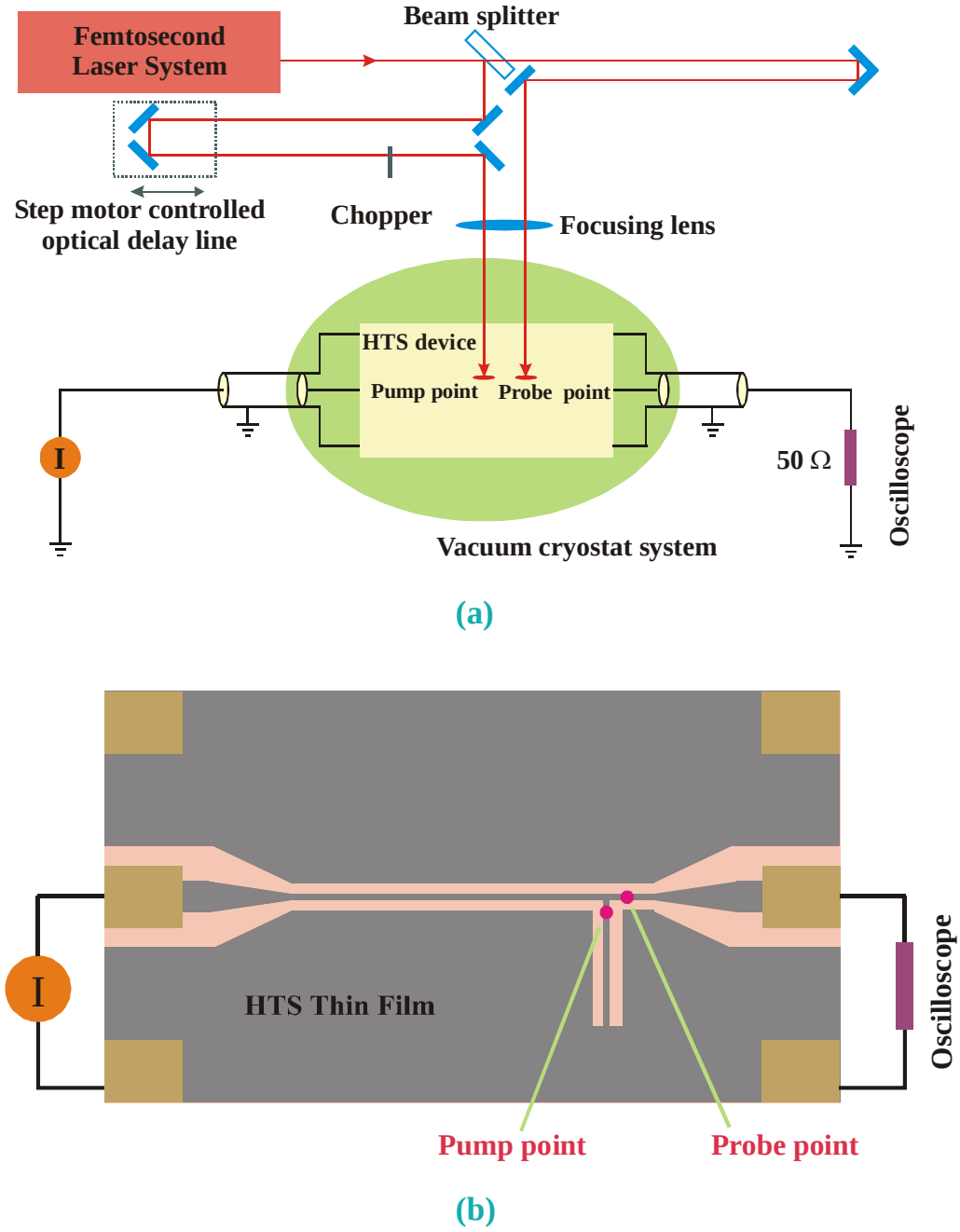

Figure 4-34 (a) The experimental setup for the electrical correlation measurement of the fast optical response of HTS film. (b) The applied HTS device.

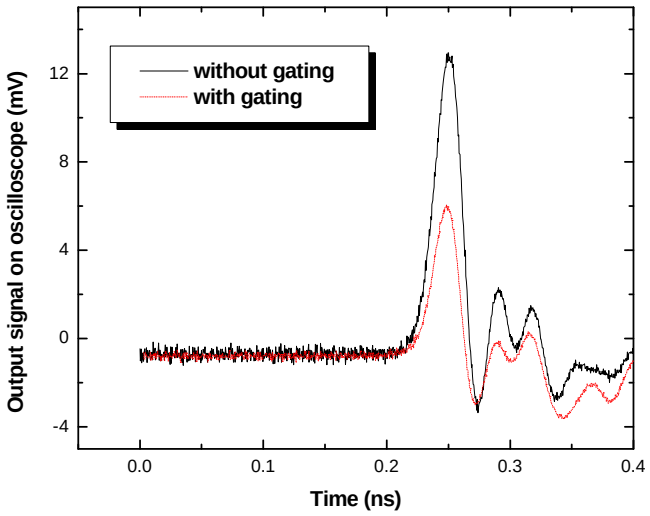

Figure 4-35 Output signal on the oscilloscope for two cases. Pump electrical transient is (not) blocked at the probe spot.

Let V represent the amplitude of the output signal on the oscilloscope, $V(\tau)$ can be expressed as

$$V(\tau) = \int_{-\infty}^{+\infty} dtE(t)g(t+\tau), \tag{4.27}$$

where $E(t)$ is the pump electrical transient generated by the pump superconductor switch, $g(t)$ is the step-like gating function describing the opening process of the probe superconductor switch, and τ is the time delay including the optical delay as well as the electrical delay of pump electrical transient propagating from the pump spot to the probe spot. In the ideal case where $g(t)$ is a perfect step function,

$$\frac{d}{d\tau}V(\tau) = \int_{-\infty}^{+\infty} dtE(t)g'(t+\tau) = \int_{-\infty}^{+\infty} dtE(t)\delta(t+\tau) = E(\tau). \tag{4.28}$$

This implies that the derivative of $V(\tau)$ with respect to τ represents the pump electrical transient, or the fast optical response, of the superconductor film – which is just what we are attempting to measure. However, in reality $g(t)$ is never a perfect step function, instead, it is a step-like function with a finite rise-time. According to the above equation the derivative of $V(\tau)$ represents the correlation of $E(t)$ and $g'(t)$, where $g'(t)$ is the derivative of $g(t)$. It is a reasonable assumption that the pulse-widths of $g'(t)$ and $E(t)$ are on the same order because the rise time of $g(t)$, which is determined by the Cooper-pair breaking time, is on the same order as $E(t)$. Therefore, we conclude that $\frac{d}{d\tau}V(\tau)$ represents the autocorrelation of $E(t)$. For an autocorrelation measurement, the pulse-width of the correlation signal can be directly related to that of the real signal given that the pulse shape is known. For example, for a Gaussian pulse, the ratio of its own pulse-width to that of its autocorrelation is 1:1.6. Assuming that the optical response signal in superconductor films is Gauassian like, the pulse-width of the fast optical response $E(t)$ can be estimated using the pulse-width of the measured autocorrelation signal.

4.4.3 Experimental Results

The YBCO film with 100 nm thickness is prepared by PLD on a $LaAlO_3$ substrate. The superconducting transition temperature of the film is 88 K. The film is patterned into the T-shape CPW device using the standard photolithography. A 30 μm center line and a 60 μm slot line are designed to obtain a 50 Ω characteristic impedance. The *bridge* length is ≅ 2.6 mm. The Ti-sapphire regenerative amplifier laser system provides laser pulses with ~100 fs pulse-width and 10 kHz repetition rate. The temperature of the YBCO device is kept constant at 78 K. The bias current is 3 mA. A

sampling oscilloscope with a 20 GHz bandwidth is utilized to monitor the output signal. The oscilloscope is also used to monitor the optical responses of both the superconductor pump switch and probe switch, to assure that the pump switch works in the non-equilibrium regime and that the probe switch works in the thermal regime. The average laser power is 2 mW for the pump switch, and 10 mW for the probe switch.

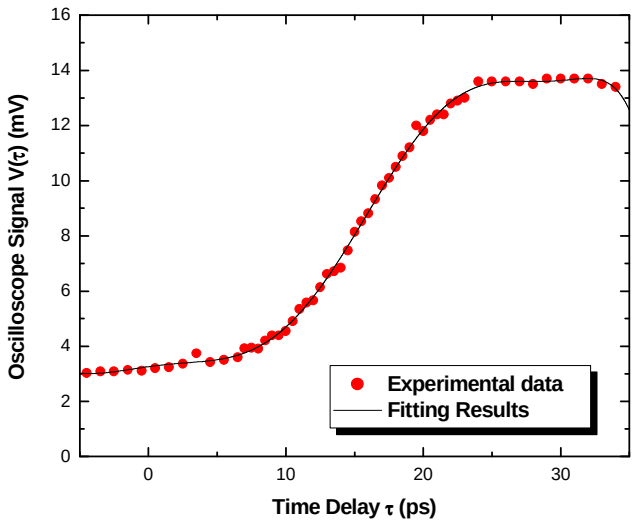

Figure 4-36 Experimental and fitted V as a function of τ.

Figure 4-36 shows the output signal V as a function of τ. The dotted line represents the experimental results while the solid line is the fitting curve. In order to take the derivative of $V(\tau)$, we fit the experimental data and convert the discrete points into a continuous function. Figure 4-37 shows the derivative of $V(\tau)$ with respect to τ, $V'(\tau)$. The FWHM of this $V'(\tau)$ pulse is 12 ps. As discussed in section 4.4.2, we estimate the pulse-width of the fast optical response to be 12/1.6 = 8 ps given the Gaussian shape assumption.

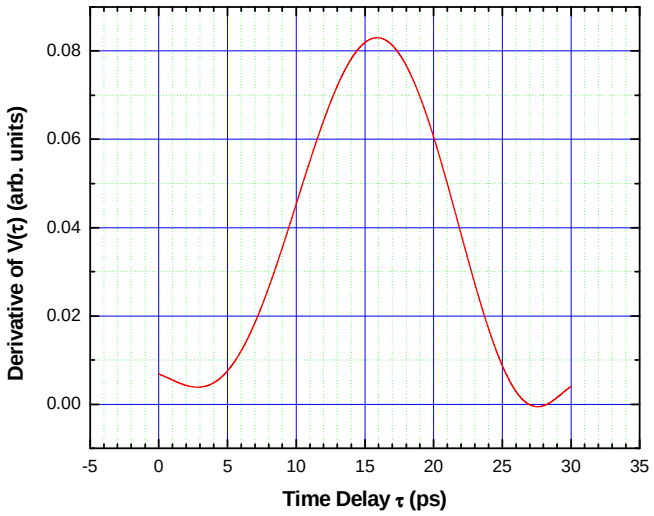

Figure 4-37 Derivative of $V(\tau)$ with respect to τ.

Compared with the 0.86 ps fast optical response measured by the *E-O* sampling [79], 8 ps is considerably larger. Possible reasons are: (1) The pulse-width of the optical response is broadened during propagating from the pump spot to the probe spot due to the dispersion and attenuation of the transmission line. In our experiment, this distance is several millimeters. (2) The focusing spots of both the pump and probe laser beams are finite. Consequently the pulse-width of the experimentally obtained optical response is larger than that of the intrinsic one. (3) The rise-time of the step-like thermal signal is slower than that of the kinetic inductance based fast optical response. The former could be slow down due to the higher power illumination. Nevertheless, the real pulse-width of the fast optical response must be less than 8 ps.

4.4.4 A Potential Application of the Superconductor Sampling switch

An ultrafast optical sampling technique can be used to measure the essential electronic parameters such as dispersion and attenuation of electrical devices (for

example, ultra-high-speed circuit). S. L. Huang *et al.* used an optical on-wafer semiconductor photoconductive switch to characterize the ultra-high speed circuit [114]. Correspondingly, the superconductor sampling switch can also be utilized for this purpose.

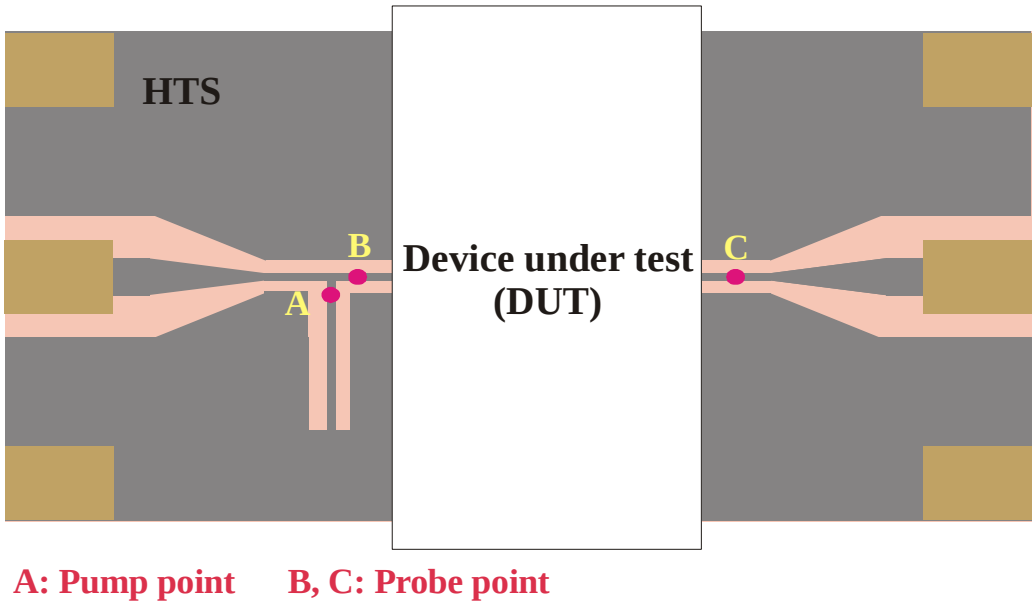

Figure 4-38 A proposed schematic of the optical sampling of integrated electrical devices with superconductor sampling switches.

Figure 4-38 shows the proposed schematic setup for optically sampling monolithic integrated electrical devices with the application of superconductor switches. The superconductor pump switch at position *A* generates an ultrafast broadband electrical pulse, which is the input pulse to the DUT (device under test). To measure this input pulse, we use a sampling switch at position *B*, as described in section 4.4. The input broadband electrical pulse propagates on the transmission line to the DUT. It suffers dispersion and loss during traveling in the DUT and will be broadened within the DUT. This broadened output electrical pulse from the device can then be sampled by another

superconductor sampling switch at position *C*. If we use $p(\tau)$ and $q(\tau)$ to represent the derivatives of the correlation waveforms of the input pulse and the output pulse respectively, we obtain S_{21} of the DUT,

$$S_{21} = \frac{F\{p(\tau)\}}{F\{q(\tau)\}}, \tag{4.29}$$

where $F\{\ \}$ represents the Fourier transform of a function.

In summary, similar to semiconductor photoconductive switches, potentially superconductor sampling switches can also be used as a sampling tool to characterize ultrafast monolithic integrated circuits.

4.5 Application of a Superconductor Opening Switch to a Current Charged Transmission Line (CCTL) System

In this section, we discuss the application of a superconductor opening switch and a superconductor transmission line to a current charged transmission line (CCTL) system to generate voltage pulses with a controllable pulse-width.

A CCTL system consists of a current source, an opening switch, a piece of shorted transmission line (TL), and the load (usually a sampling oscilloscope with a 50 Ω input impedance), as shown in Figure 4-39. The function of this system is to generate a square pulse with a short rise time and controllable pulse-width. The application of the superconductor opening switch to the CCTL system requires the opening speed of the switch to be fast [115]. The faster the opening speed, the better the performance of the CCTL system. Based on this point, the semiconductor photoconductive switch and the

superconductor switch triggered by the laser pulse are good choices. Compared with a superconductor switch, a semiconductor switch [116] operates as an almost ideal closing switch, but does not perform well as an opening switch due to its finite on-resistance. However, a superconductor switch is perfect as an opening switch since its on-resistance is zero. From this point of view, a superconductor switch is better than a semiconductor switch as an opening switch. Being a good opening switch, the input laser power over the superconductor switch has to be sufficiently high so that a thermal optical response can be obtained. This thermal response can be represented by a step-like function with a fast rise-time and long tail. We use a YBCO opening switch in our experiment.

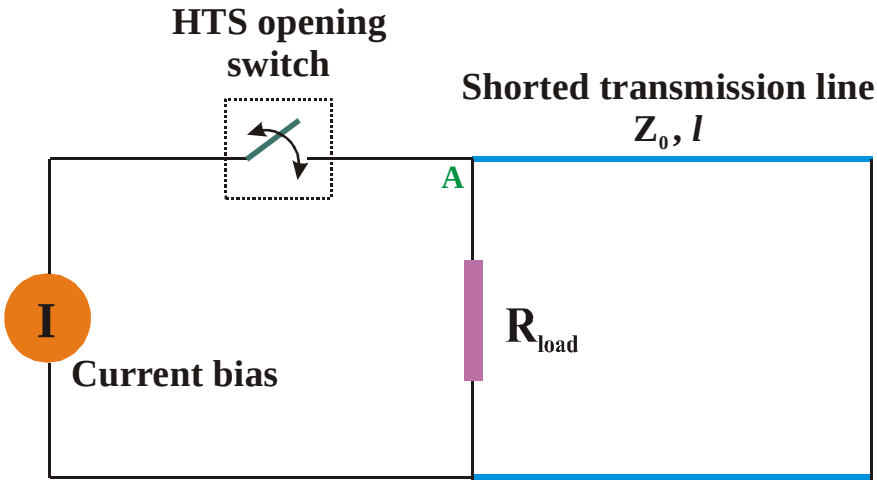

Figure 4-39 A schematic diagram of a CCTL system.

As a matter of fact, a CCTL system with a $Tl_2Ba_2CaCu_2O_8$ superconductor opening switch has already been realized. The CCTL has been applied in an inductive energy storage pulsed power system (IESPPS) to generate ultra-wide-band pulses [117, 118]. For this application, the shorted transmission line in the CCTL system must be as short as possible in order to give a high peak power gain, a short energy build-up time, and a compact size for the IESPPS [118]. Thus, if we can monolithically integrate a

CCTL into one single device we could make the transmission line at any length and at the same time avoid the contact and mismatch problems in the circuit. The inherent conductor nature of a superconductor with zero resistance in its superconducting state provides the possibility of achieving this goal. The device providing the basis of the monolithic CCTL system is the simple T-shape CPW device, as shown in Figure 4-40. The *bridge* of the 'T' (represented by *blue* color) is the shorted transmission line. Any point on the left '–' part of the 'T' (represented by *green* color) can be used as a superconductor opening switch.

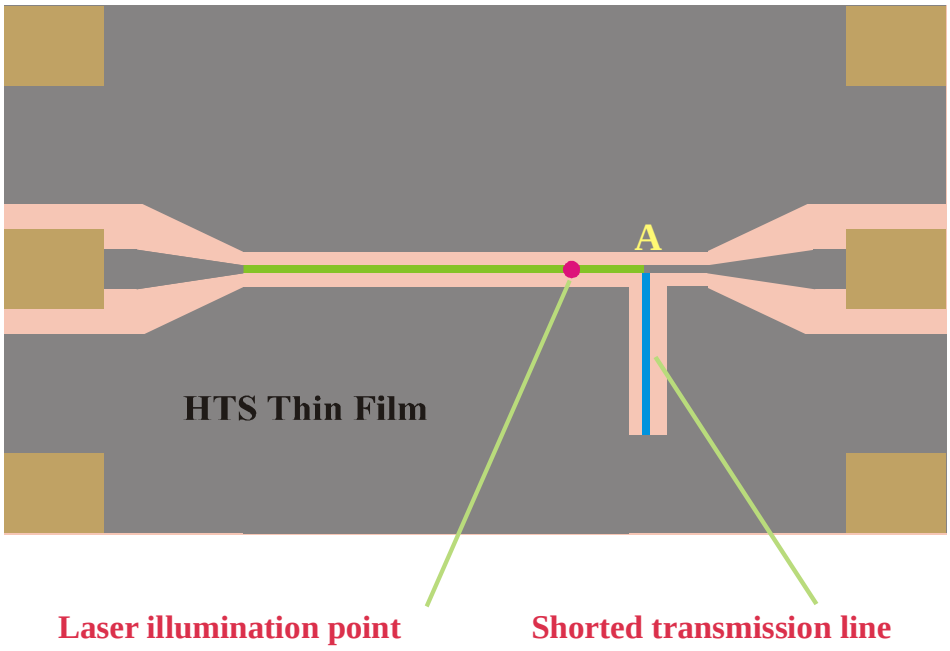

Figure 4-40 T-shape CPW device utilized as a monolithic CCTL system.

In order to explain the working principle of the CCTL system, we first examine what happens when a traveling wave, or a transient signal, meets a junction, or a discontinuity. Figure 4-41 (a) shows a junction which consists of two pieces of transmission lines. The characteristic impedance of each transmission line is Z_1 and Z_2

respectively. A traveling wave propagates along transmission line *1* and arrives at the junction. If $Z_1 = Z_2$, there will be no reflection at the junction. The input signal will pass through the junction and continue to propagate in transmission line *2*. However if $Z_1 \neq Z_2$, the reflection and transmission occur at the junction. The pulse reflection and transmission at a simple discontinuity can be described by equations

$$\begin{aligned} \rho_V &= \frac{Z_2 - Z_1}{Z_2 + Z_1} \\ \tau_V &= \frac{2Z_2}{Z_2 + Z_1} \end{aligned}, \qquad (4.30)$$

where ρ_V, τ_V represent the reflection and transmission coefficients of a voltage pulse. At the shorted end where $Z_2 = 0$, $\rho_V = -1$ and $\tau_V = 0$, suggesting a total reflection of the input signal. The analysis of a junction with three pieces of transmission lines, as shown in Figure 4-41 (b), is similar. The input signal propagates along transmission line *1* and reaches the junction. At the junction, part of the signal is reflected back to transmission line *1*, part of it transmits into transmission line *2*, and part of it transmits into transmission line *3*. Equation (4.30) still holds for calculating the reflection and transmission coefficients. Z_1 does not change, but Z_2 is replaced by $Z_2//Z_3$, denoted as $Z_{2\text{-}equivalent}$. If $Z_1 = Z_2 = Z_3 = 50\ \Omega$, then $Z_{2\text{-}equivalent}$ is 25; therefore $\rho_V = -1/3$; $\tau_V = 2/3$. Since transmission lines *2* and *3* are in parallel, the amplitudes of the transmission signal in transmission lines *2* and *3* are equal.

Let's come back to the CCTL system. Before laser illumination, the superconductor opening switch is in a closed (superconducting) state; and the *dc* current travels through the shorted superconductor transmission line to ground. Thus only the

green and *blue* parts of the superconductor transmission line are biased and charged. With laser illumination (the laser illumination point is illustrated in Figure 4-40), the superconductor opening switch is activated and a negative step-like thermal optical response signal is generated. This negative signal propagates along the transmission line and reaches junction *A* (refer to Figure 4-39 and Figure 4-40) at time $t = 0$. At junction *A* the input signal splits into two parts – one part travels along the shorted transmission line, the other part travels towards the load. We denote τ as the time required for a pulse traveling from junction *A* to the end of the shorted transmission line; or in other words, τ is the single-trip time for the shorted transmission line. For a pulse traveling along the shorted transmission line, it reaches the end at $t = \tau$ and is totally reflected back. Note that the polarity of the reflected pulse is reversed with respect to the incoming one. The reflected positive pulse travels back and hits junction *A* again. Similarly, the pulse experiences reflection and transmission at *A*. The reflected signal travels back to the end of the shorted transmission line, while the transmitted signal will split again into two parts: one to the current source, and the other to the load. Compared with the initial pulse traveling towards the load, the new signal to the load is delayed by a time 2τ. For the signal reflected back on the shorted transmission line, it will reach the shorted end and be reflected back to junction *A* again. This is the same as happened previously. Note that the amplitude of the reflected signal at junction *A* is one third of the original input signal. Eventually, the pulse on the load is a summation of all these voltage pulses, as illustrated in Figure 4-42. In this figure, a step function is used to represent the thermal optical response signal. With $Z_1 = Z_2 = Z_3 = 50\ \Omega$, which is the case for our device, a square-like signal can be obtained as shown in Figure 4-42. The duration of the output signal is 2τ,

which is determined by the length of the shorted transmission line. Another issue worth mentioning is that in order to generate a step-like pulse, the opening time of the superconductor switch has to be longer than 2τ.

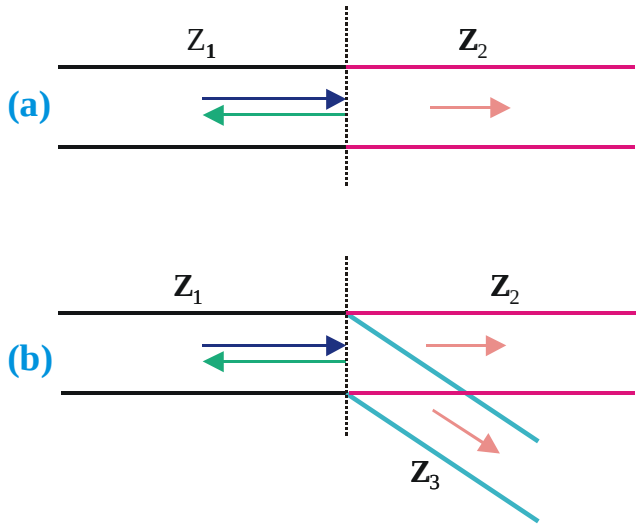

Figure 4-41 (a) A junction with two pieces of transmission lines. (b) A junction with three pieces of transmission lines.

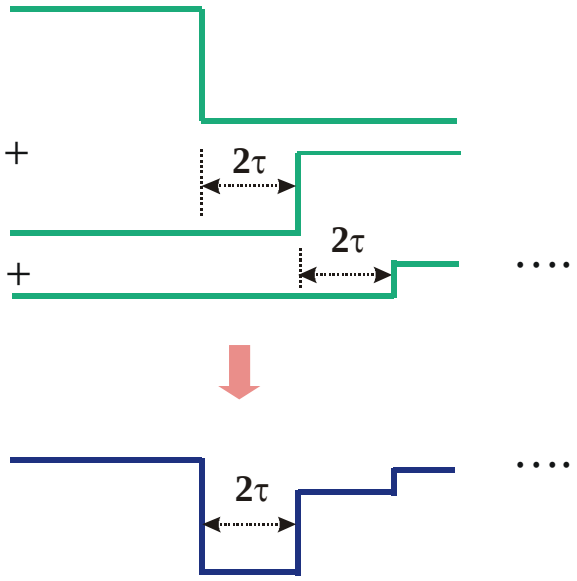

Figure 4-42 Illustration of the pulse forming in a CCTL system.

Figure 4-43 shows the experimental result. The bridge length of our device is ≅ 2.6 mm, corresponding to a pulse-width of ≅ 85 ps. This calculation is based on $\tau = nl/c$, where n is the refractive index of the $LaAlO_3$ substrate, l is the length of the shorted transmission line, and c is the speed of light in vacuum. The experimentally obtained pulse-width of ≅ 100 ps is close to the expected one. Also we note that the shape of the experimental obtained pulse is in good agreement with the one from the theoretical model (refer to Figure 4-42).

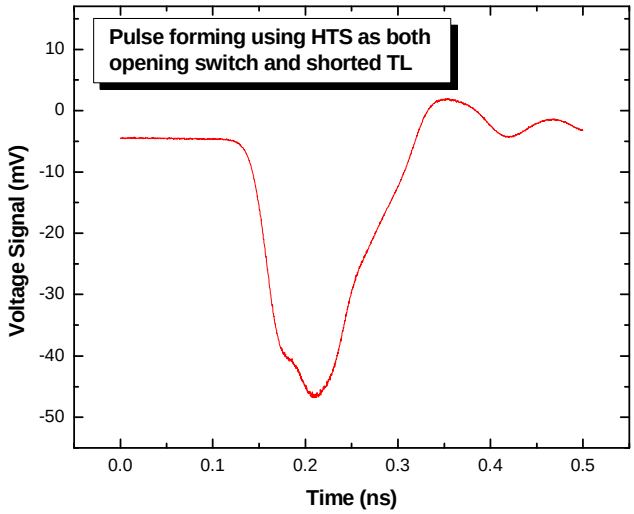

Figure 4-43 The short electrical pulse generated by a monolithic CCTL system.

In summary, we have designed and realized a monolithically integrated CCTL system that potentially could improve the performance of the IESPPS system for future applications.

Chapter 5 Conclusion and Future Work on the Study of the Optical Response of High Temperature Superconductor Materials

In this thesis, we systematically investigated the optical response of YBCO high temperature superconducting (HTS) films with femtosecond laser illumination. This study facilitates the future application of HTS materials to the ultrafast opto-electronic area.

The current, average laser power, and temperature dependence of the optical response of the YBCO films were explored with the improved TPR method whose advantages lie in its simple experimental setup, high signal-to-noise ratio, and unique ability to allow us to directly explore the microscopic mechanisms. All of the physical processes associated with the optical response and predicted by well acknowledged physical models were clearly observed with this method. Different waveforms under various conditions were characterized and shown to have good agreement with these physical models. The utilization of the laser pulse from a regenerative amplifier of a Ti:sapphire system enabled us to conduct a thorough study to gain significant insights into the optical response phenomenon. We briefly summarize the main results of our study in the following.

When laser power or substrate temperature is low, under which condition broken Cooper pairs constitute a neglectable fraction of the total number of the Cooper pairs in

the system, the waveform of the optical response exhibits a bi-polar nature that can be described by the non-equilibrium kinetic inductance model. According to the kinetic inductance model, the magnitude of the fast optical response signal is a direct measure of the Cooper pair breaking rate (dn_s/dt) with femtosecond laser pulse illumination. This kinetic inductance based non-equilibrium optical response is called the fast optical response, which is of great interest since it may shed light on understanding the basic mechanism of the high temperature superconductor material. The bi-polar signal gradually becomes a uni-polar one with a second peak appeared with increasing laser power. This process is described by the 2-T model, which depicts the interaction between the temperature of electron subsystem and that of the phonon subsystem. With sufficiently high temperature and laser power, the superconductor film is pushed to its resistive state; simultaneously electrons and phonons reach equilibrium and heat is relaxed through phonon diffusion out of the film. Consequently, a signal with a long tail is observed. This bolometric based optical response is called a thermal response or slow response, which is the key to an opening switch application. YBCO films with various film thicknesses were prepared and studied. The films can be divided into two groups – optically thin films and optically thick films depending on whether the film thickness is less or greater than the optical penetration depth. The waveforms of the optical responses of the films in same group demonstrate good consistency, while the waveforms of films belonging to different groups are different. The difference only lies in the thermal part of the signal, while signals related to the non-equilibrium process show resemblance. For optically thick films, a third peak, which is assumed to be associated with heat diffusion within the superconducting film, emerges. This assumption is validated by the observed

dependence of the position of the third peak on the film thickness. Considering applications of superconductor films, thin films can achieve higher efficiency and thus are preferred over thick films.

From our experimental data, we discovered that even if *P* or *T* is large, a bi-polar waveform emerges as long as the other parameter is sufficiently low. This suggests that the optical response process is only determined by the initial condition $\Delta n_{sc}/n_{sc}$ explicitly and is dependent on *P* and *T* implicitly through this initial condition.

The photon-energy dependence of the optical response, specifically, the Cooper pair breaking rate, was studied for a possible energy excitation around 1.5 eV, which may be important in understanding the formation of Cooper pairs in high temperature superconductors. A 1.5 eV resonance was observed with a total width of ≅100 meV. Three sub-features located at ≅ 1.63, 1.54 and 1.50 eV were observed with a width of ≅ 20-50 meV each. The experimental data can be well explained by stripe phase theory, which claims that the superconducting phase in the Cu-O plane in the high temperature superconductor is highly inhomogeneous with the insulating phase coexisting with the metallic conducting phase. The stripes are suggested to be highly dynamic and thus difficult to observe unless our 100 fs laser pulse is utilized. Based on the stripe phase scenario, the peak at 1.63 eV is identified as the charge transfer related exciton transition; the peat at 1.54 eV is associated with the excitation of the excitonic charge transfer and that of a LO phonon; and the peak at 1.50 eV originates from the combined effects of the excitonic charge transfer, a LO phonon, and a magnetic resonance. To verify the stripe phase theory, we also investigated the photon energy dependence of the fast optical response of oxygen depleted and Zn doped YBCO. The oxygen doping is in the Cu-O

chain while the Zn doping is in the Cu-O plane. The stripe phase theory is only concerned with the Cu-O plane. Therefore, we expected to observe no discrepancy between the photon energy dependence of the optical responses of oxygen doped and optimally doped YBCO. However, we should be able to observe the difference in the photon energy dependence of the optical responses of Zn doped YBCO from that of oxygen doped or optimally doped YBCO. The experimental results confirmed our conjectures.

The theoretical prediction of the speed of the non-equilibrium fast optical response is on the order of picoseconds, which is much less than the time resolution of a common electronic instrument. To temporally resolve this fast process, we performed a pump-probe *electrical* correlation measurement of the fast optical response transient with a T-shape coplanar waveguide device. The concept of a superconducting sampling gate (opening switch) was introduced. An estimated ≅ 8 ps pulse was obtained. The possible reasons that our result is considerably larger than the theoretical estimation include the dispersion of the fast optical response from the pump point to the probe point, the finite focusing spot of the laser beam, *etc*. In addition, an application of such a superconducting sampling gate was proposed for an on-wafer optical sampling.

A monolithic current charged transmission line system (CCTL) using the HTS opening switch and HTS transmission line was designed and realized to generate a rectangular pulse with a defined pulse-width. The principle of the CCTL system was presented in detail. The width of the output pulse is determined by the length of a shorted transmission line in the CCTL system. Due to the monolithic nature of our device, in which the shorted transmission can be designed to be as short as allowed, the generated

pulse-width could be very small. This is highly desirable for a CCTL system. In our system, the pulse-width is about 100 ps.

Future work can be carried out in three directions:

(1) To further prove the stripe phase theory, the photon-energy dependence experiment can be extended to the study of other high temperature superconductor materials and YBCO films doped with other elements. For example, besides YBCO, an electron-exciton excitation has also been proposed in $Tl_2Ba_2Ca_2Cu_3O_{10}$, $Tl_2Ba_2CaCu_2O_8$, and $(Bi,Pb)_2Sr_2Ca_2Cu_3O_{10}$, with energies between 1 and 2 eV based on thermal-difference reflectance spectroscopy. Therefore the sharp resonant features observed in the YBCO system with our femtosecond pair-breaking spectroscopy are also fully expected in these materials. YBCO with Fe, Al and Ni doping should also be studied. It has been shown that the doped Fe and Al atoms substitute Cu atoms in the Cu-O chain, while the doped Ni atoms replace Cu atoms in the Cu-O planes. Therefore, it will be very interesting to see how the three resonant sub-peaks look in these doped YBCO systems. Comparison of these data with previously obtained ones will be very helpful in understanding the mechanisms of high temperature superconductivity.

(2) Research can be conducted to realize the on-wafer optical sampling of a high-speed circuit with a superconducting sampling gate, as proposed in this thesis.

(3) From the application point of view, our monolithic CCTL system can be integrated into an inductive energy storage pulsed power system (IESPPS) to realize a monolithic IESPPS system. The consequent advantage is that the device will be smaller, the current buildup time will be shorter because of the smaller round trip time of the device, and the efficiency will be higher. Furthermore, since a HTS can also be patterned

into a planar antenna structure, integrating a HTS antenna with a monolithic IESPPS system (which can produce a high voltage pulse) will generate strong radiation in theory. New designs of a monolithic radiation system with a HTS opening switch, HTS transmission line, and HTS antenna should be implemented.

Chapter 6 Introduction to the Ultrafast Polarization Switching in Thin Film Ferroelectrics

Of relevance to the application of the ferroelectric materials as high-speed nonvolatile random access memories (FeRAMs) is the need to switch the remnant polarization state with a short electric pulse. The issue that how fast the polarization can be switched is of great concern. The goal of our research is to systematically study the ultrafast polarization switching dynamics of ferroelectric capacitors and obtain the intrinsic polarization switching time.

This chapter introduces the background information for the polarization switching process of ferroelectric materials. Specifically, we will explain the following questions. What is ferroelectricity? Why are ferroelectric materials good candidates for non-volatile memory devices and what is their historical development? What is the polarization switching process in the ferroelectric materials? Why and how do we study it?

6.1 Introduction to Ferroelectricity

In this section we introduce ferroelectric materials and their common properties.

In general, a ferroelectric material possesses the property that above a certain temperature, called Curie temperature T_c, it is in paraelectric phase; and below T_c, it is in ferroelectric phase. In the paraelectric phase, the dielectric constant falls off with temperature according to the Curie-Weiss Law

$$\varepsilon_r = B + \frac{C}{T - T_c}, \qquad (6.1)$$

where B and C are constants; and the direction of the polarization of each unit cell is random. Thus the net polarization of the material is zero in the absence of an applied electric field. However, in the ferroelectric phase, the material possesses non-zero net polarization even without an applied electric field and this polarization is reversible with the application of an electric field. This property is denoted as ferroelectricity. Actually, not all ferroelectric materials exhibit the phase transition characteristic. A good example is $BaMgF_4$, which does not experience phase transition even up to its melting point [119].

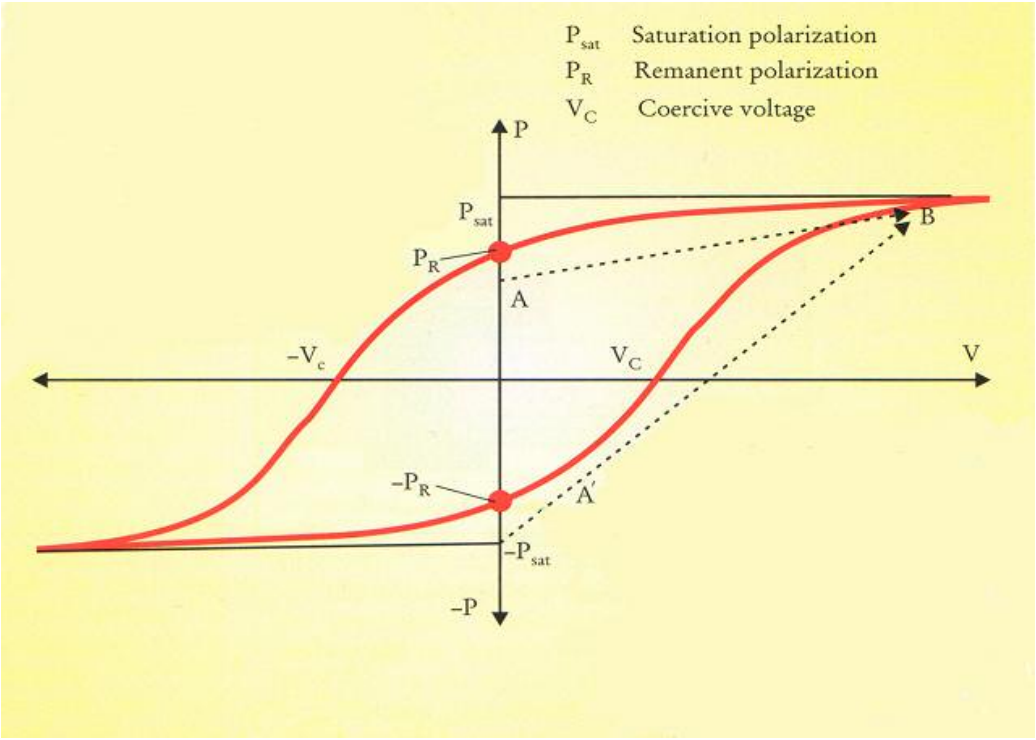

Figure 6-1 A schematic hysteresis loop of a ferroelectric material.

Different from linear dielectric materials, where the relationship between the polarization and the applied electric field is linear, ferroelectric materials in a

ferroelectric phase exhibit a non-linear, hysteresis loop property, as shown in Figure 6-1. The finite polarization in the absence of the electric field is called a remnant polarization or spontaneous polarization, denoted as P_s. E_c (V_c) is the coercive field (voltage) representing the minimum field (voltage) required to realize polarization switching.

The equilibrium properties of ferroelectrics can be well described by the so-called thermodynamic model. This theory stems from the Gibbs free energy and gives a macroscopic picture of ferroelectricity. The Gibbs free energy for ferroelectrics is expressed as [15]:

$$G = G_0 + \frac{1}{2}\beta(T - T_0)P^2 + \frac{1}{4}\gamma P^4 + \frac{1}{6}\delta P^6, \qquad (6.2)$$

where β, γ, and δ are constants. β and δ are found to be positive in all known ferroelectrics, while γ can be either positive or negative.

Figure 6-2 shows the characteristic curves of the Gibbs free energy (G) vs. polarization for ferroelectrics with a first-order transition in different temperature ranges. T_0, T_c, T_1, and T_2 are a series of special temperatures characterizing the transition from the ferroelectric phase to the paraelectric phase. We must note that the system can only be in the minimum energy state in equilibrium. At a low temperature where $T < T_0$, the G-curve has two stable minimum points corresponding to the two stable remnant polarizations, $+P_r$ and $-P_r$, and we say the material is in its ferroelectric phase. Note that only the ferroelectric phase can exist in this temperature range. From T_0 to T_c, the third minimum point corresponding to $P = 0$ appears in between the two previously existing minimum points. The fact that this new minimum point is less deep than the other two suggests that the ferroelectric phase is still the stable phase, while the non-polar

(corresponding to $P = 0$) phase is non-stable. With the increase in temperature, the third minimum point becomes deeper until $T = T_c$, where all of the three minimums are equal. T_c is the Curie temperature, as introduced earlier. When $T_c < T < T_1$, the third minimum is deeper than the other two, indicating that the ferroelectric phase is no longer stable, while the non-polar paraelectric phase is stable. Above T_1, the two ferroelectric minimums disappear. Therefore in this temperature range ferroelectric phase could not exist. For $T > T_2$, the G-curve becomes parabolic-like and only the paraelectric phase exists. Once T_0, β, γ and δ are given, T_c, T_1 and T_2 and the corresponding P_r can be calculated.

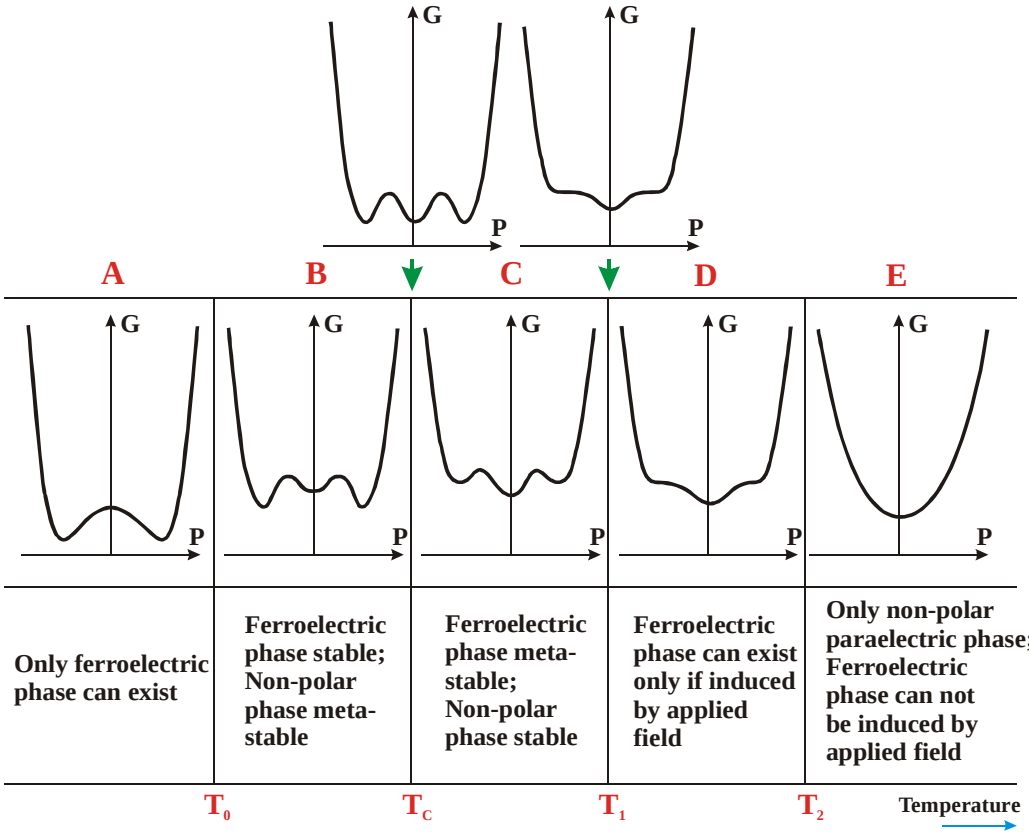

Figure 6-2 Characteristic Gibbs free energy (G) versus polarization curves for ferroelectrics with a first-order transition in different temperature ranges [15].

Ferroelectricity can only exist in non-centro-symmetric crystals due to the remnant polarization. Of the twenty-one non-centro-symmetric point groups, twenty exhibit piezoelectricity – where a polarization can be induced by stress or strain. Among these piezoelectric materials, ten are pyroelectric, where a temperature variation alters the electrical polarization. Ferroelectrics belong to this pyroelectric group. Obviously, only a small fraction of non-centro-symmetric crystals exhibit ferroelectric property. This is due to the fact that a readily polarizable axis is a prerequisite for a ferroelectric material.

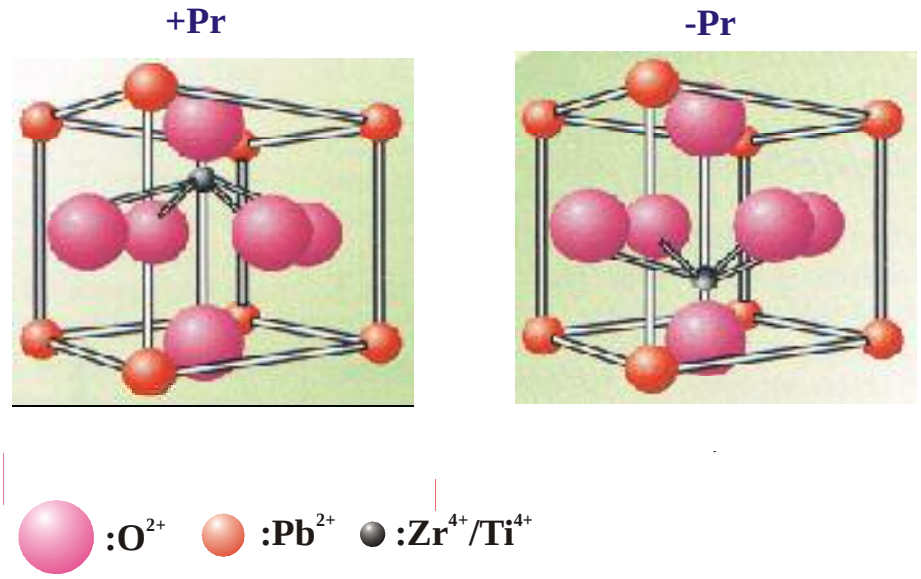

Figure 6-3 The cubic perovskite unit cell for Pb(Zr, Ti)$_3$ (PZT) [119].

When a ferroelectric material transforms from its paraelectric phase into the ferroelectric phase, the unit cell of the material varies correspondingly. For example, the commonly studied ferroelectric Pb(Zr,Ti)O_3 (PZT) has a body centered cubic structure in its paraelectric phase with Zr^{4+} or Ti^{4+} at the center of the cubic; however, in the ferroelectric phase the unit cell of PZT takes the non-symmetric structure with the Zr^{4+} or Ti^{4+} ion shifted up or down with respect to the oxygen octahedral, as illustrated in Figure

6-3. This displacement destroys the symmetry and causes a tetragonal distortion of the unit cell, leading to the two stable polarization states $+P_r$ and $-P_r$, which characterize the ferroelectric material.

The unit cell of different ferroelectric materials can be of great diversity. For example, it can be as simple as a cubic perovskite PZT, or as complex as a layered perovskite $SrBi_2Ta_2O_9$ (SBT), as shown in Figure 6-4.

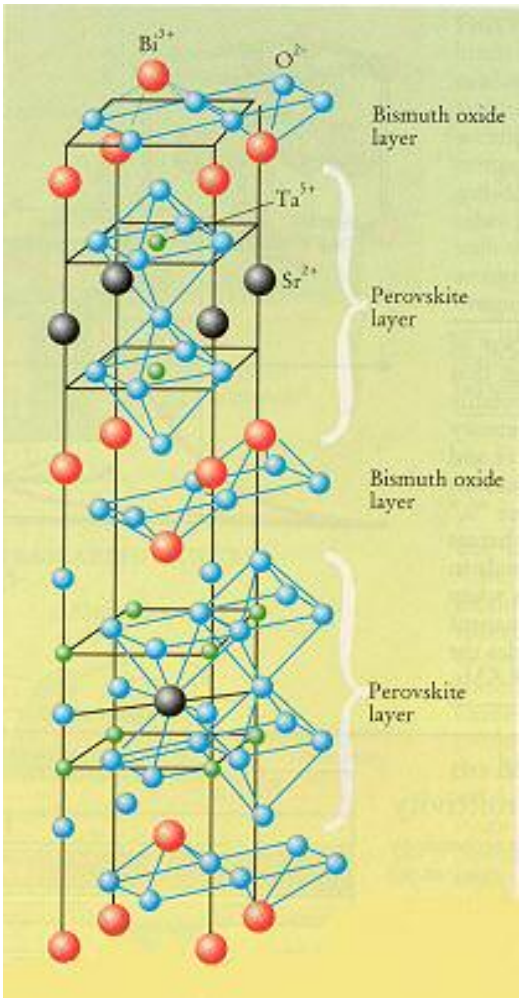

Figure 6-4 The layered perovskite unit cell for $SrBi_2Ta_2O_9$ (SBT) [119].

6.2 Application of Ferroelectric Thin Films to Non-volatile Memory Devices

6.2.1 Ferroelectrics as a Non-volatile Memory Device

The application of ferroelectric materials can be classified into two main groups. In one group, the piezoelectric and pyroelectric properties are exploited to produce MEMS devices such as micro-sensors, actuators, transducers, infrared detectors, electro-optic switches, and modulators [19]. The other application group is as memory devices, either dynamic random access memories (DRAMs) which utilize the high dielectric constant of the ferroelectric (typically between 300 to 1500), or ferroelectric non-volatile random accesses memories (FeRAMs) which take advantage of the hysteresis property of ferroelectrics in a ferroelectric state. In this thesis, we focus on FeRAMs applications.

The application of ferroelectric (FE) capacitors to FeRAMs is based on their two remnant polarization states and the capability of switching from one polarization state to the other by applying a short voltage pulse [120, 121]. The $+P_r$ and $-P_r$ polarizations can be used as logic '1' and '0' respectively. The word *non-volatile* indicates that the memory can preserve stored data information even when the power is off.

The basic *read* and *write* operations of the FeRAMs is explained with the help of Figure 6-5. In this figure, the positive polarization $+P_r$ and the negative polarization $-P_r$ are defined as logic '1' and logic '0' states respectively. State '1' can be written with a positive electric pulse. Since regardless of the previous polarization state, after a positive electric field greater than the coercive field is applied and then removed, the device will end up in the '1' state. Similarly, the '0' state can be written with a negative electric pulse. In the figure, $V_{write}(1)$ and $V_{write}(0)$ represent the amplitudes of electric pulses

completing the *write* operation. The electric pulse realizing the *read* operation, denoted by V_{read}, is always positive. Given the memory is in state '1', after applying a *read* pulse, the polarization changes from $+P_r$ to $+P_{max}$; only a linear non-switched response $P^{\wedge} = P_{\max} - P_r$ is measured in the form of a current flowing through the capacitor. If the memory is initially in state '0', then the polarization changes from $-P_r$ to P_{max}; thus a switched response $P^{*} = P_{\max} + P_r$ is obtained. P^{*} contains the domain polarization switching and is greater than $P^{\wedge}$. By comparing these responses (P^{*} and $P^{\wedge}$) with a reference signal, the initial state can be read. Cleary this reading scheme is a destructive one. Independent of its initial state, a memory cell is in '1' state after a *read* operation.

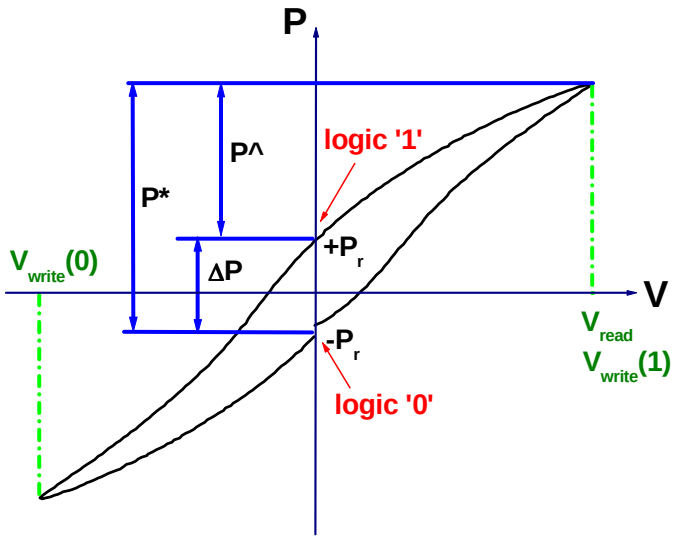

Figure 6-5 Basic read/write operation of FeRAMs.

Fatigue, retention, and imprint are the three main issues limiting the practical application of a FeRAM. Fatigue describes the endurance of a device, defined as a decrease of the switched polarization in a ferroelectric material with the increase of the

switching cycles. Retention reflects the aging of the device. A ferroelectric memory cell looses polarization slowly with time. If the polarization stored in a memory cell becomes so small or even reversed (the direction of the polarization changes) that can not be read correctly by a sensing circuit, we say the stored information is lost and refer to this situation as a '*loss of retention*'. Imprint is the tendency for ferroelectric memory cells to have a preferred state such that the switching speed from one state to the other is fast while the reverse switching is slow. In order to make the ferroelectric memory devices commercially available, all of these problems must be solved.

The most extensively studied ferroelectric materials for memory applications are SBT and PZT. Both of them have their advantages and disadvantages respectively. SBT does not exhibit fatigue with a Pt electrode but requires high processing temperature. On the contrary, PZT has a fatigue problem with a Pt electrode but can be processed at a relatively low temperature. Both materials can be made to have a low coercive field, which is essential for power saving in integrated high-density memory devices.

6.2.2 History of the Development of the FeRAM

Since the 1950s, tremendous efforts have been put into the study of memory devices using ferroelectrics. Advantages of these devices include: inherent non-volatile nature, low power consumption, radiation hardness, high speed, and high density [19]. Initially such memory devices were made of bulk materials or thick film. Thus the operation voltage was very high and devices were very expensive. The development of ferroelectrics in a thin-film form provides the possibility of producing fully integrated devices (integrated into silicon or gallium arsenide semiconductor chips) in which polarization switching can occur at less than 5.0 V applied voltage, which is the industrial

standard. The coercive field of a bulk ferroelectric ceramic is typically greater than 40 kV/cm [19]. Thus for a 200 nm thin film, the coercive voltage is only 0.8 V; however it is 80 V for a 3 mm thick bulk crystal. Furthermore, the development of the sol-gel technique and the 1T-1C cell architecture greatly facilitate the reliable fabrication of wafer-scale integrated ferroelectric memory devices.

To date, four important issues associated with the FeRAMs are under investigation. (1) The scaling issue. What is the smallest possible size for a ferroelectric memory device to exhibit ferroelectricity? How thin can a ferroelectric layer be to still yield a stable polarization? (2) The reliability issue. How can we solve the fatigue, retention and imprint problems of ferroelectric memory devices? (3) The quality related issue. How can the quality of ferroelectric films be improved? How can we make the remnant polarization larger? (4) The speed issue. What is the intrinsic polarization switching speed? What are the parameters limiting speed?

The first issue has been studied extensively towards the nanosize ferroelectric memory cell. A small memory device (or capacitor) size results in a high-density memory wafer. Questions of 'How to pattern and switch a nanosize ferroelectric capacitor?' and 'What are the effects of a reduced device size on material properties?' attract considerable attention. Ordered nanosize ferroelectric memory cells have been fabricated in different ways. With the electron-beam direct writing (EBDW) technique, ferroelectric memory cell arrays with a lateral length less than 100 nm of each single cell have been patterned. These cells show a good hysteresis loop [122]. An individual PZT ferroelectric capacitor of $\cong$ 70 nm lateral size was realized with the focused-ion-beam milling technique [123]. Nano-imprint lithography (NIL), which is a rapid, low-cost technique,

was applied to fabricate arrays of mesoscopic ferroelectric PZT cells with lateral lengths between less than 300 nm and several micrometers [124]. A technique called nature lithography or nanosphere lithography was utilized to prepare $BaTiO_3$ ferroelectric nano-structures, which have a pyramid-like shape with ≅ 200 nm lateral length at half of their height and form a regular hexagonal pattern. It has been shown that these nano-pyramids have the remnant polarization and are switchable by the electric field [125]. For non-ordered self-patterning cells, ferroelectric epitaxial nanocrystals with a 9 nm height and 50 nm lateral length were prepared [126]. As for the issue of critical thickness for ferroelectricity in ultra-thin films, a 4 nm thin film was demonstrated to have ferroelectricity experimentally [119]; theoretically, a 2.4 nm limit is proposed for a realistic $BaTiO_3$ thin film capacitor with $SrRuO_3$ electrodes [127].

Investigations of the fatigue problem are conducted from multiple aspects. (1) Is there any new ferroelectric material that shows superior fatigue resistances [128, 129]? (2) How can an electrode be engineered to prolong the lifetime of a memory device [130, 131]? For example, a PZT film with metal oxide electrode such as $(La,Sr)CoO_3$ (LSCO) shows a relatively long lifetime. (3) What is the origin of fatigue [132]? This question causes considerable debates. Oxygen vacancy in the ferroelectric film is one proposed reason, while blocked nano-domain is identified as another one [132]. It has also been shown that the domains become pinned with time and stop contributing to the switched charge when fatigue occurs in reality [19]. Recently, the mechanism of retention loss has been discussed and the internal field is found to be the main cause [133].

For a FeRAM, a large remnant polarization is highly desirable. Recent development on this issue is focused on increasing P_r [134-136]. A P_r of 90 μm/cm^2 was observed in a 100% polar-axis-oriented PZT film on a $SrRuO_3/SrTiO_3$ substrate [134].

The final issue is the polarization switching speed. Fast polarization switching is a desirable quality for FeRAMs. The most recent result is a ≅ 220 ps switching time obtained in this work for a $Pb(Nb_{0.4}Zr_{0.28}Ti_{0.68})O_3$ (PNZT) capacitor [137, 138].

6.3 Study of Polarization Switching Dynamics in Ferroelectrics

The study of the intrinsic polarization switching time of a ferroelectric material is important from both the physics and application points of view. For physics, it is a fundamental question. For applications, a faster polarization switching time leads to a faster *write* and *read* operation of a memory device. To study the polarization switching time problem, we have to understand the microscopic mechanisms of the polarization switching process.

Microscopically, a ferroelectric crystal consists of a large number of domains. A domain is defined as a group of dipoles that are polarized along the same direction. The study of the polarization switching process is equivalent to that of the domain switching process. Domains can be classified into two groups, *a*-domain and *c*-domain, depending on whether the polarization direction is perpendicular or parallel to the electric field. A 90° domain wall separates an *a*-domain and a *c*-domain; while a 180° domain is formed by two anti-parallel domains, as shown in Figure 6-6. It has been shown that it is the reversal of the 180° domains that dominates the polarization switching process.

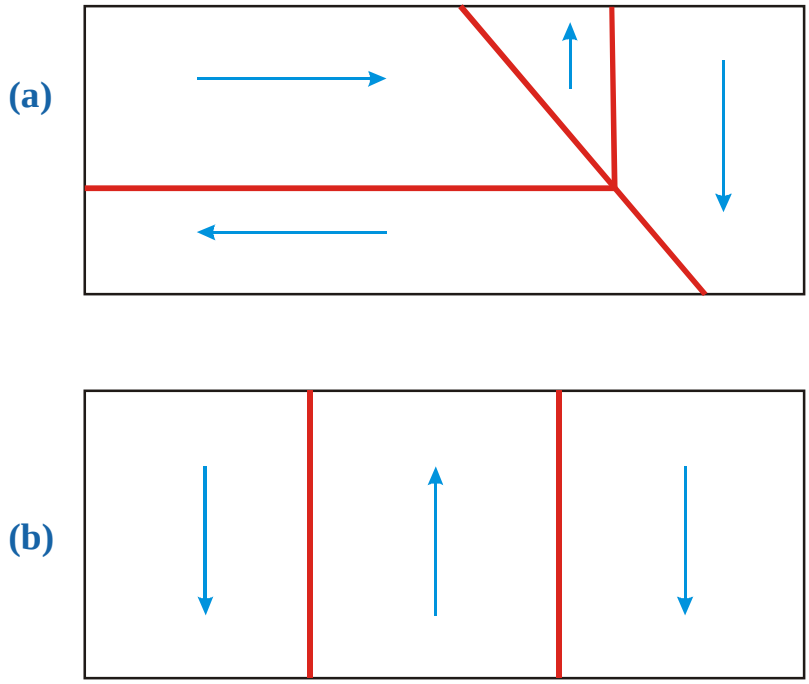

Figure 6-6 Illustration of (a) 90° and (b) 180° domain walls.

Much effort has been put into the exploration of the mechanisms of polarization switching in ferroelectrics. Basically there are two types of techniques that are applied [15]. One is the so-called pulse method, which monitors the displacement current flowing through the capacitor; the other is referred to as the optical method, which images the polarization of the device. The advantages of the pulse method are: (a) it is a direct measure of the polarization switching time; and (b) it is applicable to almost all kinds of ferroelectric materials. However, the relationship between the experimental results and the domain polarization switching is indirect. On the other hand, the optical method records the domain motion, and gives a clearer picture of polarization reversal in ferroelectrics. The disadvantages of this method include: (a) it has a complex experimental setup; and (b) it is difficult to realize the time resolution. The advantage of the optical method is the disadvantage of the pulse method, and vice versa. To investigate

the intrinsic polarization switching time, the pulse method is a perfect choice; and to explore the domain dynamics, the optical method is advantageous, while the only problem is that it might be extremely hard to observe the domain switching in a sub-nanosecond range.

In the early days, the optical method was very popular to study the movement of domain walls in the ferroelectrics. The experimental results [139-141] illustrated that domain switching is realized in a four-step process, (a) the nucleation of the reverse domain at ferroelectric/electrode interfaces, (b) the forward growth of the domains through the thickness of the crystal, (c) the sideway expansion of the domains, and (d) the coalescence of the domains, as illustrated in Figure 6-7.

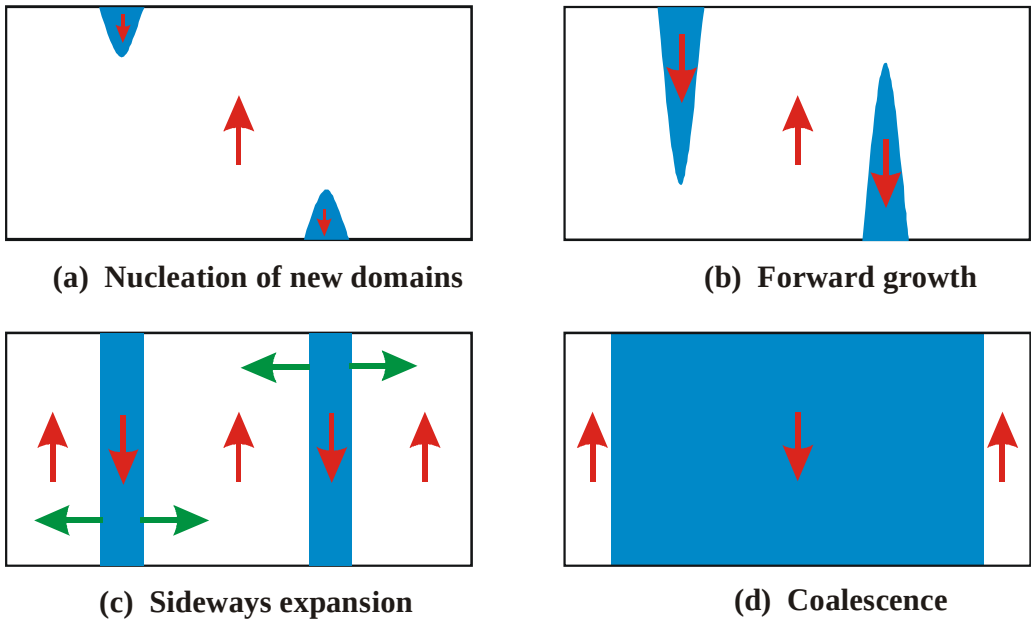

Figure 6-7 Illustration of the polarization switching process in ferroelectrics.

This model is regarded as the nucleation model for domain dynamics. The experimental results show that step-*a* and step-*c* are the rate limiting ones during the reversal, while step-*b* occurs very fast. However, a more recent study [142] gave

evidence that the forward domain growth is the rate-limiting step in the polarization switching of PZT thin-film capacitors. As a matter of fact, up to date, people still do not exactly know intrinsically how the domains are reversed – namely what the mechanism is, and what the limit is. Moreover, these experimental results did not exhibit a time-resolution reflecting the time scale by which the four-step domain reversal process can be completed, since it is difficult for the optical method to acquire data in real time. Consequently, how a domain reverses in ferroelectric thin-films on an ultrafast time scale, such as hundreds of picoseconds, is still an open question.

The study of the polarization switching process in ferroelectrics with the pulse method is focused on the polarization switching speed, or the intrinsic polarization switching time. With this method, P.K. Larson and coworkers reported a polarization switching time of ≅ 390 ps for PZT samples [20, 21]. We pushed this value down to ≅ 220 ps [jjli].

6.4 Motivation and Organization

As indicated in the previous sections, the speed of the polarization switching process is a fundamental issue. The goal of our research is to obtain the intrinsic polarization switching time. The pulse method, which will be described in detail in the subsequent chapters, is selected for this purpose.

It can be shown that in the pulse method the measurement of the polarization switching time is hindered by a variety of circuit related delays such as the rise-time of the input electric pulse, the timing jitter, and the *RC* time constant of the circuit. To obtain the intrinsic polarization switching time, the rise-time of the input electric pulse

and the RC_{FE} time constant must be at least on the same order as the intrinsic switching time. Experimentally, the rise-time of the input electrical pulse, which is the critical limiting factor of the pulse method, is of great concern. The faster the rise-time is, the higher the temporal resolution. The ideal input electric pulse for the experiment is a step-function pulse with an extremely fast rise-time and constant amplitude thereafter. Such an electric pulse is not readily attainable by electronic techniques. However the microwave photonic technique using a photoconductive switch actuated by an ultrashort laser pulse is perfectly suitable for producing such a pulse [112, 143]. In this thesis, we demonstrate the utilization of jitter-free, ultrafast rise-time electrical pulses generated by a semiconductor photoconductive switch with femtosecond laser illumination to study the fast polarization switching process in fully integrated ferroelectric $Pb(Nb,Zr,Ti)O_3$ capacitors. A polarization switching time t_s of $\cong$ 220 ps is obtained for a 4.5×5.4 μm^2 PNZT capacitor. Modeling of the switching transients using the Ishibashi-Merz model gives a characteristic switching time t_0 of $\cong$ 70 ps. The effects of the circuit parameters on the application of the Ishibashi-Merz model, which relates the experimental results of the pulse method to the domain polarization switching dynamics, are comprehensively examined. It is shown that the extracted characteristic polarization switching time t_0 and the domain growth dimensionality n are certainly circuit parameter dependent.

This part of the thesis is organized as follows. Chapter 7 covers the experiment in detail and the results. In this chapter, we first introduce the pulse method. By simulating the pulse method, the requirement to measure the intrinsic polarization switching speed is given. A detailed description of our experimental system follows. The subsequent section is devoted to the physical models for the dynamic properties of the polarization switching

process in ferroelectrics, which give a theoretical interpretation of the pulse method investigation. Experimental results are presented at the end of this chapter. We draw a conclusion and discuss future work in Chapter 8.

Chapter 7 Study of the Polarization Switching Dynamics of PNZT Ferroelectric Thin Film Capacitors

This chapter systematically studies the fast polarization switching process in fully integrated ferroelectric $Pb(Nb,Zr,Ti)O_3$ capacitors using a novel experimental setup that provides a time resolution of tens of picoseconds.

7.1 Pulse Method and Its Simulation

As discussed in Chapter 6, the pulse method is the most used one to study the polarization switching process in ferroelectric materials, since the polarization switching speed can be measured directly. In this section, we describe in detail the pulse method and present a numerical analysis of the measurement circuit.

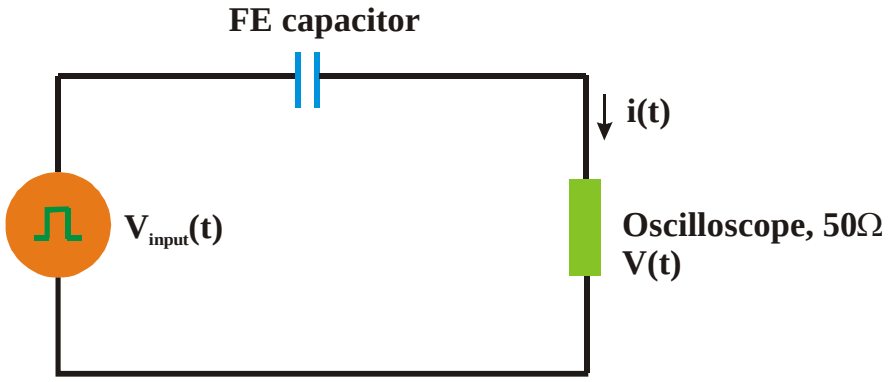

Figure 7-1 Equivalent circuit of the 'pulse method'.

The equivalent circuit of the pulse method is shown in Figure 7-1. It consists of a pulse generator, a ferroelectric capacitor under test, and a sampling oscilloscope with a

50 Ω input impedance. The pulse generator provides an input positive-positive or positive-negative pulse train, as shown in Figure 7-2, where the first pulse is the *write* pulse, and the second pulse is the *read* pulse. The pulses go through the ferroelectric capacitor and the oscilloscope is used to monitor the displacement current flowing through the capacitor. Figure 7-3 shows an expected output signal on the oscilloscope. With a positive-negative or positive-positive input, current transients corresponding to the polarization switched case (P^*) and the polarization non-switched case ($P^\wedge$) are observed respectively. By subtracting the $P^\wedge$ output from the P^* output, we obtain ΔP, which is only related to the domain switching and is of great interest.

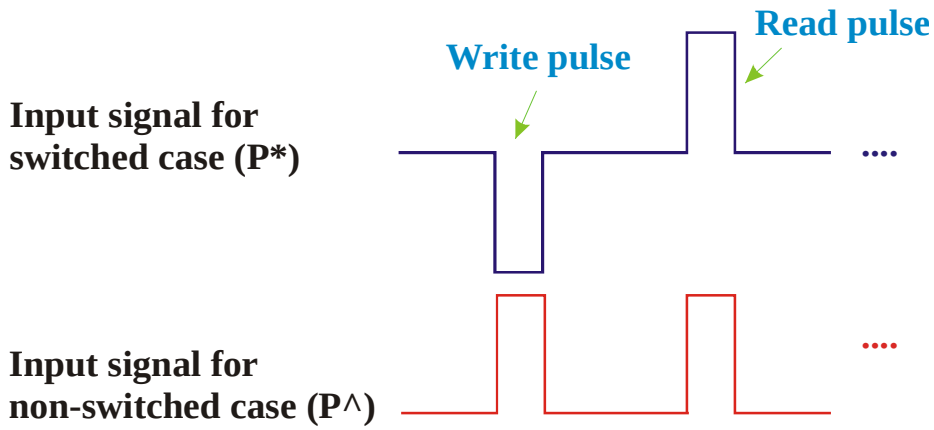

Figure 7-2 Illustration of the input positive-positive or positive-negative pulse trains of the pulse method.

In order to study the polarization process using the pulse method, we must first answer the following questions. What circuit parameters are critical for accurate measurement of the intrinsic polarization switching time? And how do they take effect? Considering the fact that the ferroelectric capacitor is also a circuit component, an understanding of the circuit performance makes it easy to answer the above questions.

This is the exact motivation for conducting circuit simulations of the pulse method, which will be presented in the following.

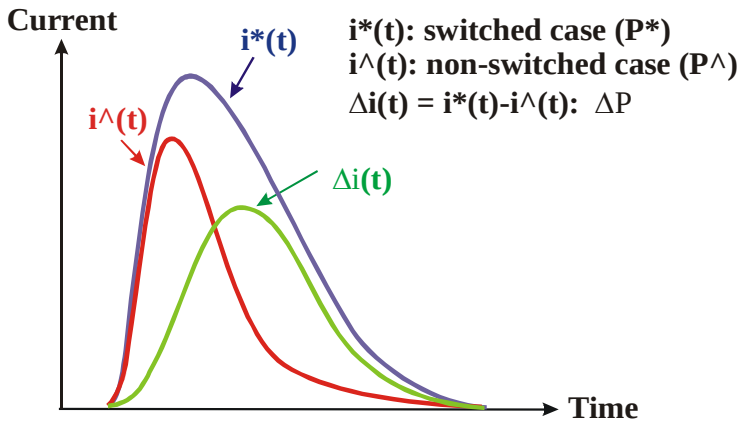

Figure 7-3 The expected current transients shown on the oscilloscope using the pulse method.

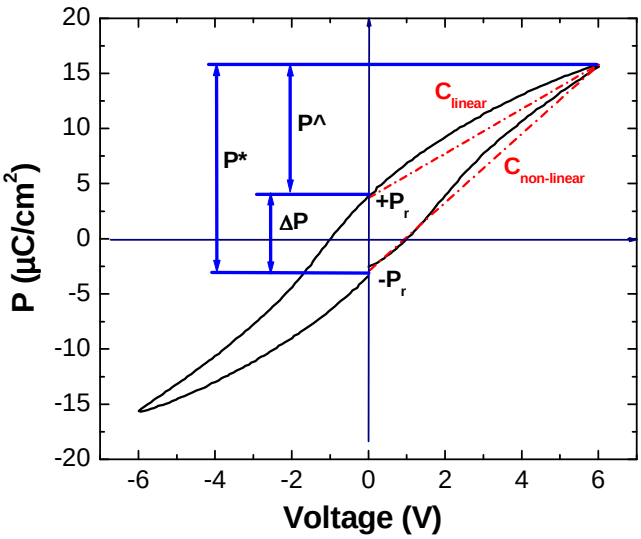

Figure 7-4 An experimentally obtained hysteresis loop of a thin-film PNZT capacitor. $P^{\wedge}$ and P^{*} correspond to the non-switched and switched polarization respectively.

Assuming that the capacitor is a linear dielectric one, the ordinary differential equation of the circuit is

$$i(t)R + \frac{\int_0^t i(t)dt}{C} = V_{input}(t), \tag{7.1}$$

where $i(t)$ is the current flowing through the oscilloscope and also the displacement current flowing through the capacitor. The oscilloscope is represented by a 50 Ω resistor R. C is the capacitance of the dielectric capacitor. $V_{input}(t)$ is the step-like input electric pulse to the capacitor. The displacement current $i(t)$ is directly related to $V(t)$, which is the output response displayed on the oscilloscope, or specifically the voltage drop across the 50 Ω node, by

$$i(t) = \frac{V(t)}{R}. \tag{7.2}$$

The voltage drop across the capacitor is given by

$$V_{cap}(t) = V_{input}(t) - V(t) = \frac{\int_0^t i(t)dt}{C}. \tag{7.3}$$

Equation (7.1) can be solved using a Laplace transform if $V_{input}(t)$ is an ideal step function. Realistically, the rise-time of $V_{input}(t)$ can never be zero. A numerical calculation is required to solve this equation. Simulations are carried out using the Runga-Kutta method. In simulations, the input step-like electric pulse ($V_{input}(t)$) is mathematically modeled as

$$V_{input}(t) = A * \exp[-\exp(-k(t - t_c)], \tag{7.4}$$

where A controls the amplitude, k controls the rise-time, and t_c controls the position. The selection of this model is based on the fact that our experimentally applied input electric pulse can be best fitted with this model.

Figure 7-4 illustrates an experimentally obtained hysteresis loop of a thin-film PNZT capacitor along with parameters of concern. The simulation of a non-linear ferroelectric capacitor is accomplished in the following way. From Figure 7-4, the polarization reversal process (P^*) consists of both the domain polarization switching process (ΔP) and the linear dielectric polarization variation process ($P^\wedge$), which is the charging or discharging of the capacitor. To simplify our analysis, the P^* process is modeled using a simple dielectric capacitor with capacitance $C_{non\text{-}linear}$,

$$C_{non-linear} = \frac{P^* \cdot A_{FE}}{V_{applied}}, \tag{7.5}$$

while the $P^\wedge$ process is modeled by another linear dielectric capacitor with capacitance C_{linear},

$$C_{linear} = \frac{P^\wedge \cdot A_{FE}}{V_{applied}}. \tag{7.6}$$

A_{FE} is the area of the capacitor. The values of P^* and $P^\wedge$ can be obtained directly from Figure 7-4. Giving $V_{input}(t)$, $C_{non\text{-}linear}$, and C_{linear}, voltage responses corresponding to the P^* and $P^\wedge$ processes, which are denoted by $V(t)_{P*}$ and $V(t)_{P\wedge}$ respectively, can be simulated. The $\Delta V(t)$ response, which corresponds only to the domain polarization switching ΔP process, is given by:

$$\Delta V(t) = V(t)_{P^*} - V(t)_{P^\wedge}. \qquad (7.7)$$

$\Delta V(t)$ is a very important quantity since it ultimately determines the polarization switching speed, dictating how fast a ferroelectric memory device can be. It may also provide information of the domain polarization switching dynamics with the help of certain theoretical model (*i.e.* the Ishibashi-Merz model, which will be introduced in detail in a later section).

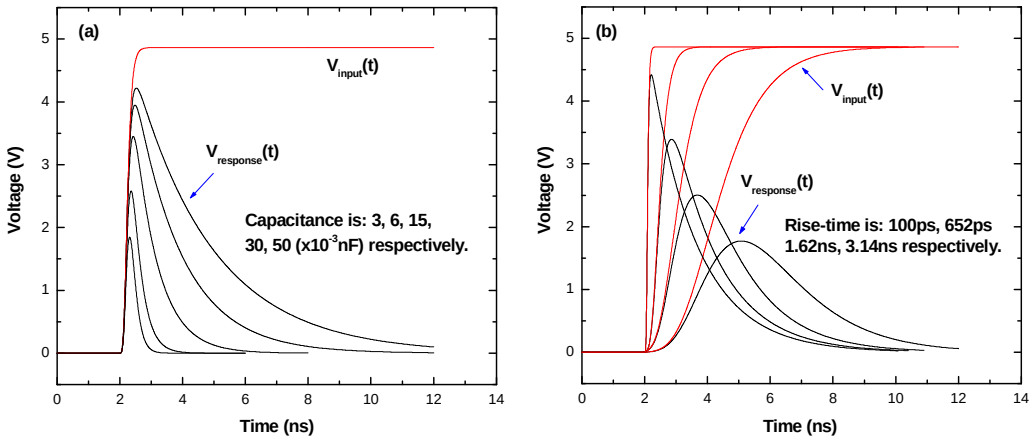

Figure 7-5 Simulated output responses $V(t)$ for various (a) capacitances and (b) rise-times of the input electric pulse $V_{input}(t)$. In (a), the rise-time of the input electric pulse is kept constant at 300 ps. In (b), the capacitance is kept constant at 3×10^{-2} nF.

The area of the capacitor and the rise-time of the input electric pulse are two parameters characterizing the measurement circuit. Therefore, simulations are carried out to study their effects on the polarization switching, specifically, on the output response $V(t)$. Figure 7-5 (a) and (b) show the output responses as a function of time for various capacitances and rise-times respectively. An output response with a longer tail is expected for a larger capacitance due to the increase of the circuit RC_{FE} time constant,

indicating the need for small-size capacitors to realize the measurement of the ultrafast polarization switching process. Similarly a slow rise-time of the input pulse results in a slow response. Even there does exist an ultra-fast polarization switching process, the slow rise-time makes it impossible to resolve this fast process that is embedded within. This is the exact reason why a step-like electric pulse with a fast rise-time is necessary. Figure 7-5 (a) and (b) also show that the shape of the output response changes with the capacitance and the rise-time. With an increase in the rise-time (keeping capacitance constant) or a decrease in the capacitance (keeping rise-time constant), the shape of the output response becomes more symmetric. It is important to understand this shape variation since it explicitly shows whether the RC_{FE} effect or the rise-time dominates under a given condition. As a matter of fact, it is the impedance ratio of the capacitor to the load resistor, denoted by

$$B = \left| \frac{1/j\omega C}{R} \right|, \tag{7.8}$$

that determines the shape of the output response. C is the capacitance, R is 50Ω, and ω is the angular frequency if the applied voltage is sinusoidal. From a circuit point of view, varying the capacitance or varying the rise-time has an identical effect on the shape of the output response. In our experiment the applied voltage is a step-like electric pulse with a finite rise-time. It is reasonable to use this rise-time information to derive an effective angular frequency $\omega_{effective}$. Here, we use 2π/(rise-time) to represent this $\omega_{effective}$. Hence, it is possible to roughly estimate the required rise-time of the input electric pulse for a capacitor with a specific capacitance. Faster rise-times are unnecessary for large-size capacitors.

In the following, simulations are carried out to investigate the rise-time dependence of the $\Delta V(t)$ response for a ferroelectric capacitor. A 22.5×25 μm^2 PNZT capacitor is chosen for this purpose. The corresponding P^*, $P^{\wedge}$, $C_{non\text{-}linear}$, and C_{linear} of this capacitor are 28.64 $\mu C/cm^2$, 16.01 $\mu C/cm^2$, 32 pF, and 17.9 pF respectively. Step-like input electric pulses with a 5V amplitude and various rise-times are applied in the simulation. Figure 7-6 shows the $\Delta V(t)$ responses for various rise-times of input electric pulses. Since $\Delta V(t)$ is obtained by subtracting $V(t)_{P^{\wedge}}$ from $V(t)_{P^*}$ (as defined in equation (7.7)), it is expected that faster rise-times lead to faster $\Delta V(t)$ responses. We earlier concluded from Figure 7-5 that the rise-time and the capacitor size could affect the shape of the output response $V(t)$. Consequently, they also affect the shape of $\Delta V(t)$.

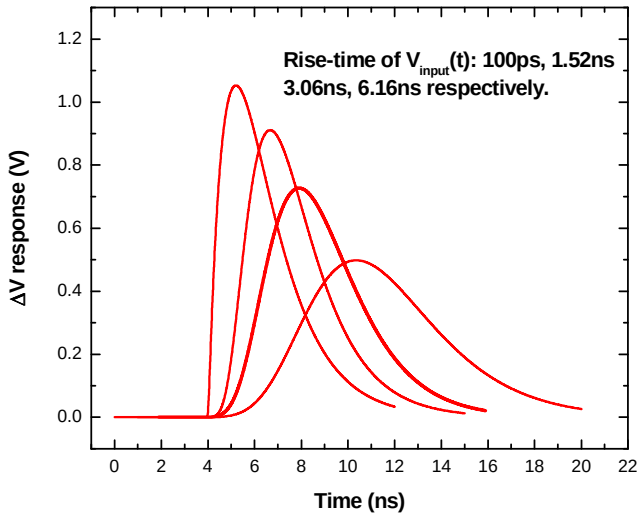

Figure 7-6 Simulated $\Delta V(t)$ responses for various rise-times of input electric pulses.

In summary, simulation results explicitly indicate that the fast rise-time of input electric pulses and the small size of ferroelectric capacitors are critical for the *accurate* detection of the fast polarization switching process.

7.2 Experimental Techniques

In this section we describe the device preparation and the experimental setup.

7.2.1 Thin Film Preparation with Sol-gel Technique

Due to the recent fast development of the application of ferroelectrics to memory devices, there arises a strong demand for the deposition of the ferroelectric perovskite thin-film materials that are compatible with integrated circuit technology. The common deposition techniques include: sputtering, sol-gel, pulsed laser deposition (PLD), metal-organic decomposition (MOD), chemical vapor deposition (CVD), and evaportation [19]. In our experiment, fully integrated $Pb(Nb_{0.04}Zr_{0.28}Ti_{0.68})O_3$ (PNZT) ferroelectric capacitors are prepared using the sol-gel technique. In the following, we introduce the basic knowledge of this technique.

The sol-gel deposition of PZT was invented by Yanovskaya *et al.* in Moscow in 1973 and by Hanold in U.S. in 1975 [19]. The sol-gel is one of the chemical processing techniques that is suitable for making ceramic or glass thin films. Much effort has been put to study how to obtain high quality ferroelectric thin-films using this technique [144]. A good review of the sol-gel deposition of PZT thin-films was given by Paz de Araujo [145]. Basically, a *sol* is a suspension or dispersion of discrete colloidal particles or polymeric species in a solution while a *gel* is a colloidal or polymeric solid that has an internal network structure with mixed or highly dispersed solid and fluid components [144]. Correspondingly, there are two types of sol-gel systems, colloidal and polymeric. In a colloidal *gel*, it is the electrolytic and steric effects in the precursor solution (or *sol*) that determine the *gel* formation. However in a polymeric *gel*, it is the rates and the extents of the chemical reactions that are important in forming the polymeric *gel*.

The *sol*-s that are used to deposit our PNZT films are titanium isopropoxide, Zirconium-n-butoxide, and lead acetate dissolved in stoichiometric proportion in hexane [146]. A sol-gel process is the one that involves the transition of a system from a liquid *sol* (mostly colloidal) into a solid *gel*. For the thin film deposition, the precursor solution is spin-coated onto the substrate to form an amorphous *gel*. The *gel* is then dried at 300°C for ≅ 30 minutes and then thermal-annealed slowly at 700°C for ≅ 1 hour to crystallize the ferroelectric film [146].

Ferroelectric thin films obtained by the sol-gel method are not single-crystal films, instead they are polycrystalline films where a large amount of grains exist in the films. A grain consists of many domains. The grain boundary can depolarize the film and make the remnant polarization of a polycrystalline ferroelectric thin film much smaller than that of a single-crystal thin film. Consequently the hysteresis loops of both kinds of films show different appearances. Unlike the hysteresis loop shown in Figure 7-4, which is for a PNZT polycrystalline film, the loop of a single-crystal film is more like a rectangle in that the polarization changes sharply around the coercive field; and the corresponding $P^{\wedge}$ is significantly smaller than P_r. Moreover, the P_r value of a polycrystalline film is considerably less than that of a single-crystal film.

The electrodes of our PNZT capacitor are made of $(La_{0.5}Sr_{0.5})CoO_3$ (LSCO) [147], with which the fatigue problem in PZT capacitors with Pt electrodes can be avoided. The reason for doping Nb^{5+} in place of (Zr^{4+}, Ti^{4+}) in a PZT thin film is to soften the PZT. This *soft* PZT exhibits a high dielectric loss, a low conductivity, and a low coercive field. The low coercive field of a ferroelectric material is one of the most desirable qualities for memory applications.

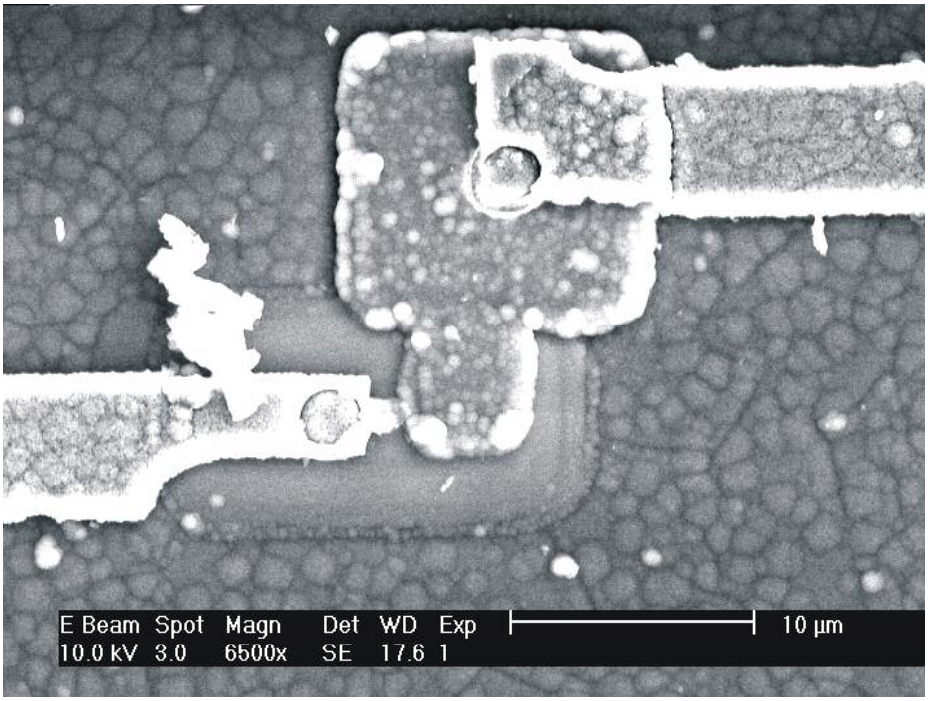

Figure 7-7 SEM image of a fully integrated PNZT ferroelectric capacitor made with the sol-gel technique.

Figure 7-7 shows the SEM image of a fully integrated PNZT capacitor made with the sol-gel technique. The ferroelectric film is sandwiched between the top and bottom electrodes of the device. A protection layer is coated on top of the top electrode to insulate the device from the air, which prolongs the lifetime of the device. Two wire-bonding pads are connected to the top and the bottom electrodes of the capacitor respectively. Differently from previous work, where the capacitor is put inside a lumped microwave circuit holder, our capacitor is inserted into 50 Ω micro-strip transmission lines, which are put on the surface of a copper block. Such a design avoids problems such as signal reflection and dispersion within the holder, and consequently a high-speed measurement is performed. Both wire-bonding pads are bonded to these outside transmission lines.

7.2.2 Experimental Setup

The ≅ 50 ps theoretically estimated polarization switching time [15-19] requires a setup with a time resolution of at least the same level. Since the rise-time of the input electric pulse is the bottleneck, generation of a step-like pulse with less than 50 ps rise-time is essential. In our experiment, a semiconductor photoconductive switch is used as a fast '*pulse generator*' to produce step-like pulses with rise-times as short as ≅ 50-100 ps and amplitudes up to 10 V.

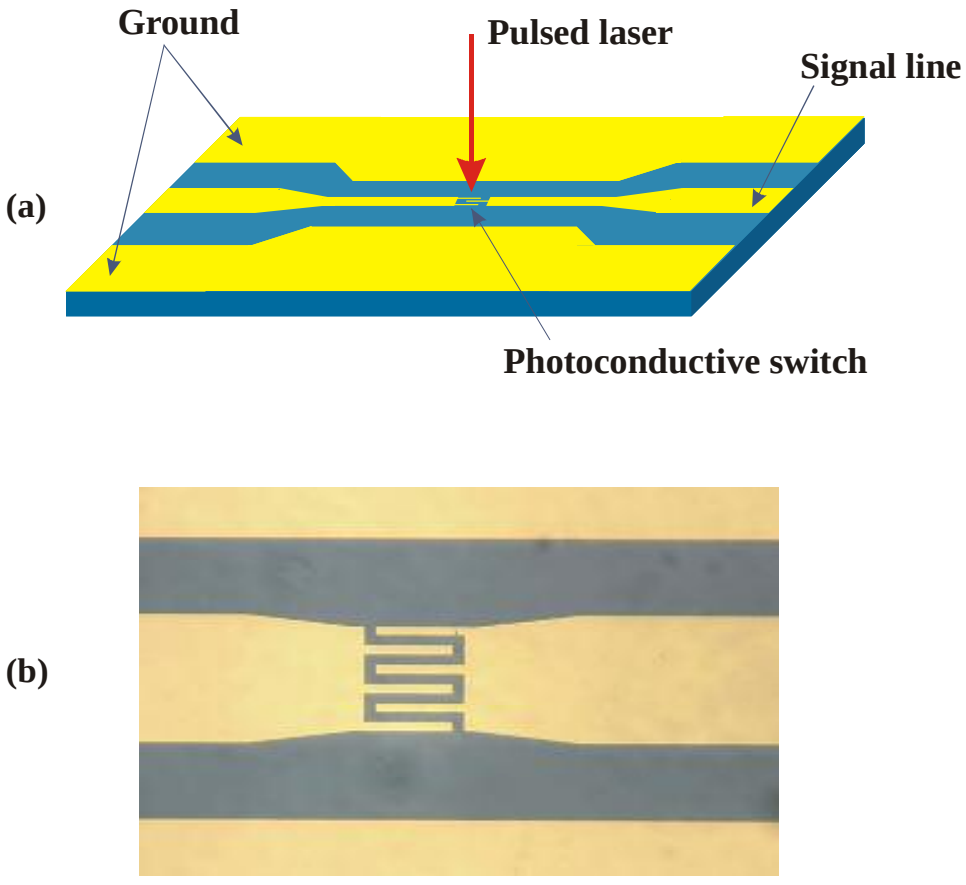

Figure 7-8 (a) Schematic and (b) real image of a semiconductor photoconductive switch device.

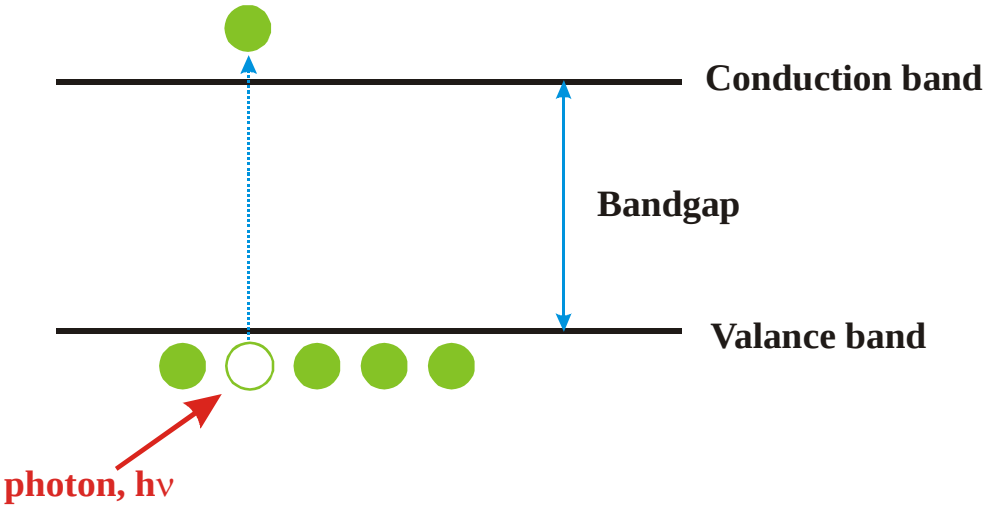

Figure 7-9 Principle of a semiconductor photoconductive switch.

Figure 7-8 (a) and (b) show a schematic and a real image of a semiconductor photoconductive switch device. Photoconductive switches with interdigitated fingers are patterned into the coplanar transmission line structure with a 50 Ω characteristic impedance in order to transmit the high-speed broadband signal with neglectable dispersion and attenuation. Figure 7-9 shows the principle of a semiconductor photoconductive switch. Without the pulsed laser illumination, the photoconductive switch is in the dark state, or high resistance state with a resistance of ≅ 100 kΩ to MΩ. With laser illumination, electron-hole pairs are generated and the switch is in the conductive state, with a resistance of possibly a few Ω. Consequently, a voltage pulse is produced. Theoretically the rise-time of this voltage pulse could be as small as picoseconds. However in practice it only reaches the sub-nanosecond region. The rise-time depends on laser power, bias, and *etc*. A Si photoconductive switch is chosen to generate the step-like pulse because carrier lifetime in Si is on the order of microseconds. The constant amplitude of the voltage pulse once turned on enables us to systematically

study the polarization switching process for ferroelectric capacitors of different sizes. One issue worth noting is the effects of the photoconductive switch dynamics on the final experimental results. Basically, the capacitance of a Si switch is sufficiently small (on the order of tens of fF) compared with that of the ferroelectric capacitor (on the order of tens of pF) under test; and what we are concerned with here is precisely the step-like electric pulse generated by such switch, which already includes the influence from the switch's time-varying capacitance and time-varying conductance; therefore in this sense the dynamics of the Si switch will not affect our experimental results.

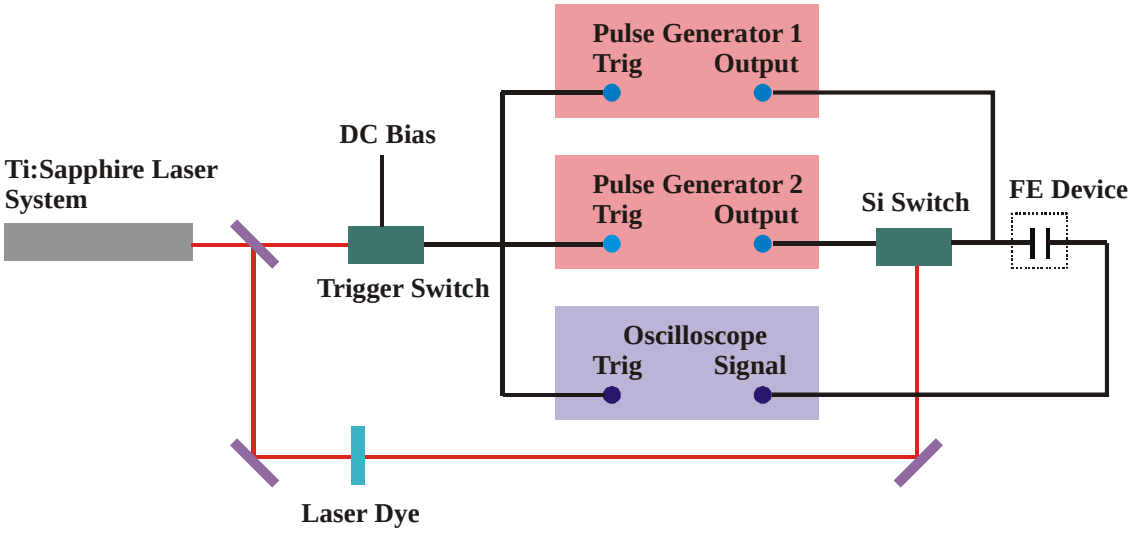

Figure 7-10 Experimental setup of the pulse method using a Si photoconductive switch as a fast pulse generator.

The detailed experimental setup is shown in Figure 7-10. A conventional pulse generator (pulse generator *1* in the figure) was used to produce the *write* pulse which sets the ferroelectric device to a stable positive or negative polarization state by applying a positive or negative square pulse. An electric pulse with a ≅ 7 ns rise-time, 8 V amplitude, and 1 ms duration was used as this *write* pulse. Femto-second laser pulses

from the Ti:sapphire regenerative amplifier (repetition rate = 10 kHz, laser pulse width ≅ 100 fs) illuminated the Si switch to produce *read* pulses with fast rise-time, sufficiently high amplitude and long duration. The bias of the Si switch was provided by another conventional pulse generator (pulse generator *2* in the figure). The delay between the two pulse generators was carefully tuned so that *write* pulses are in the middle of *read* pulses. The output pulse train to the ferroelectric device is the combination of the writing and reading pulse trains. The new pulse train can be a sequence of negative-positive pulses or positive-positive pulses. A negative-positive pulse sequence applied to the ferroelectric device produces a switched response $V(t)_{P*}$, while a positive-positive sequence gives the non-switched response $V(t)_{P\wedge}$. By subtracting the non-switched response from the switched response, the $\Delta V(t)$ response is obtained which gives information only depending on the domain polarization switching ΔP. An HP54750A sampling oscilloscope with a time resolution of ≅ 20 ps was used to monitor the output polarization switching response. The input impedance of the oscilloscope is 50Ω, which is impedance-matched to the transmission line to prevent the signal from reflecting back to the setup. Figure 7-11 shows the timing sequence of each pulse train. All instruments are synchronized by a low jitter trigger signal generated by a photo-diode trigger switch.

It is shown in Figure 7-10 that a dye solvent was inserted in the path of the laser beam towards the Si switch. Here the dye solvent is used as a saturable absorber to eliminate the pre-pulse of each laser pulse. For our ≅ 800 nm working wavelength of the laser, the dye material selected is *IR-140* from Exciton Inc. Its central absorption wavelength is 810 nm. The excited state lifetime is 600 ps. The corresponding solvent is

Ethylene Glycol / Propylene Carbonate (1:1). The density of the dye solvent is ≅ 0.38 mg/ml. The selection of the dye density depends on laser power and laser pulse-width.

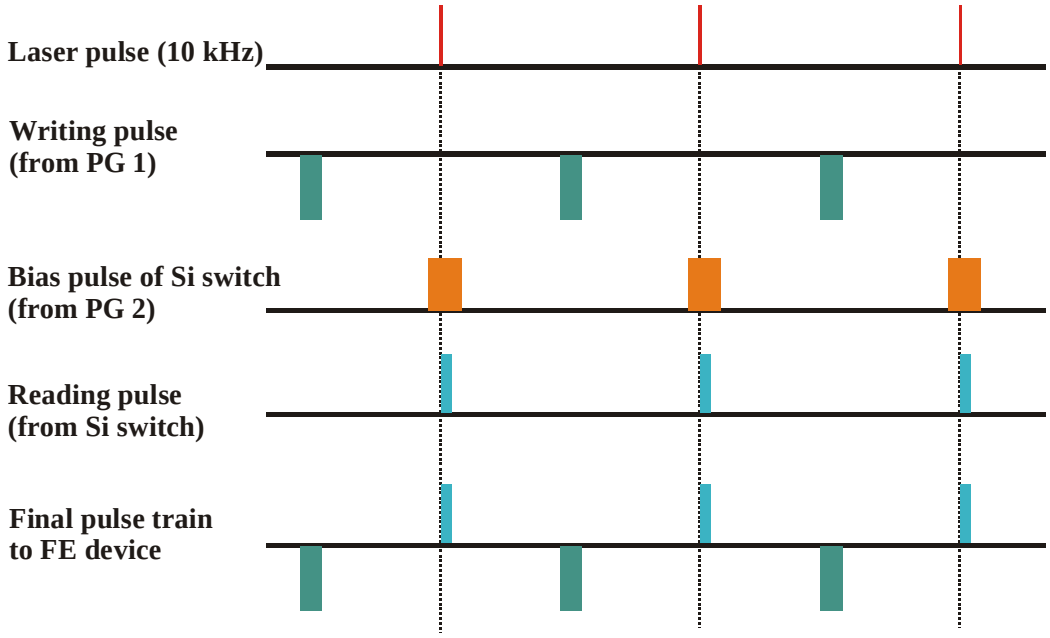

Figure 7-11 Time sequences of pulse trains.

Due to the high-speed transmission lines connected to the ferroelectric capacitors and the high-bandwidth sampling oscilloscope, the time resolution of our experimental setup depends only on the rise-time of the input electric pulse generated by the Si switch, which is ≅ 50-100 ps. Therefore our experimental system is capable of detecting the fast polarization switching for ferroelectric capacitors. A ≅ 220 ps polarization switching time is obtained for a 4.5×5.4 μm^2 capacitor. Modeling of the switching transients using the Ishibashi-Merz model [15, 139, 148, 149] yields a characteristic switching time of ≅ 70 ps. Moreover, systematic studies of the polarization switching process become feasible using our experimental system.

7.3 Physical Models for the Dynamic Properties of the Polarization Switching Process of Ferroelectrics

Mathematical modeling of the polarization switching process in ferroelectrics has been studied for many years. With the model one can connect the experimental data obtained by the pulse method to the microscopic domain polarization switching mechanism in ferroelectrics. Nevertheless, the theoretical interpretation of switching dynamics is still an open problem. In this section, we introduce in detail the most popular and widely accepted Ishibashi-Merz model [15, 139, 148, 149]. For the purpose of comparison, the Shur model [150-152] will also be covered.

7.3.1 Ishibashi-Merz Model

A. Ishibashi model

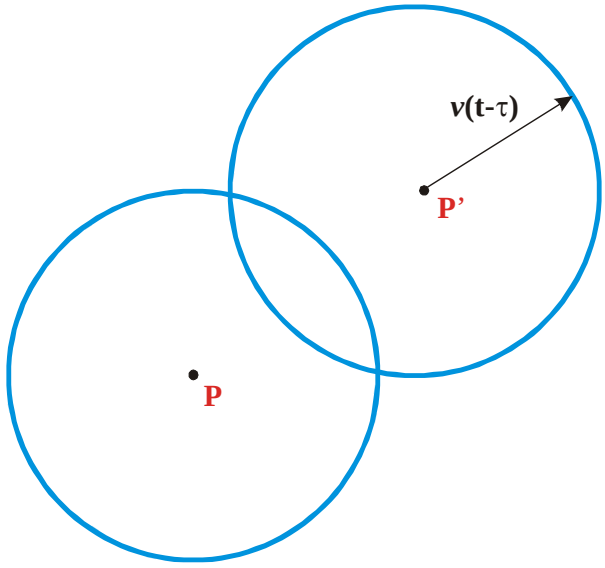

Figure 7-12 The area covered by the domain started at point P′ [153].

In this section we derive the Ishibashi model [153]. Our purpose is to obtain the relationship between the reversed domain area and the elapsed time for a ferroelectric material, or in other words, the fraction of the reversed domain as a function of time, $f(t)$.

Consider an infinite ferroelectric plane, we first calculate the probability $q(t)$ that a certain point is not covered by any reversed domain at time t given the start time of the polarization reversal process as time zero. Assuming the nucleus of a reversed domain appears at time τ ($\tau < t$) at the point P', then at time t this reversed domain will expand into a circle with radius $v(t-\tau)$ and center P', as shown in Figure 7-12, where v is the growth speed of the reversed domain. Therefore, if a nucleus appears at time τ within the distance of $v(t-\tau)$ to P, that is, the nucleus lies in a circle with center P and radius $v(t-\tau)$, P will be covered by this new reversed domain at time t. We denote the area of this circle as $S(t, \tau)$ which is a function of both time t and the time of the appearance of the new nucleus τ. If a reversed domain grows in one-dimension (as shown in Figure 7-13 (a)), $S(t, \tau)$ is given by

$$S_1(t,\tau) = 2v(t-\tau), \tag{7.9}$$

while if a reversed domain grows in two-dimensions (as shown in Figure 7-13 (b)), $S(t, \tau)$ is given by

$$S_2(t,\tau) = \pi v^2 (t-\tau)^2. \tag{7.10}$$

In general, we can write $S(t, \tau)$ as

$$S_d(t,\tau) = C_d [v(t-\tau)]^d, \tag{7.11}$$

where d is the dimensionality and C_d is a constant depending on d. Assuming that the nucleation probability at time τ is $J(\tau)$ (which denotes the number of the appearing nuclei per unit area per unit time at a specific time τ), the probability that no nucleus appears in $S(t, \tau)$ during a short period from τ to $\tau + \Delta\tau$ can be expressed as $1 - J(\tau)S(t,\tau)\Delta\tau$. By dividing the time by steps of $\Delta\tau$, we write $t = k\Delta\tau$ and $\tau = i\Delta\tau$. Therefore $q(t)$, the probability that P is not covered by any reversed domain, can be written as

$$q(t) = \prod_{i=0}^{k} [1 - J(i\Delta\tau)S(k\Delta\tau, i\Delta\tau)\Delta\tau]. \qquad (7.12)$$

When $\Delta\tau \to 0$, the logarithm of $q(t)$ can be expressed as

$$\ln q(t) = \sum \ln[1 - J(i\Delta\tau)S(k\Delta\tau, i\Delta\tau)\Delta\tau] \approx -\int_0^t J(\tau)S(t,\tau)d\tau\,. \qquad (7.13)$$

Therefore, the probability $f(t)$ that an arbitrarily selected point P is covered by the reversed domains, or the fraction of the reversed domains, is

$$f(t) = 1 - q(t) = 1 - \exp[-\int_0^t J(\tau)S(t,\tau)d\tau]. \qquad (7.14)$$

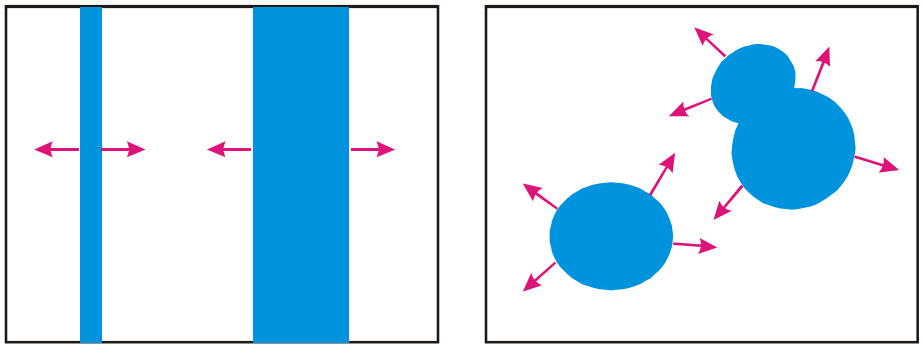

Figure 7-13 (a) One-dimensional and (b) two-dimensional domain expansions [153].

We consider the polarization reversal in two extreme cases. In the first one, $J(\tau)$ is a constant,

$$J(\tau) = R, \tag{7.15}$$

which suggests that the nucleation of the new domains can happen at any time during the polarization reversal process. This case is referred to as the α-model. The corresponding $f(t)$ is given by

$$f(t) = 1 - \exp[-\left(\frac{t}{t_\alpha}\right)^{d+1}], \tag{7.16}$$

where $\left(\frac{1}{t_\alpha}\right)^{d+1} = \frac{RC_d v^d}{d+1}$. In the second case, $J(\tau)$ is expressed as

$$J(\tau) = N\delta(\tau), \tag{7.17}$$

which means that the nucleation only takes place at $t = 0$. This case is referred to as the β-model. The corresponding $f(t)$ is given by

$$f(t) = 1 - \exp[-\left(\frac{t}{t_\beta}\right)^{d}], \tag{7.18}$$

where $\left(\frac{1}{t_\beta}\right)^{d} = C_d N v^d$.

Comparing the α-model and the β-model, the equations are similar being only different in dimensionality d. For example, the fitting result of $d = 2$ corresponds to 1-D domain growth with the α-model, and 2-D domain growth with the β-model.

In a practical polarization reversal process, both schemes may work simultaneously, and $f(t)$ is written as

$$f(t) = 1 - \exp[-\left(\frac{t}{t_\alpha}\right)^{d+1}]\exp[-\left(\frac{t}{t_\beta}\right)^{d}]. \quad (7.19)$$

Since this expression is complicated, we simplify it as

$$f(t) = 1 - \exp[-\left(\frac{t}{t_0}\right)^{n}], \quad (7.20)$$

where the exponent n is referred to as the dimensionality of the nucleating domain, and t_0 is the characteristic switching time which is the time at which 63% polarization has been switched with an infinite applied electric field. Being roughly equal to 63% of the intrinsic polarization switching time, t_0 is also an intrinsic parameter. Equation (7.20) is the mathematical expression of the so-called Ishibashi model.

It should be noted that in the derivation of the Ishibashi model, we assume that the film is infinitely large, which is not true in reality. This unrealistic assumption is one shortcoming of the Ishibashi model.

B. Merz model

The Ishibashi model only illustrates the time dependence of the fraction of the reversed polarization without considering the electric field. However, the experimental results show that the nucleation rate depends on the electric field E. Their relationship is given in the exponential form of [15]

$$J \propto \exp[-\left(\frac{\alpha}{E}\right)], \quad (7.21)$$

where α is called the activation field, reflecting the ease of the polarization reversal. If we only consider the effect of the electric field on the fraction of the reversed polarization as a function of time, *f*(*t*), we obtain

$$f(t) \propto 1 - \exp[-\exp\left(-\frac{\alpha}{E}\right)]. \qquad (7.22)$$

This equation expresses the Merz model. We note that the Merz model is a heuristic model based on experimental results, but not theory.

C. Ishibashi-Merz model

By combining the Ishibashi model and the Merz model we obtain the so-called Ishibashi-Merz model, as defined by

$$f(t) = 1 - \exp[-\exp\left(-\frac{\alpha}{E}\right)\left(\frac{t}{t_0}\right)^n]. \qquad (7.23)$$

Given an α, we could fit the experimental data and extract n and t_0, which are the parameters related to the domain polarization switching.

In conclusion, the Ishibashi-Merz model, in which the switching process can be described in terms of a classical solid-state phase transformation involving nucleation and growth of the reversed domains, is a bridge connecting experimental data obtained by the pulse method to the intrinsic polarization switching time.

7.3.2 Shur Model

The Shur model attempts to describe the polarization switching behavior of a realistic finite object. However its correctness is still under debate. Nevertheless, for the

sake of the completeness, we will explore this model and compare it with our experimental results.

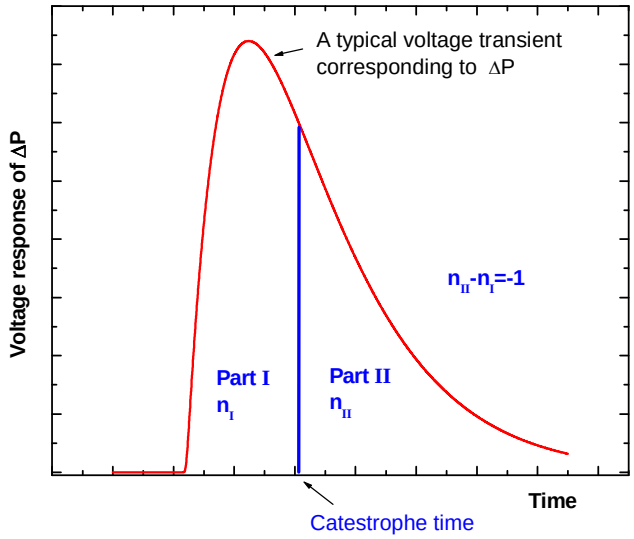

Figure 7-14 Illustration of the Shur model.

The main feature of the Shur model is the *catastrophe time*. According to this model, this *catastrophe time* divides the polarization switching process into two parts, part I and part II, as shown in Figure 7-14. Both parts can be fitted with equation

$$f(t) = 1 - \exp[-\left(\frac{t}{t_0}\right)^n \left(1 - \frac{t}{t_m}\right)], \tag{7.24}$$

where both t_0 and n have the same definition as in the Ishibashi model and t_m accounts for the impingement of the growing domains on the boundary of the media. The dimensionality n of part I is greater than that of part II by 1 ($\Delta n = n_{II} - n_I = -1$), or in other words, the data can only be fitted with 2D→1D or 3D→2D from part I to part II. Also, by

combining both Shur model and Merz model, we obtain Shur's express of $f(t)$ for each part,

$$f(t) = 1 - \exp[-\exp\left(-\frac{\alpha}{E}\right)\left(\frac{t}{t_0}\right)^n\left(1-\frac{t}{t_m}\right)]. \qquad (7.25)$$

According to Shur's explanation, the revision of the Ishibashi model is based on two considerations. First, the dimensionality *n* obtained by the Ishibashi model is commonly not an integer. Ishibashi has suggested that the mechanism of the polarization reversal is based on not only the α-model but also the β-model, as discussed in the previous section. However Shur thought this non-integer *n* is due to the unrealistic assumption of infinite device size in the Ishibashi model. Second, Shur found it almost impossible to describe the decaying part of the voltage transient using the Ishibashi model; or in other words, this experimentally obtained voltage transient could not be fitted well with the Ishibashi model. In one sense this claim could be true in that the tail part and the front part of the typical *ΔP* voltage transient (as shown in Figure 7-14, note the asymmetric feature of the ΔP voltage transient) have different shapes, consequently the experimental data could not be fitted well with a single dimensionality *n*, which describes the shape of the transient. However, on the other hand Shur failed to consider the fact that the experimental data are convoluted with circuit effects in the pulse method. As simulated in section 7.1, these circuit parameters certainly will affect the shape of the *ΔP* voltage transient and hence *n*. Our experimental results, which will be shown in the next section, will justify this argument. Therefore this asymmetric *ΔP* voltage transient may be due to the circuit effect and hence is not inherent for the polarization switching

process in ferroelectrics. And the catastrophe time may not make much sense. In section 7.4, the experimental results will verify our conjecture.

7.3.3 Calculation of *f*(*t*) from Experimental Data

The raw data obtained by the pulse method are the voltage transients corresponding to P^* and $P^\wedge$ processes. In order to fit these experimental data with the theoretical models discussed earlier, we review the approach of calculating $f(t)$ from the raw data.

The displacement current, $\Delta i(t)$, is related solely to the domain polarization switching process and can be expressed as

$$\Delta i(t) = \frac{V(t)_{p^*} - V(t)_{P^\wedge}}{50}, \tag{7.26}$$

where $V(t)_{P^*}$ and $V(t)_{P^\wedge}$ are the voltage transients displayed on the oscilloscope corresponding to the polarization switched and non-switched processes respectively. $\Delta P(t)$, which represents the switched polarization as a function of time, can be obtained by integrating the current transient $\Delta i(t)$,

$$\Delta P(t) = \frac{\int_0^\infty \Delta i(t)dt}{A_{FE}}, \tag{7.27}$$

where A_{FE} is the area of the capacitor. Given the total switched polarization P_{total}, $f(t)$ can be expressed as

$$f(switched) = \frac{\Delta P(t)}{P_{total}}. \tag{7.28}$$

In other words, $f(t)$ is the normalized $\Delta P(t)$ and represents the fraction of the switched domains as a function of time.

7.4 Experimental Results

In this section we present the experimental results for PNZT capacitors with the experimental setup described in section 7.2. Our intention is not only to obtain the most *accurate* intrinsic polarization switching time but also to investigate the effects of circuit parameters, specifically the rise-time of the input electric pulse and the capacitor size, on the polarization switching process.

7.4.1 The ≅ 220 ps Polarization Switching Time for a 4.5×5.4 μm^2 PNZT Capacitor

Figure 7-15 shows the 5 V step-like input electric pulse with a rise-time (10%-90%) of ≅ 68 ps, which is generated by a Si photoconductive switch. Figure 7-16 (a) and (b) show the corresponding voltage responses of P^*, $P^\wedge$ and ΔP processes for a 4.5×5.4 μm^2 PNZT capacitor. The polarization switching time t_s, which is defined as the time from the onset of switching to the point 90% down from the maximum, is ≅ 220 ps.

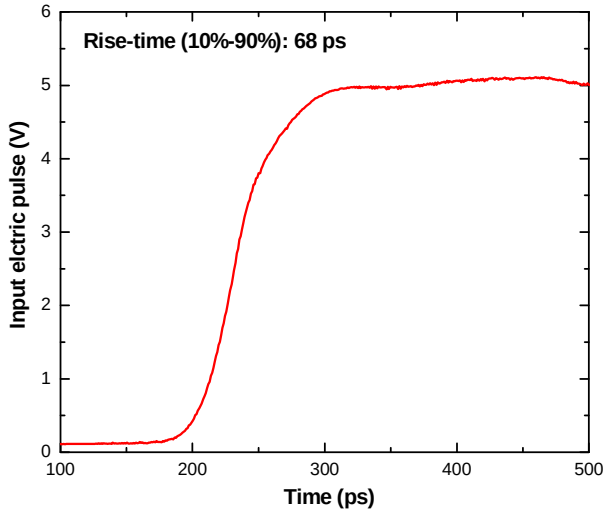

Figure 7-15 An input 5 V electric pulse generated by a Si photoconductive switch.

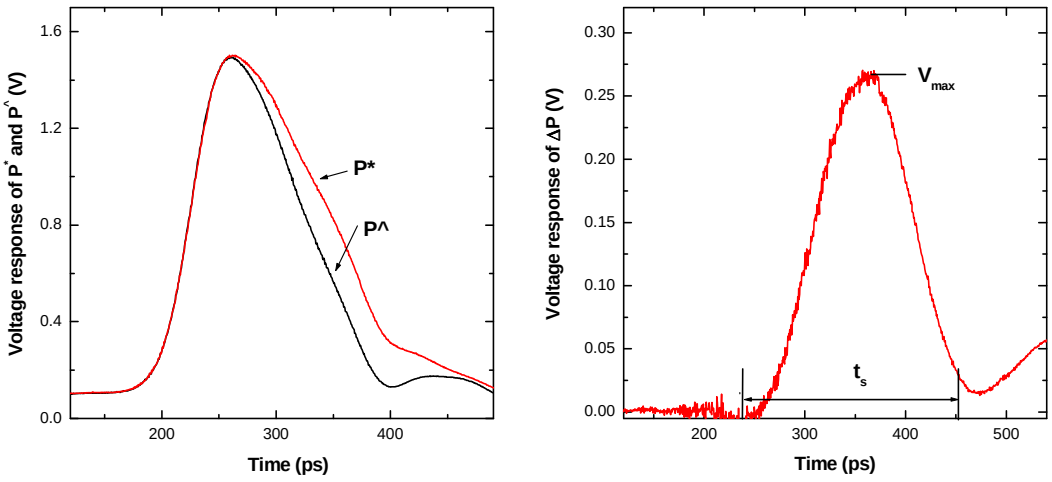

Figure 7-16 Voltage responses of P^*, $P^\wedge$, and ΔP processes for a 4.5×5.4 μm^2 PNZT capacitor.

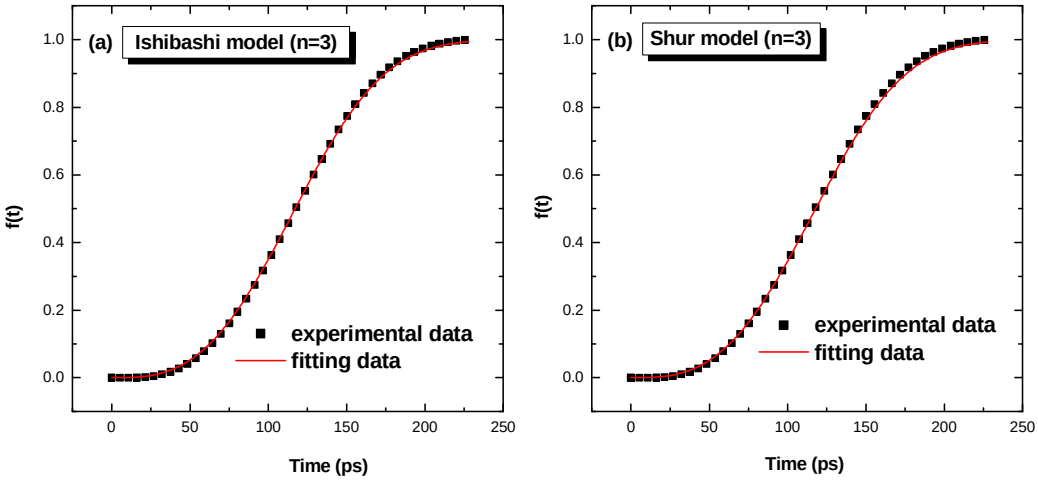

Figure 7-17 Plots of $f(t)$ and its fitting curve using (a) the Ishibashi-Merz and (b) the Shur-Merz model for a 4.5×5.4 μm^2 PNZT capacitor.

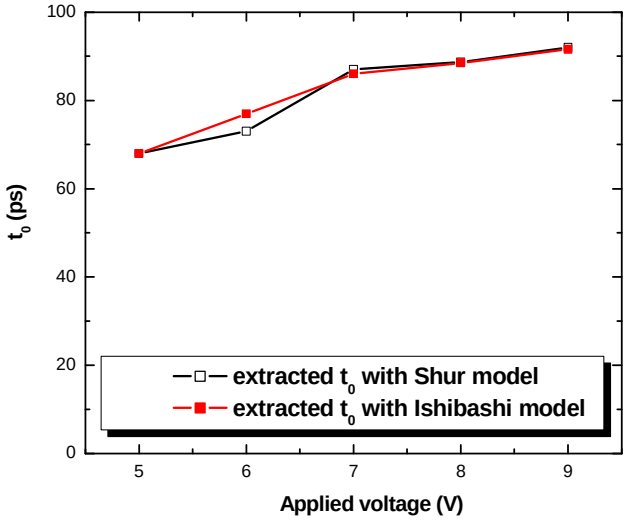

Figure 7-18 Electric field dependence of t_0 for a 4.5×5.4 μm^2 PNZT capacitor.

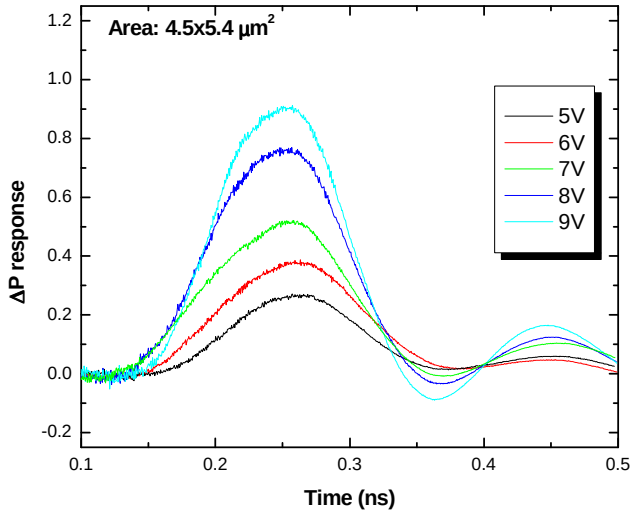

Figure 7-19 Voltage responses of ΔP processes for various amplitudes of input electric pulses for a 4.5×5.4 μm^2 PNZT capacitor.

If we assume that the domain walls propagate with a field dependent speed $v = \mu E$ and a mobility $\mu \cong 2.4\times10^{-4}$ m^2/Vs [154], then the intrinsic polarization switching time in a 200 nm PNZT film is ≅ 80 ps for a 5 V pulse. We try to extract the intrinsic polarization switching time from the above results. As discussed earlier, the polarization switching process can be described by the Ishibashi-Merz model (refer to equation (7.23)) or the Shur-Merz model (refer to equation(7.25)). We use these two inter-related models to fit experimental data for the 4.5×5.4 μm^2 capacitor for different applied fields. According to section 7.3.4, $f(t)$ can be obtained by the integration of the current transient normalized by the maximum polarization. Figure 7-17 (a) and (b) show the plots of $f(t)$ and the corresponding fitting curves using the Ishibashi-Merz model and the Shur-Merz model. A 500 kV/cm activation field [147] is used for fitting experimental data. The general approach to fitting the $f(t)$ using the Ishibashi model is by varying both t_0 and n.

As a result, a non-integral value of dimensionality n is typically obtained. In our original fitting, we varied both t_0 and n and obtained an $n \cong 3.1$. However we recognize that the interpretation of the switching data is more meaningful if n is an integer, enabling us to identify the actual nucleation and growth mechanism. Therefore in our fitting, we fix n to be 3.0 and extract the t_0 value from the current transient data. The excellent fit of the experimental data with the model, Figure 7-17 (a), is noteworthy. Furthermore, we do not observe any significant change in the fit as a consequence of changing the n value from 3.1 to 3.0, thus supporting the validity of fixing $n = 3$. A t_0 of $\cong$ 68 ps is obtained for this capacitor with $n = 3$ and the field dependence is shown in Figure 7-18. We notice that t_0 increases with the applied electric field. This is due to the Merz model, in which the polarization switching time t_s is assumed to be a function of the electric field. The Merz model is based on the experimental results obtained in a slow measurement, at least on the order of tens of nanoseconds. However, in our experiment, which could measure effects on the order of hundreds of picoseconds, we do not observe a significant variation of t_s with the electric field, as shown in Figure 7-19, which illustrates the ΔP voltage transient with different amplitudes of the input electric pulses. Therefore, if we still use the Merz model in the fitting, we will find that t_0 increases with the amplitude of the input electric field.

We also attempt to fit the switching transients using the Shur model, Figure 7-17 (b), in which the polarization switching process is separated into two or three stages with different dimensionalities [152]. All stages of the dynamic process can be described by the same equation (7.25) except that the dimensionality changes by integral values for each stage. However, our data could not be fitted well with such a multi-stage switching

process. We note that the shape of our switching transient is distinctly different from that presented by Shur [152], thus suggesting one possible cause for our inability to extract meaningful parameters through a multi-stage switching process. Actually, the shape of the switching transient is greatly affected by circuit parameters, as will be shown later. It is certain that less circuit effect leads to more accurate fitting results. Furthermore, the time scales involved in these two measurements are significantly different (*i.e.*, picoseconds versus microseconds). Finally, we observe that the quality of the fit using the Shur model improves as the t_m value is progressively increased, although the t_0 value itself does not change. This can be simply understood as a consequence of the fact that the $(1-t/t_m)$ term approaches unity as t_m becomes much larger than '*t*'. Under such conditions, the Shur model converges into the Ishibashi model.

What is the meaning of the observed value of $n = 3$? We presented earlier that two limiting situations of the reversal process are usually considered in both the Ishibashi [148] and the Shur [152] models, termed as the α-model and β-model. In the α-model, reverse nuclei arise throughout the whole process and in the β-model reversal is caused by nuclei that pre-exist at the beginning of the process. The fitting equations for the α and β models are the same except the dimensionality n is different. Therefore, $n = 3$ corresponds to 2-D growth of reverse domains in the α-model and 3-D growth in the β-model. Differentiating between these two possibilities is complicated by the polycrystalline nature of the films used in this study; however, we suspect that 3-D reversal is unlikely (as surmised by Ishibashi [148]).

Also we note that the value of n determined from fitting the switching transients is extremely sensitive to the size of the capacitor (which will be discussed in the following

sections); increasing the capacitor size lowers the *n* value, presumably due to a significant convolution from capacitive *RC*-effects. We have observed that the capacitor size and therefore the *RC*-time constant directly influence the shape of the ΔP response (*i.e.*, produce a long "tail"), and consequently the fitting results. Therefore, it is clearly important to reduce the *RC* time constant of the test structure to a value smaller than the expected t_0 value (*i.e.*, smaller than ≅ 50 ps). For the 4.5×5.4 μm^2 size capacitor, we estimate a *RC*-time constant value of ≅ 45 ps.

7.4.2 Impact of the Capacitor Area on the Measurement

In this section we discuss the influence of the capacitor area on the polarization switching measurement. We find that the switching transient is very sensitive to the capacitor size.

Figure 7-20 shows the voltage responses corresponding to the polarization switching (P^*) and non-switching ($P^\wedge$) cases, and ΔP for ferroelectric capacitors with various areas. The fact that the measured switching time, t_s, is larger than the rise-time of the input electric pulse suggests that the time resolution of our setup is sufficient for this size of capacitor. With the decrease of capacitor area, the polarization switching time decreases because of the RC_{FE} limitation. The shapes of the P^*, $P^\wedge$, and ΔP responses vary just as expected by simulation with various sizes of capacitors.

Figure 7-21 shows the plots of $f(t)$ and the corresponding fitting curves using the Ishibashi-Merz model for different capacitor sizes. Using the above model we extracted t_0 and dimensionality *n* from $f(t)$. Figure 7-22 shows the dependence of t_s and t_0 on capacitor size. Both t_s and t_0 decrease linearly with area, illustrating the RC_{FE} time limitation. The fitting parameter t_0, which is assumed to be intrinsic, should not depend

on capacitor area. However our data clearly show that t_0 varies with capacitor size, although this change is less than that of t_s. The reason for this discrepancy could be that circuit factors in the polarization switching process are not considered by the Ishibashi-Merz model. Therefore, with a sufficiently small size capacitor, t_0 is expected to converge to a constant value, which should be the intrinsic one. Figure 7-23 shows that dimensionality n varies with the capacitor area. Is this variation intrinsic or circuit parameter related? We will discuss this question shortly.

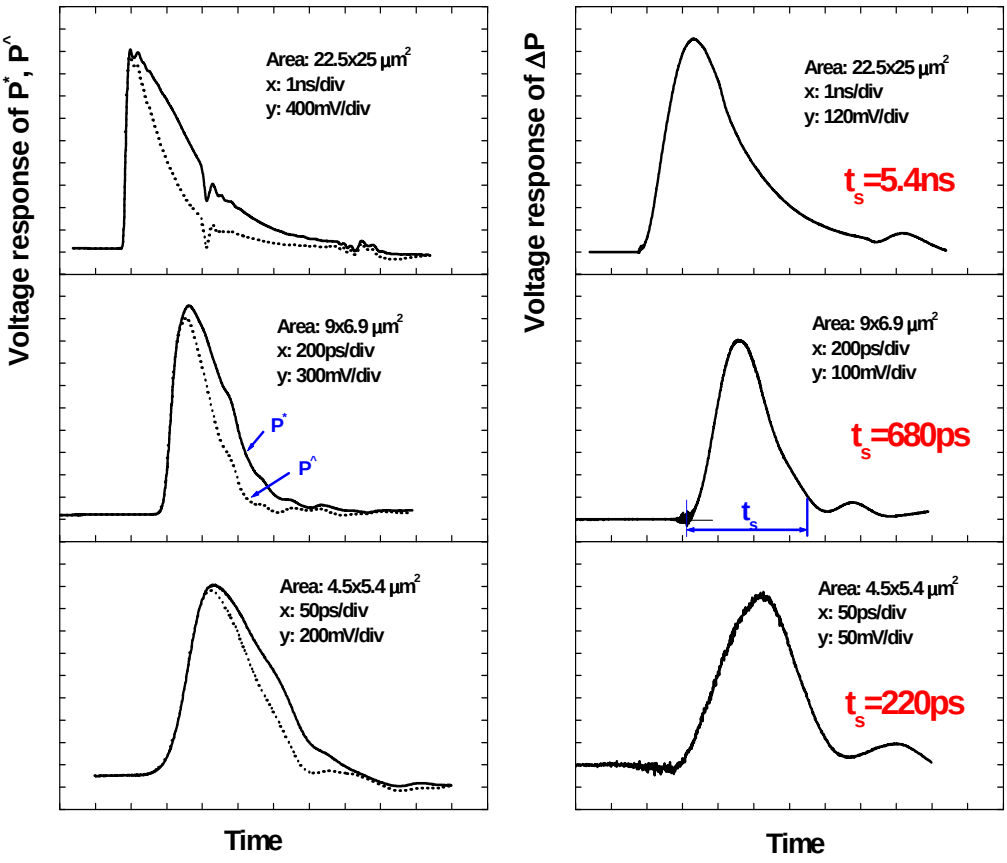

Figure 7-20 Voltage responses of P*, P^, and ΔP processes for various capacitor areas. The amplitude of the input electric pulse is 6 V.

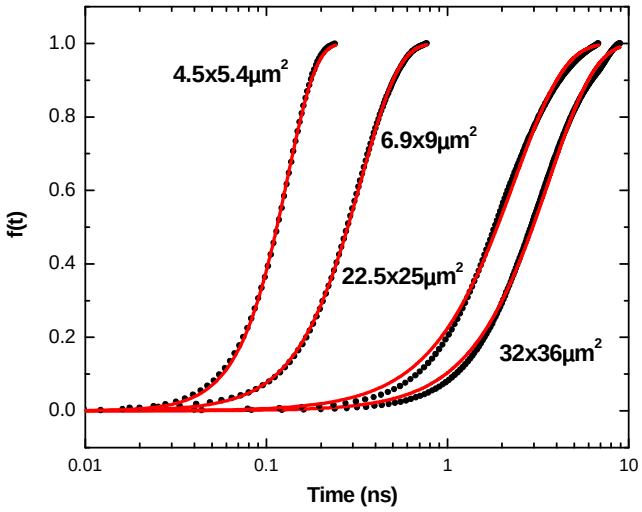

Figure 7-21 Plots of measured (dot line) and fitted (solid line) $f(t)$ curves for various capacitor areas.

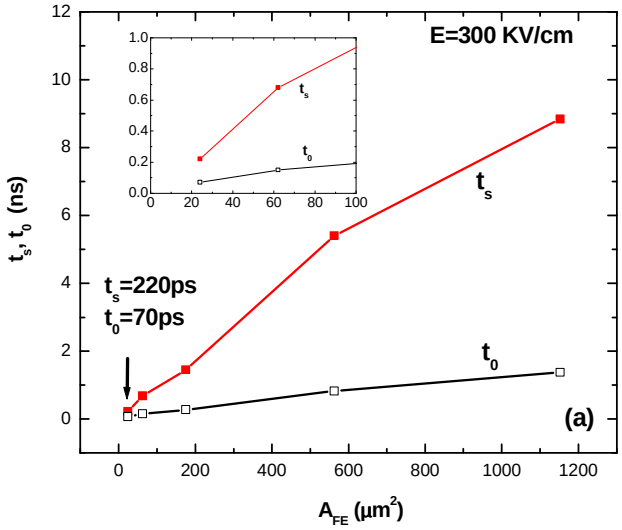

Figure 7-22 Polarization switching time t_s and characteristic switching time t_0 as functions of capacitor area. The inset shows the front part of the curve.

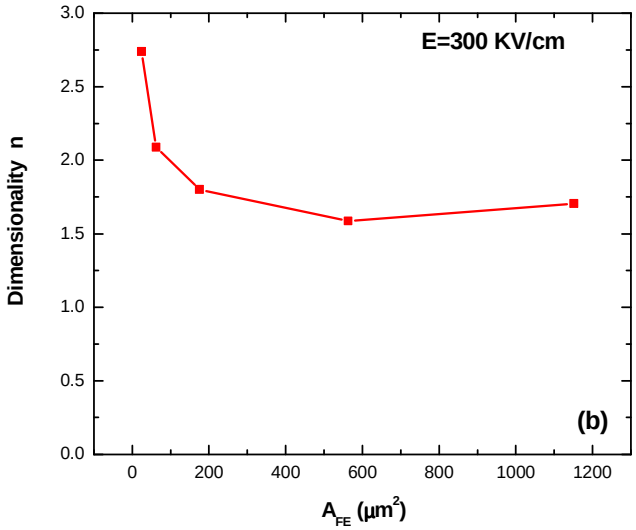

Figure 7-23 Dimensionality *n* as a function of capacitor area.

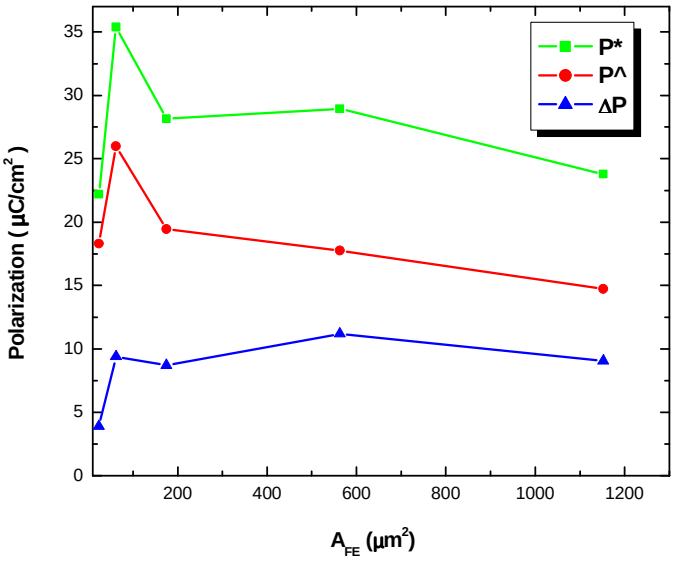

Figure 7-24 Non-switched polarization (P^), switched polarizaiton (P*), and ΔP as functions of capacitor area.

Figure 7-24 shows the dependence of the non-switched polarization ($P^{\wedge}$), switched polarization (P^{*}), and their difference ΔP on capacitor size. Since the calculation of the polarization has already taken into account the area, the ΔP values should be the same. However, there is an obvious decrease of polarization for the 4.5×5.4 μm^2 capacitor. The reason for this could be that the effective area of this capacitor is much smaller than expected. Conversely, it is possible that there is a real decrease in switched polarization due to processing damage, which is likely to occur in smaller size capacitors.

7.4.3 Impact of the Rise-time of the Input Step-like Electric Pulse on the Measurement

Similarly, a study is also carried out on the effect of the rise-time of the input electric pulse on the polarization switching process. The rise-time was varied by using cable delay lines with various lengths. The dispersion of the cables will stretch the rise-time of the input electric pulse; therefore the application of a longer cable results in a slower rise-time.

Figure 7-25 shows the voltage transients of the ΔP process for various rise-times of the input electric pulses for a 12.5×14 μm^2 ferroelectric capacitor. The rise-time dependent data are fitted to the Ishibashi-Merz model to extract the characteristic switching time t_0 and dimensionality n. Figure 7-26 shows the polarization switching time t_s and the extracted characteristic polarization switching time t_0 as functions of the rise-time of the input electric pulse. The curves are very similar to what are expected from simulation. It clearly shows that for the capacitor with this area, a faster or even zero rise-time of the input electric pulse will not yield the intrinsic switching time. The

time resolution of the experimental setup is completely limited by the circuit RC_{FE}. Figure 7-27 shows the dimensionality *n* as a function of the rise-time of the input electric pulse. It is clear that the rise-time indeed influences the *n* value.

We have observed that: (1) *n* varies with capacitor area, as illustrated in Figure 7-23; and (2) even for a specific capacitor, *n* is not a constant, *n* varies with the rise-time of the input electric pulse, as shown in Figure 7-27. Along with the fact that both the capacitance and rise-time are the circuit parameters, we conclude that the changing of dimensionality *n* is due to the circuit influence. Moreover, the fact that a decrease in rise-time or an increase in capacitor area gives rise to the same trend on *n* further proves the circuit impact on *n* since we already explained in simulations that the decrease of rise-time and increase of capacitor area have the same effect on the impedance of the capacitor. From another point of view, changing the rise-time and capacitor area causes the change of impedance ratio of the capacitor to the 50 Ω resistor (as introduced in section 7.1), which defines the shapes of the P^* and $P^\wedge$ responses, and hence that of the ΔP response. Different shapes of ΔP voltage responses will have different dimensionality *n* since *n* is a shape factor in the fitting. Therefore, the changing of circuit parameters results in different *n* values. It is certainly true that the smaller the capacitor size and the faster the rise-time of the input electric pulse, the more reliable the fitted values of t_0 and *n* will be.

Figure 7-28 shows the non-switched polarization ($P^\wedge$), switched polarization (P^*), and their difference ΔP as functions of the rise-time of the input electric pulse. Regardless of the rise-time, the ΔP value should be constant since the polarization

switching is an integration process. This point is clearly illustrated in the figure where the curves are relatively flat.

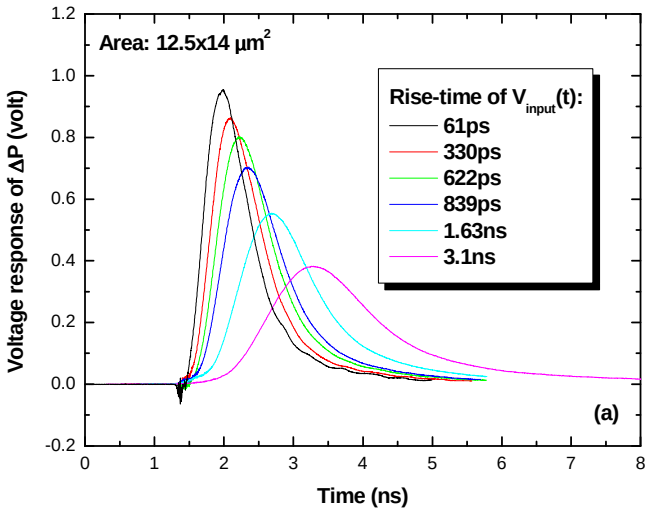

Figure 7-25 Voltage responses of the ΔP process for various rise-times of the input electric pulses for a 12.5×14 μm^2 ferroelectric capacitor. The amplitude of the input electric pulse is 5V.

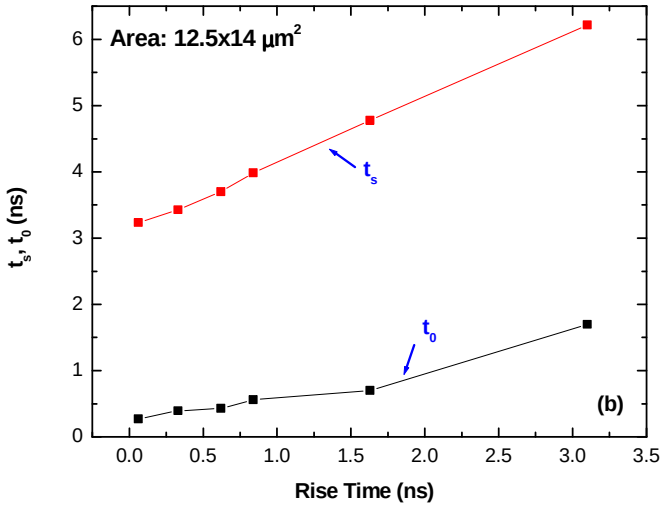

Figure 7-26 Polarization switching time t_s and characteristic switching time t_0 as functions of the rise-time of the input electric pulse for a 12.5×14 μm^2 PNZT capacitor.

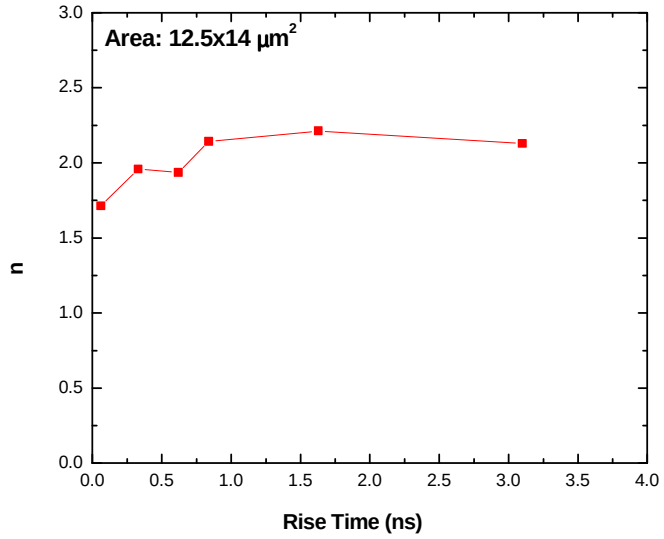

Figure 7-27 Dimensionality *n* as a function of the rise-time of the input electric pulse for a 12.5×14 μm^2 PNZT capacitor.

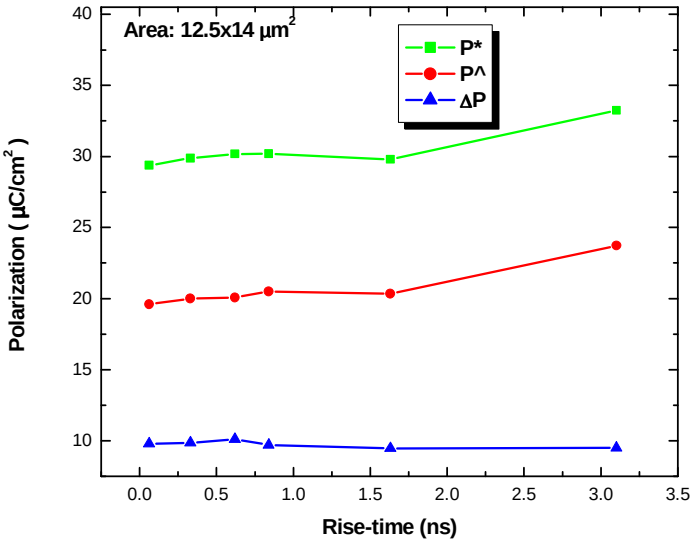

Figure 7-28 Non-switched polarization (P^), switched polarization (P*), and ΔP as functions of the rise-time of the input electric pulse.

7.4.4 Activation field

When Merz studied barium titanate single crystals, he introduced a parameter, called the activation field (α), which indicates the ease of the polarization switching [15]. The activation field can be calculated from the switching transients with different input electric pulse amplitudes, as described by:

$$\ln(\Delta i_{\max}) = \ln i^{'} - \alpha d \frac{1}{V}, \qquad (7.29)$$

where Δi_{max} is the maximum value of $i(t)$, V is the amplitude of the applied bias voltage, and d is the film thickness. The slope of the linear fit of $\ln(\Delta i_{max})$ as a function of $1/V$ yields the activation voltage αd, and consequently α given the thickness d. Figure 7-29, Figure 7-30, Figure 7-31, and Figure 7-32 show the current responses of the ΔP process for various pulse amplitudes for capacitors with areas of 36×32 μm^2, 22.5×25 μm^2, 6.9×9 μm^2, and 4.5×5.4 μm^2 respectively. Each inset shows the logarithm of Δi_{max} as a function of $1/V$, and the linear fitting curve.

Figure 7-33 shows the activation field α as a function of the capacitor area. Clearly, α tends to increase with a decrease in capacitor size. It is possible that the change in α is due to the change in shape of the ΔP response for capacitors of various sizes. It is interesting that when we compare the curves of α, n and $f(t_{peak})$ as functions of capacitor area, (Figure 7-33, Figure 7-23 and Figure 7-34 respectively), we find that they show a similar trend. While t_{peak} is the time when the ΔP transient reaches the maximum value, $f(t_{peak})$ represents the fraction of polarization that has been switched at

time t_{peak}, which is also related to the shape of ΔP. It certainly shows that α is not extremely robust, but a function of circuit parameters.

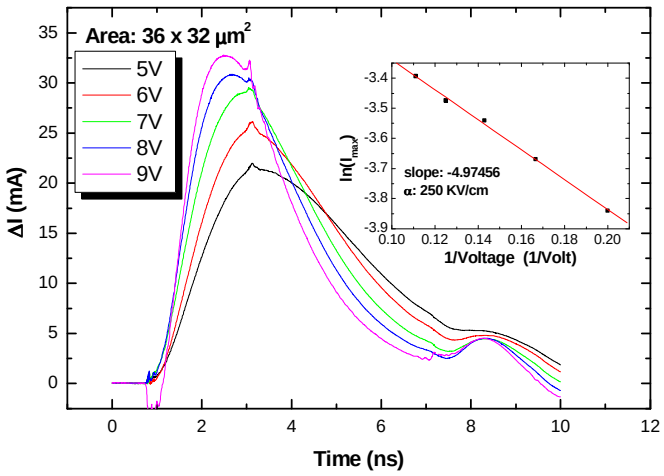

Figure 7-29 Current responses of ΔP processes for various amplitudes of input electric pulses for a 36×32 μm^2 capacitor. The inset shows the plot of ln(Δi_{max}) vs. 1/V and its linear fitting curve.

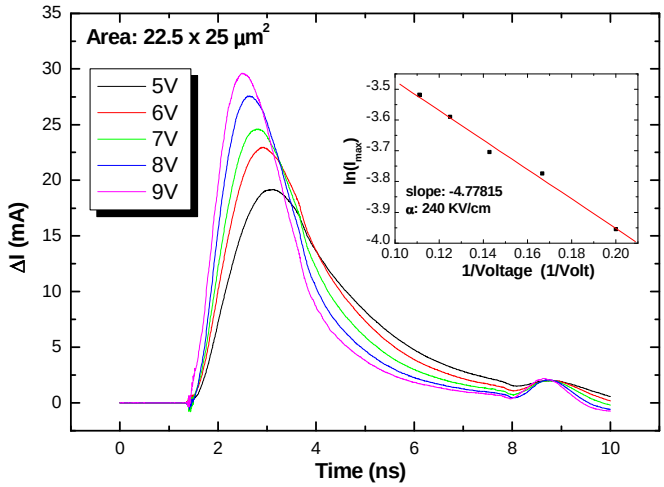

Figure 7-30 Current responses of ΔP processes for various amplitudes of input electric pulses for a 22.5×25 μm^2 capacitor. The inset shows the plot of ln(Δi_{max}) vs. 1/V and its linear fitting curve.

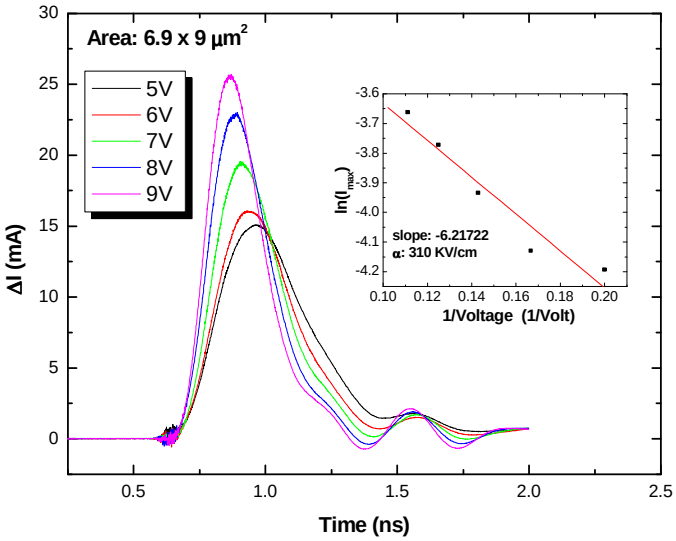

Figure 7-31 Current responses of ΔP processes for various amplitudes of input electric pulses for a 6.9×9 μm^2 capacitor. The inset shows the plot of ln(Δi_{max}) vs. 1/V and its linear fitting curve.

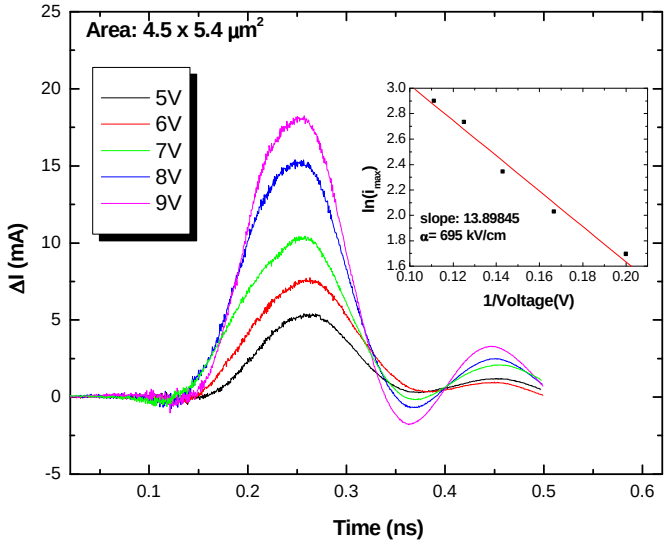

Figure 7-32 Current responses of ΔP processes for various amplitudes of input electric pulses for a 4.5×5.4 μm^2 capacitor. The inset shows the plot of ln(Δi_{max}) vs. 1/V and its linear fitting curve.

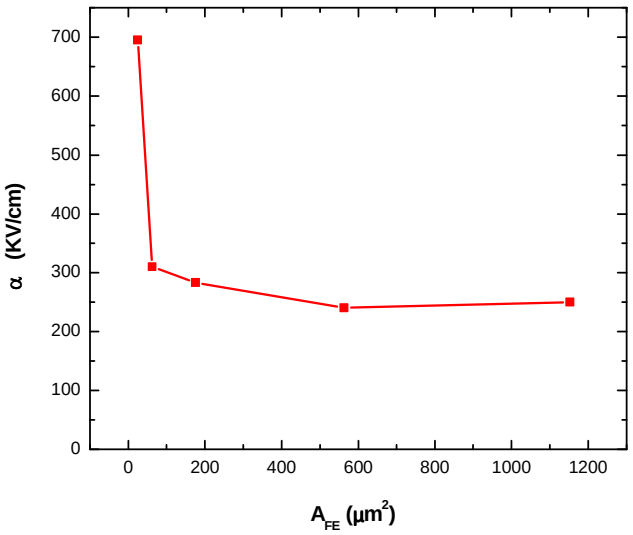

Figure 7-33 Activation field α as a function of capacitor area.

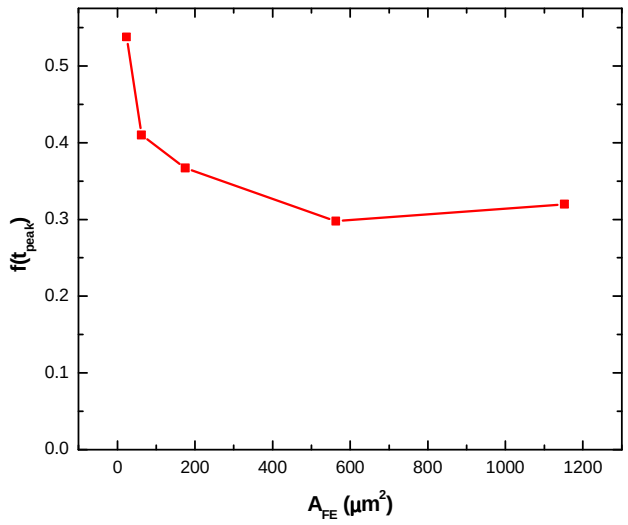

Figure 7-34 $f(t_{peak})$ as a function of capacitor area.

Chapter 8 Conclusion and Future Work on the Study of Polarization Switching Dynamics of Ferroelectric Thin Film Capacitors

In this thesis we systematically studied the ultrafast polarization switching dynamics of $Pb(Nb,Zr,Ti)O_3$ (PNZT) ferroelectric capacitors.

The approach we utilized is the widely applied pulse method, which can directly measure the domain switching speed. Numerical simulations of the circuit of this method were carried out to investigate the impact of circuit parameters on the experimental results. It has been shown that in order to obtain the accurate intrinsic polarization switching time, the rise-time of the input electric pulse and the capacitor area, or equivalently the RC_{FE} time constant, must be as small as possible or at least on the same order as the intrinsic switching time, which is estimated theoretically ≅ 50 ps.

In this thesis, we designed and realized a novel experimental setup with a time resolution as small as ≅ 50-100 ps to study the fast polarization switching processes in ferroelectric capacitors. In this setup a semiconductor photoconductive switch actuated by an ultrafast laser pulse is utilized as a fast '*pulse generator*' to produce jitter-free, step-like electric pulses with fast rise-times. The input pulse rise-time limitation on obtaining the intrinsic polarization switching time is mostly eliminated.

The experiments were conducted on fully integrated ferroelectric PNZT capacitors by varying either the capacitor size or the rise-time of the input electric pulse.

For a 4.5×5.4 μm^2 PNZT capacitor, a switching time t_s of ≅ 220 ps was obtained, which is to our knowledge, the fastest switching time ever reported. From the experimental data we confirmed that in order to obtain the real intrinsic polarization switching time both the rise-time of the input electric pulses and the capacitor size have to be sufficiently small. The polarization switching time measurement is limited by the larger of the two parameters, namely the RC-time constant and the rise-time of the input electric pulse. In other words, the rise-time becomes important only when the capacitor size is small enough. For larger size capacitors, a fast rise-time will still result in a large switching time since it is now limited by the RC-time constant of the capacitor. For smaller size capacitors, a longer rise-time will still result in a larger switching time. Only when the above two parameters work together can one obtain a switching time that is close to the intrinsic switching time.

The experimentally obtained switching transients were fitted with the widely accepted Ishibashi-Merz model in order to extract the inherent parameters associated with the domain switching process, namely the characteristic switching time t_0 and the domain growth dimensionality n. A ≅ 70 ps characteristic switching time was obtained for a 4.5×5.4 μm^2 PNZT capacitor. In the Ishibashi-Merz model, t_0 and n are supposed to be intrinsic parameters. However, it was shown that both parameters are extremely sensitive to the capacitor size and the rise-time of the input electric pulse. This circuit parameter dependence of t_0 and n is due to the inevitable distortion of the experimental data by circuit effects in the pulse method, while the Ishibashi-Merz model is a theoretical model solely based on the physical process of the polarization switching. During the study, we also noted that the circuit parameters also affect the shape of the switching transient.

Since the dimensionality n is a parameter reflecting the shape of the transient curve, varying the circuit parameters will change the value of n. Nevertheless, it is certainly true that less circuit impact leads to greater reliability of the fitting results.

Circuit influence on the activation field, α, which reflects the ease of the polarization switching, was also studied. The experimental data showed that α is not independent of the circuit parameters; specifically it varies with the capacitor area.

Future work can be carried out in three directions:

(1) We consider the improvement of the pulse method. Since the fast rise-time of the input electric pulse and the small size of the capacitor are two essential concerns for obtaining the intrinsic polarization switching time and studying the domain switching mechanism, future work should be focused on these two aspects. As for the rise-time, except for using a Si photoconductive switch to generate fast pulses, is there a better way to obtain even faster rise-times? Or is there any other semiconductor material that can generate pulses with faster rise-times? All these questions should be explored deeper in future research. With respect to the capacitor size, to date the smallest well-integrated capacitor we have is $4.5 \times 5.4\ \mu m^2$. The term '*well-integrated*' means that the capacitor is connected to transmission lines by wire bonding pads, which is essential for high-speed measurements. During the thesis work, we tried to reduce capacitor size with the Focused Ion Beam technology. However, it was not successful. We have not found a feasible approach for obtaining a smaller size capacitor so far. Future research can be directed in this direction. Another option for investigation is a nanosize ferroelectric capacitor. Recent work demonstrated that nanosize capacitors could be produced. However in order to measure them, instruments such as an AFM are required. Therefore a new design with

high-speed transmission lines integrated with the AFM system, enabling the ultrafast polarization switching study of ferroelectric capacitors, should be considered. Another potential area of study for nanosize capacitors is to develop techniques to directly fabricate the '*well-integrated*' nanosize capacitors. Future work in these directions are promising.

(2) The Ishibashi-Merz model, which does not consider circuit effects on the polarization switching process, should be improved to well extract domain polarization switching dynamics from the experimental data obtained by the pulsed method.

(3) In this thesis the devices we studied are polycrystalline PNZT capacitors. In order to fully understand the polarization switching process, studies should cover single-crystal PZT, as well as other ferroelectrics.

(4) Considering the limited bandwidth (20 GHz) of the oscilloscope used in the pulse method, a new optical method is worthy of exploration for the study of ultrafast polarization switching dynamics in ferroelectric capacitors.

Appendix A Runga-Kutta Method

Runga-Kutta method is one of the major classes of practical numerical methods solving initial value problems for ordinary differential equations (ODEs).

The classical fourth order Runga-Kutta solutions of the first order ODE equation

$$\frac{dy}{dt} = f(t, y) \tag{A-1}$$

are given by:

$$\begin{aligned}
k_1 &= hf(t_n, y_n) \\
k_2 &= hf(t_n + \frac{1}{2}h, y_n + \frac{1}{2}k_1) \\
k_3 &= hf(t_n + \frac{1}{2}h, y_n + \frac{1}{2}k_2) \\
k_4 &= hf(t_n + h, y_n + k_3) \\
t_{n+1} &= t_n + h \\
y_{n+1} &= y_n + \frac{1}{6}[k_1 + 2k_2 + 2k_3 + k_4]
\end{aligned} \quad . \tag{A-2}$$

Given the values of x_n, y_n and a step size of h between x_n and x_{n+1}, y_{n+1} can be calculated. The final solution can be obtained by repeating the iterative operations. This is an explicit solution procedure in that one can calculate the values for the next iteration entirely form the current values.

The formulas of the classical fourth order Runga-Kutta solution of the coupled first order ODEs

$$\begin{cases} \dfrac{dy}{dt} = f(t, y, z) \\ \dfrac{dz}{dt} = g(t, y, z) \end{cases} \tag{A-3}$$

are given by:

$$\begin{aligned}
k_1 &= hf(t_n, y_n, z_n) \\
m_1 &= hg(t_n, y_n, z_n) \\
\\
k_2 &= hf\left(t_n + \frac{1}{2}h, y_n + \frac{1}{2}k_1, z_n + \frac{1}{2}m_1\right) \\
m_2 &= hg\left(t_n + \frac{1}{2}h, y_n + \frac{1}{2}k_1, z_n + \frac{1}{2}m_1\right) \\
\\
k_3 &= hf\left(t_n + \frac{1}{2}h, y_n + \frac{1}{2}k_2, z_n + \frac{1}{2}m_2\right) \\
m_3 &= hg\left(t_n + \frac{1}{2}h, y_n + \frac{1}{2}k_2, z_n + \frac{1}{2}m_2\right) \\
\\
k_4 &= hf(t_n + h, y_n + k_3, z_n + m_3) \\
m_4 &= hg(t_n + h, y_n + k_3, z_n + m_3) \\
\\
t_{n+1} &= t_n + h \\
y_{n+1} &= y_n + K \\
z_{n+1} &= z_n + M \\
K &= \frac{1}{6}(k_1 + 2k_2 + 2k_3 + k_4) \\
M &= \frac{1}{6}(m_1 + 2m_2 + 2m_3 + m_4)
\end{aligned} \tag{A-4}$$

Appendix B Derivation of Initial Condition for R-T Equation Simulation

When simulating the R-T equation, the first step is to estimate the quasiparticles density rate induced by laser illumination, which is the driven source of the subsequent non-equilibrium process. In this appendix, we estimate the photon-induced quasiparticles density rate, $i_{qp}(t)$ (in unit of $\frac{\#}{s \cdot m^3}$), for the R-T equation simulation. In order to do so, we first discuss how to derive the intensity profile for each laser pulse from the average power of the laser, P.

If the repetition rate of the laser is $f_{repetition}$, then the energy per pulse, E, is:

$$E = \frac{P}{f_{repetition}} \ . \qquad \text{(B-1)}$$

We assume that the laser pulse intensity $I(t)$, with unit of $\frac{W}{cm^2}$, is of Gaussian distribution

$$I = I_0 e^{-(\frac{t-t_0}{\tau_0})^2} , \qquad \text{(B-2)}$$

where τ_0 is the pulse width. Thus the energy per pulse can be obtained through integrating equation (B-2). E can be expressed by:

$$E = \sqrt{\pi} I_0 \tau_0 wl , \qquad \text{(B-3)}$$

where w, l are the width and length of the focus spot of the laser respectively. Comparing equation (B-1) and (B-3), I_0 can be obtained

$$I_0 = \frac{P}{f_{repetition} \cdot \sqrt{\pi}\tau_0 wl}. \qquad \text{(B-4)}$$

Substituting equation (B-4) into (B-2), the intensity profile of each pulse as a function of time is obtained. If the absorption coefficient of the YBCO thin film is δ, the reflection of the light on the surface is R, the film thickness is d, the fraction of the light illuminating on YBCO thin film is α, then the laser actually absorbed can be written as

$$I_{real} = I_0 \alpha (1-R)(1-e^{-\frac{d}{\delta}}) e^{-(\frac{t-t_0}{\tau_0})^2}. \qquad \text{(B-5)}$$

The wavelength of the laser is ≅ 800 nm, which corresponds to ≅ 1.5 eV. Hence the number of photons per unit volume per time generated with average laser power P can be expressed as

$$n_{photon} = \frac{I_{real}}{d \cdot (1.5eV)}. \qquad \text{(B-6)}$$

Assuming that the number of quasiparticles created by one photon is η, the total quasiparticle density rate, $i_{qp}(t)$ (in unit of $\frac{\#}{s \cdot m^3}$), generated by the laser illumination is:

$$i_{qp}(t) = n_{photon} \cdot \eta = \frac{P\alpha(1-R)(1-e^{-\frac{d}{\delta}})}{f_{repetition} dwl\sqrt{\pi}\tau_0 \cdot (1.5eV)} \cdot \eta \cdot e^{-(\frac{t-t_0}{\tau_0})^2} \qquad \text{(B-7)}$$

Appendix C Derivation of Initial Condition for 2-T Equation Simulation

In this appendix, we estimate the absorbed laser power per unit volume, $p(t)$ (in unit of $\frac{W}{m^3}$), for the 2-T equation simulation. From equation (B-5), we could straightforwardly obtain p(t), the power of the absorbed optical radiation per unit volume as a function of time. It is given by

$$p(t) = \frac{P\alpha(1-R)(1-e^{-\frac{d}{\delta}})}{f_{repetition} dwl\sqrt{\pi}\tau_0} \cdot e^{-(\frac{t-t_0}{\tau_0})^2} . \qquad \text{(C-1)}$$

REFERENCES

[1] J. G. Bednorz and K. A. Müller, "Possible high-Tc superconductivity in the Ba-La-Cu-O System," *Z. Phys. B Con. Mat.*, Vol. 64, p. 189-193, 1986.

[2] A. Frenkel, M. A. Saifi, T. Venkatesan, P. England, X. D. Wu, and A. Inam, "Optical-response of nongranular high-Tc $Y_1Ba_2Cu_3O_{7-X}$ superconducting thin-films," *J. Appl. Phys.*, Vol. 67, p. 3054-3068, 1990.

[3] M. Johnson, "Nonbolometric photoresponse of $YBa_2Cu_3O_{7-\delta}$ films," *Appl. Phys. Lett.*, Vol. 59, p. 1371-1373, 1991.

[4] A. D. Semenov, G. N. Goltsman, I. G. Gogidze, A. V. Sergeev, E. M. Gershenzon, P. T. Lang, and K. F. Renk, "Subnanosecond photoresponse of a YBaCuO thin-film to infrared and visible radiation by quasi-particle induced suppression of superconductivity," *Appl. Phys. Lett.*, Vol. 60, p. 903-905, 1992.

[5] F. A. Hegmann and J. S. Preston, "Origin of the fast photoresponse of epitaxial $YBa_2Cu_3O_{7-\delta}$ thin-films," *Phys. Rev. B*, Vol. 48, p. 16023-16039, 1993.

[6] A. Ghis, J. C. Villegier, S. Pfister, M. Nail, and P. Gibert, "Electrical picosecond measurements of the photoresponse in YBa_2Cu_3O7-x," *Appl. Phys. Lett.*, Vol. 63, p. 551-552, 1993.

[7] W. A. Little, "Possibility of synthesizing organic superconductor," *Physical Review a-General Physics*, Vol. 134, p. 1416, 1964.

[8] W. A. Little, K. Collins, and M. J. Holcomb, "Electronic and phonon contributions to the pairing in the cuprates," *J. Supercond.*, Vol. 12, p. 89-94, 1999.

[9] M. J. Holcomb, C. L. Perry, J. P. Collman, and W. A. Little, "Thermal-difference reflectance spectroscopy of the high-temperature cuprate superconductors," *Phys. Rev. B*, Vol. 53, p. 6734-6751, 1996.

[10] M. J. Holcomb, J. P. Collman, and W. A. Little, "Thermal difference spectroscopy," *Rev. Sci. Instrum.*, Vol. 64, p. 1862-1867, 1993.

[11] M. J. Holcomb, J. P. Collman, and W. A. Little, "Optical evidence of an electronic contribution to the pairing interaction in superconducting $Tl_2Ba_2Ca2Cu_3O_{10}$," *Phys. Rev. Lett.*, Vol. 73, p. 2360-2363, 1994.

[12] C. J. Stevens, D. Smith, C. Chen, J. F. Ryan, B. Podobnik, D. Mihailovic, G. A. Wagner, and J. E. Evetts, "Evidence for two-component high-temperature superconductivity in the femtosecond optical response of $YBa_2Cu_3O_{7-\delta}$," *Phys. Rev. Lett.*, Vol. 78, p. 2212-2215, 1997.

[13] V. J. Emery, S. A. Kivelson, and H. Q. Lin, "Phase-separation in the T-J model," *Phys. Rev. Lett.*, Vol. 64, p. 475-478, 1990.

[14] D. Poilblanc and T. M. Rice, "Charged solitons in the Hartree-Fock approximation to the large-U Hubbard model," *Phys. Rev. B*, Vol. 39, p. 9749-9752, 1989.

[15] E. Fatuzzo and W. J. Merz, *Ferroelectricity*. 1967, New York: John Wiley & Sons.

[16] W. J. Merz, "Switching time in ferroelectric $BaTiO_3$ and its dependence on crystal thickness," *J. Appl. Phys.*, Vol. 27, p. 938-943, 1956.

[17] H. L. Stadler and Zachmani.Pj, "Nucleation and growth of ferroelectric domains in $BaTiO_3$ at Fields from 2 to 450 kV/cm," *J. Appl. Phys.*, Vol. 34, p. 3255-&, 1963.
[18] J. F. Scott, "Limitations on ULSI-FeRAMs," *Ieice T Electron*, Vol. E81C, p. 477-487, 1998.
[19] J. F. Scott, "The physics of ferroelectric ceramic thin films for memory applications," *Ferroelectrics Review*, Vol. 1, p. 1-129, 1998.
[20] P. K. Larsen, G. L. M. Kampschoer, M. B. van der Mark, and M. Klee. *Ultrafast polarization switching of lead zirconate titanate thin films.* in *Eighth IEEE International Symposium on Applications of Ferroelectrics.* 1992.
[21] P. K. Larsen, R. Cuppens, and G. J. M. Dormans, *Pulse switching characterization of ferroelectric thin films*, in *Science and Technology of Electronic Thin Films*, O. Auciello and R. Waser, Editors. 1995, Kluwer Academic: Dodrecht. p. 201-221.
[22] H. K. Onnes, *Leiden Comm.*, Vol. 120b, 122b, 124c, p., 1911.
[23] W. Meissner and R. Ochsenfeld, *Naturwissenschaften*, Vol. 21, p. 787, 1933.
[24] C. J. Gorter and H. B. G. Casimir, *Z. Phys.*, Vol. 35, p. 963, 1934.
[25] L. N. Cooper, "Bound electron pairs in a degenerate fermi gas," *Phys. Rev.*, Vol. 104, p. 1189-1190, 1956.
[26] J. Bardeen, L. N. Cooper, and J. R. Schrieffer, "Theory of superconductivity," *Phys. Rev.*, Vol. 108, p. 1175-1204, 1957.
[27] M. K. Wu, J. R. Ashburn, C. J. Torng, P. H. Hor, R. L. Meng, L. Gao, Z. J. Huang, Y. Q. Wang, and C. W. Chu, "Superconductivity at 93-K in a new mixed-phase Y-Ba-Cu-O compound system at ambient pressure," *Phys. Rev. Lett.*, Vol. 58, p. 908-910, 1987.
[28] S. Hikami, T. Hirai, and S. Kagoshima, "High transition-temperature tuperconductor - Y-Ba-Cu Oxide," *Jpn. J. Appl. Phys.*, Vol. 26, p. L314-L315, 1987.
[29] Z. X. Zhao, L. Q. Chen, Q. S. Yang, Y. H. Huang, G. H. Chen, R. M. Tang, G. R. Liu, C. G. Cui, L. Chen, L. H. Wang, S. Q. Guo, S. L. Li, and J. Q. Bi, "Superconductivity above liquid-nitrogen temperature in Ba-Y-Cu Oxides," *Kexue Tongbao*, Vol. 32, p. 661-664, 1987.
[30] P. Dai, B. C. Chakoumakos, G. F. Sun, K. W. Wong, Y. Xin, and D. F. Lu, "Synthesis and neutron powder diffraction study of the superconductor $HgBa_2Ca_2Cu_3O_{8+\delta}$ by Tl substitution," *Physica C*, Vol. 243, p. 201-206, 1995.
[31] B. Oh, R. H. Koch, W. J. Gallagher, V. Foglietti, G. Koren, A. Gupta, and W. Y. Lee, "YBaCuO input coils with low Tc and high-Tc squids," *Appl. Phys. Lett.*, Vol. 56, p. 2575-2577, 1990.
[32] Z. Y. Shen, *High temperature superconducting microwave circuits.* 1994: Artech House.
[33] M. C. Nuss, P. M. Mankiewich, R. E. Howard, B. L. Straughn, T. E. Harvey, C. D. Brandle, G. W. Berkstresser, K. W. Goossen, and P. R. Smith, "Propagation of terahertz bandwidth electrical pulses on $YBa_2Cu_3O_{7-\delta}$ transmission-lines on lanthanum aluminate," *Appl. Phys. Lett.*, Vol. 54, p. 2265-2267, 1989.
[34] W. L. Cao, Y. Q. Liu, C. H. Lee, S. N. Mao, X. X. Xi, and T. Venkatesan, "Nanosecond Inductive Energy Storage Pulsed Power System using YBCO

superconductor opening switches," *Ieee Photonic Tech L*, Vol. 5, p. 109-111, 1993.

[35] M. Tonouchi, M. Tani, Z. Wang, K. Sakai, N. Wada, and M. Hangyo, "Terahertz emission study of femtosecond time-transient nonequilibrium state in optically excited $YBa_2Cu_3O_{7-\delta}$ thin films," *Jpn. J. Appl. Phys.*, Vol. 35, p. L1578-L1581, 1996.

[36] M. Tonouchi, M. Tani, Z. Wang, K. Sakai, S. Tomozawa, M. Hangyo, Y. Murakami, and S. I. Nakashima, "Ultrashort electromagnetic pulse radiation from YBCO thin films excited by femtosecond optical pulse," *Japanese Journal of Applied Physics Part 1-Regular Papers Short Notes & Review Papers*, Vol. 35, p. 2624-2632, 1996.

[37] L. R. Testardi, "Destruction of superconductivity by laser light," *Phys. Rev. B*, Vol. 4, p. 2189-&, 1971.

[38] P. M. W. French, "Ultrafast solid-state lasers," *Contemp. Phys.*, Vol. 37, p. 283-301, 1996.

[39] A. J. Demaria, D. A. Stetser, and H. Heynau, "Self mode-locking of lasers with saturable absorbers - (regenerative pulse oscillator bleachable dyes E)," *Appl. Phys. Lett.*, Vol. 8, p. 174-&, 1966.

[40] C. V. Shank and E. P. Ippen, "Subpicosecond kilowatt pulses from a mode-locked cw dye laser," *Appl. Phys. Lett.*, Vol. 24, p. 373-375, 1974.

[41] R. L. Fork, C. H. B. Cruz, P. C. Becker, and C. V. Shank, "Compression of optical pulses to 6 femtoseconds by using cubic phase compensation," *Opt. Lett.*, Vol. 12, p. 483-485, 1987.

[42] A. J. Hand, "Study confirms attosecond pulses," *Photon Spectra*, Vol. 34, p. 28-+, 2000.

[43] P. M. Paul, E. S. Toma, P. Breger, G. Mullot, F. Auge, P. Balcou, H. G. Muller, and P. Agostini, "Observation of a train of attosecond pulses from high harmonic generation," *Science*, Vol. 292, p. 1689-1692, 2001.

[44] N. A. Papadogiannis, B. Witzel, C. Kalpouzos, and D. Charalambidis, "Observation of attosecond light localization in higher order harmonic generation," *Phys. Rev. Lett.*, Vol. 83, p. 4289-4292, 1999.

[45] D. E. Spence, P. N. Kean, and W. Sibbett, "60-fsec pulse generation from a self-mode-locked Ti:sapphire laser," *Opt. Lett.*, Vol. 16, p. 42-44, 1991.

[46] U. Morgner, F. X. Kartner, S. H. Cho, Y. Chen, H. A. Haus, J. G. Fujimoto, E. P. Ippen, V. Scheuer, G. Angelow, and T. Tschudi, "Sub-two-cycle pulses from a Kerr-lens mode-locked Ti :sapphire laser," *Opt. Lett.*, Vol. 24, p. 411-413, 1999.

[47] M. J. Weber, D. Milam, and W. L. Smith, "Non-linear refractive-index of glasses and crystals," *Opt Eng*, Vol. 17, p. 463-469, 1978.

[48] N. H. Rizvi, P. M. W. French, and J. R. Taylor, "Generation of 33-fs pulses from a passively mode-locked Cr^{3+}:$LiSrAlF_6$ Laser," *Opt. Lett.*, Vol. 17, p. 1605-1607, 1992.

[49] R. L. Fork, O. E. Martinez, and J. P. Gordon, "Negative dispersion using pairs of prisms," *Opt. Lett.*, Vol. 9, p. 150-152, 1984.

[50] T. B. Norris, "Femtosecond pulse amplification at 250 Khz with a Ti:sapphire regenerative amplifier and application to continuum generation," *Opt. Lett.*, Vol. 17, p. 1009-1011, 1992.

[51] R. B. Laibowitz, R. H. Koch, P. Chaudhari, and R. J. Gambino, "Thin Superconducting Oxide-Films," *Physical Review B*, Vol. 35, p. 8821-8823, 1987.
[52] R. M. Silver, A. B. Berezin, M. Wendman, and A. L. Delozanne, "As-deposited superconducting Y-Ba-Cu-O thin-films on Si, Al_2O_3, and $SrTiO_3$ substrates," *Appl. Phys. Lett.*, Vol. 52, p. 2174-2176, 1988.
[53] E. S. Hellman, D. G. Schlom, N. Missert, K. Char, J. S. Harris, M. R. Beasley, A. Kapitulnik, T. H. Geballe, J. N. Eckstein, S. L. Weng, and C. Webb, "Molecular-beam epitaxy and deposition of high-Tc superconductors," *J. Vac. Sci. Technol. B*, Vol. 6, p. 799-803, 1988.
[54] J. Kwo, T. C. Hsieh, R. M. Fleming, M. Hong, S. H. Liou, B. A. Davidson, and L. C. Feldman, "Structural and superconducting properties of orientation-ordered $YBa_2Cu_3O_{7-X}$ films prepared by Molecular-Beam Epitaxy," *Phys. Rev. B*, Vol. 36, p. 4039-4042, 1987.
[55] M. Hong, S. H. Liou, J. Kwo, and B. A. Davidson, "Superconducting Y-Ba-Cu-O oxide-films by sputtering," *Appl. Phys. Lett.*, Vol. 51, p. 694-696, 1987.
[56] Y. Hakuraku, S. Higo, and T. Ogushi, "Highly oriented Bi(Pb)-Sr-Ca-Cu-O superconducting thin-films by magnetron sputtering of a single target," *Appl. Phys. Lett.*, Vol. 55, p. 1569-1571, 1989.
[57] X. X. Xi, G. Linker, O. Meyer, E. Nold, B. Obst, F. Ratzel, R. Smithey, B. Strehlau, F. Weschenfelder, and J. Geerk, "Superconducting and structural-properties of YBaCuO thin-films deposited by inverted cylindrical magnetron sputtering," *Z. Phys. B Con. Mat.*, Vol. 74, p. 13-19, 1989.
[58] Y. Suzuki, D. Lew, A. F. Marshall, M. R. Beasley, and T. H. Geballe, "Anisotropic transport-properties of in-plane-aligned a-axis $YBa_2Cu_3O_7$ films," *Phys. Rev. B*, Vol. 48, p. 10642-10645, 1993.
[59] K. Zhang, E. P. Boyd, B. S. Kwak, A. C. Wright, and A. Erbil, "Metalorganic chemical vapor-deposition of $Tl_2CaBa_2Cu_2O_y$ superconducting thin-films on sapphire," *Appl. Phys. Lett.*, Vol. 55, p. 1258-1260, 1989.
[60] C. S. Chern, J. Zhao, Y. Q. Li, P. Norris, B. Kear, and B. Gallois, "Insitu growth of $YBa_2Cu_3O_{7-X}$ high-Tc superconducting thin-films directly on sapphire by plasma-enhanced metalorganic chemical vapor-deposition," *Appl. Phys. Lett.*, Vol. 57, p. 721-723, 1990.
[61] T. Sugimoto, M. Yoshida, K. Yamaguchi, K. Sugawara, Y. Shiohara, and S. Tanaka, "Epitaxial-growth of Bi-Sr-Ca-Cu-O superconducting thin-films by metalorganic chemical vapor-deposition," *Appl. Phys. Lett.*, Vol. 57, p. 928-930, 1990.
[62] C. S. Chern, J. Zhao, Y. Q. Li, P. Norris, B. Kear, B. Gallois, and Z. Kalman, "Epitaxial thin-films of $YBa_2Cu_3O_{7-X}$ on $LaAlO_3$ substrates deposited by plasma-enhanced metalorganic chemical vapor-deposition," *Appl. Phys. Lett.*, Vol. 58, p. 185-187, 1991.
[63] D. Dijkkamp, T. Venkatesan, X. D. Wu, S. A. Shaheen, N. Jisrawi, Y. H. Minlee, W. L. Mclean, and M. Croft, "Preparation of Y-Ba-Cu Oxide superconductor thin-films using pulsed laser evaporation from high-Tc bulk material," *Appl. Phys. Lett.*, Vol. 51, p. 619-621, 1987.

[64] E. V. Pechen, A. V. Varlashkin, S. I. Krasnosvobodtsev, B. Brunner, and K. F. Renk, "Pulsed-laser deposition of smooth high-Tc superconducting films using a synchronous velocity filter," *Appl. Phys. Lett.*, Vol. 66, p. 2292-2294, 1995.

[65] B. Holzapfel, B. Roas, L. Schultz, P. Bauer, and G. Saemann-Ischenko, "Off-axis laser deposition of $YBa_2Cu_3O_{7-\delta}$ thin films," *Appl. Phys. Lett.*, Vol. 61, p. 3178, 1992.

[66] H. M. Smith and A. F. Smith, "Vacuum deposited thin films using a ruby laser," *Appl. Opt.*, Vol. 4, p. 147, 1965.

[67] C. P. Wen, "Coplanar waveguide: a surface strip transmission line suitable for nonreciprocal gyromagnetic device applications," *IEEE Trans. Microwave Theory Tech.*, Vol. 17, p. 1087, 1969.

[68] K. C. Gupta, R. Grag, I. Bahl, and P. Bhartia, *Microstrip lines and slotlines*, Second ed. 1996, Boston, MA: Artech House.

[69] A. D. Semenov, R. S. Nebosis, Y. P. Gousev, M. A. Heusinger, and K. F. Renk, "Analysis of the nonequilibrium photoresponse of superconducting films to pulsed radiation by use of a 2-temperature model," *Phys. Rev. B*, Vol. 52, p. 581-590, 1995.

[70] J. F. Golding, ed. *Measuring oscilloscopes*. 1971, Iliffe: London.

[71] A. D. Semenov, "Transient photoimpedance response of $YBa_2Cu_3O_{7-\delta}$ epitaxial films in the mixed state," *JETP*, Vol. 89, p. 552-558, 1999.

[72] N. Bluzer, "Temporal relaxation of nonequilibrium in Y-Ba-Cu-O measured from transient photoimpedance response," *Phys. Rev. B*, Vol. 44, p. 10222-10233, 1991.

[73] B. Friedl, C. Thomsen, and M. Cardona, "Determination of the Superconducting Gap in Rba2cu3o7-Delta," *Phys. Rev. Lett.*, Vol. 65, p. 915-918, 1990.

[74] M. Nahum, S. Verghese, P. L. Richards, and K. Char, "Thermal-boundary resistance for $YBa_2Cu_3O_{7-\delta}$ films," *Appl. Phys. Lett.*, Vol. 59, p. 2034-2036, 1991.

[75] A. V. Sergeev, A. D. Semenov, P. Kouminov, V. Trifonov, I. G. Goghidze, B. S. Karasik, G. N. Goltsman, and E. M. Gershenzon, "Transparency of a $YBa_2Cu_3O_{7-\delta}$ film substrate interface for thermal phonons measured by means of voltage response to radiation," *Phys. Rev. B*, Vol. 49, p. 9091-9096, 1994.

[76] H. L. Edwards, J. T. Markert, and A. L. Delozanne, "Energy-gap and surface-structure of $YBa_2Cu_3O_{7-x}$ probed by scanning tunneling microscopy," *Phys. Rev. Lett.*, Vol. 69, p. 2967-2970, 1992.

[77] R. Meservey and P. M. Tedrow, "Measurements of kinetic inductance of superconducting linear structures," *J. Appl. Phys.*, Vol. 40, p. 2028-&, 1969.

[78] A. Rothwarf and B. N. Taylor, "Measurement of recombination lifetimes in superconductors," *Phys. Rev. Lett.*, Vol. 19, p. 27-&, 1967.

[79] M. Lindgren, M. Currie, C. Williams, T. Y. Hsiang, P. M. Fauchet, R. Sobolewski, S. H. Moffat, R. A. Hughes, J. S. Preston, and F. A. Hegmann, "Intrinsic picosecond response times of Y-Ba-Cu-O superconducting photodetectors," *Appl. Phys. Lett.*, Vol. 74, p. 853-855, 1999.

[80] S. M. Anlage, B. W. Langley, G. Deutscher, J. Halbritter, and M. R. Beasley, "Measurements of the temperature-dependence of the magnetic penetration depth in $YBa_2Cu_3O_{7-\delta}$ superconducting thin-films," *Phys. Rev. B*, Vol. 44, p. 9764-9767, 1991.

[81] C. Williams, R. Adam, Q. Xie, R. Sobolewski, and O. Harnack, "Nonequilibrium kinetic inductive response of Y-Ba-Cu-O photodetectors," *Supercond. Sci. Technol.*, Vol. 12, p. 843-846, 1999.

[82] R. Sobolewski. *Ultrafast Dynamics of Nonequilibrium Quasiparticles in High-Temperature Superconductors*. in *Superconducting and Related Oxides: Physics and Nanoengineering III*. 1998. Proceedings of SPIE.

[83] A. Frenkel, M. A. Saifi, T. Venkatesan, C. L. Lin, X. D. Wu, and A. Inam, "Observation of fast nonbolometric optical-response of nongranular high-Tc $YBa_2Cu_3O_{7-X}$ superconducting thin-films," *Appl. Phys. Lett.*, Vol. 54, p. 1594-1596, 1989.

[84] M. A. Heusinger, A. D. Semenov, R. S. Nebosis, Y. P. Gousev, and K. F. Renk, "Nonthermal kinetic inductance photoresponse of thin superconducting films," *IEEE Trans. Appl. Supercond.*, Vol. 5, p. 2595-2598, 1995.

[85] J. F. Whitaker, R. Sobolewski, D. R. Dykaar, T. Y. Hsiang, and G. A. Mourou, "Propagation Model for Ultrafast Signals on Superconducting Dispersive Striplines," *IEEE Trans. Microwave Theory Tech.*, Vol. 36, p. 277-285, 1988.

[86] Y. G. Zhao, S. B. Ogale, R. Shreekala, Z. W. Dong, S. P. Pai, M. Rajeswari, T. Venkatesan, W. L. Cao, W. Lu, and C. Lee, "Laser power and temperature dependence of the transient photoimpedance response of epitaxial $YBa_2Cu_3O_{7-\delta}$ thin films," *J. Appl. Phys.*, Vol. 83, p. 1531-1535, 1998.

[87] M. Tinkham, *Introduction to Superconductivity*. 1996, New York: McGraw-Hill.

[88] A. C. Rose-Innes and E. H. Rhoderick, *Introduction to superconductivity*. Vol. 6. 1978, New York: Pergramon Press.

[89] E. Li, R. P. Sharma, S. B. Ogale, Y. G. Zhao, T. Venkatesan, J. Li, W. L. Cao, and C. H. Lee, "Sharp resonant multiplet in femtosecond optical pair-breaking spectroscopy of optimally doped, underdoped, and Zn-doped $YBa_2Cu_3O_{7-\delta}$: Transient insulating regions in the superconducting state," *Phys. Rev. B*, Vol. 65, p. 184519, 2002.

[90] Y. G. Zhao, W. L. Cao, J. J. Li, H. D. Drew, R. Shreekala, C. H. Lee, S. P. Pai, M. Rajeswari, S. B. Ogale, R. P. Sharma, G. Baskaran, and T. Venkatesan, "Unusual photon energy dependence of the Cooper pair breaking rate in $YBa_2Cu_3O_{7-\delta}$ epitaxial thin films," *J. Supercond.*, Vol. 12, p. 675-680, 1999.

[91] Y. G. Zhao, E. Li, T. Wu, S. B. Ogale, R. P. Sharma, T. Venkatesan, J. J. Li, W. L. Cao, C. H. Lee, H. Sato, and M. Naito, "Optical Cooper pair breaking spectroscopy of cuprate superconductors," *Phys. Rev. B*, Vol. 6313, p. 132507, 2001.

[92] Y. G. Zhao, T. Wu, S. B. Ogale, E. Li, R. P. Sharma, T. Venkatesan, J. J. Li, W. L. Cao, and C. H. Lee, "Optical Cooper pair breaking spectroscopy of $YBa_2Cu_{2.8}Zn_{0.2}O_{7-delta}$ thin films," *Supercond. Sci. Technol.*, Vol. 15, p. 468-471, 2002.

[93] D. Vaknin, S. K. Sinha, D. E. Moncton, D. C. Johnston, J. M. Newsam, C. R. Safinya, and H. E. King, "Antiferromagnetism in La_2CuO_{4-Y}," *Phys. Rev. Lett.*, Vol. 58, p. 2802-2805, 1987.

[94] J. M. Tranquada, D. E. Cox, W. Kunnmann, H. Moudden, G. Shirane, M. Suenaga, P. Zolliker, D. Vaknin, S. K. Sinha, M. S. Alvarez, A. J. Jacobson, and D. C. Johnston, "Neutron-diffraction determination of antiferromagnetic structure

of Cu ions in $YBa_2Cu_3O_{6+x}$ with x = 0.0 and 0.15," *Phys. Rev. Lett.*, Vol. 60, p. 156-159, 1988.

[95] G. Shirane, R. J. Birgeneau, Y. Endoh, P. Gehring, M. A. Kastner, K. Kitazawa, H. Kojima, I. Tanaka, T. R. Thurston, and K. Yamada, "Temperature-dependence of the magnetic excitations in $La_{1.85}Sr_{0.15}CuO_4$ (Tc = 33 K)," *Phys. Rev. Lett.*, Vol. 63, p. 330-333, 1989.

[96] S. W. Cheong, G. Aeppli, T. E. Mason, H. Mook, S. M. Hayden, P. C. Canfield, Z. Fisk, K. N. Clausen, and J. L. Martinez, "Incommensurate magnetic fluctuations in $La_{2-X}Sr_xCuO_4$," *Phys. Rev. Lett.*, Vol. 67, p. 1791-1794, 1991.

[97] T. E. Mason, G. Aeppli, and H. A. Mook, "Magnetic dynamics of superconducting $La_{1.86}Sr_{0.14}CuO_4$," *Phys. Rev. Lett.*, Vol. 68, p. 1414-1417, 1992.

[98] H. A. Mook, P. C. Dai, and F. Dogan, "Charge and spin structure in $YBa_2Cu_3O_{6.35}$," *Phys. Rev. Lett.*, Vol. 88, p. 97004, 2002.

[99] H. A. Mook, P. C. Dai, S. M. Hayden, G. Aeppli, T. G. Perring, and F. Dogan, "Spin fluctuations in $YBa_2Cu_3O_{6.6}$," *Nature*, Vol. 395, p. 580-582, 1998.

[100] V. Kataev, B. Rameev, B. Büchner, M. Hücker, and R. Borowski, "Slow antiferromagnetic dynamics in the low-temperature tetragonal phase of $La_{2-x}Sr_xCuO_4$ as revealed by ESR of Gd spin probes," *Phys. Rev. B*, Vol. 55, p. 3394, 1997.

[101] M. L. H. J. Zaanen, W. van Saarloos, "Charged domain-wall dynamics in doped antiferromagnets and spin fluctuations in cuprate superconductors," *Phy. Rev. B*, Vol. 53, p. 8671-8680, 1995.

[102] M. E. Simon, A. A. Aligia, C. D. Batista, E. R. Gagliano, and F. Lema, "Excitons in insulating cuprates," *Phys. Rev. B*, Vol. 54, p. R3780-R3783, 1996.

[103] E. Hanamura, N. T. Dan, and Y. Tanabe, "Excitons and two-magnon Raman scattering of the strongly correlated systems La_2CuO_4 and $YBa_2Cu_3O_6$," *Phys. Rev. B*, Vol. 62, p. 7033-7044, 2000.

[104] R. Liu, D. Salamon, M. V. Klein, S. L. Cooper, W. C. Lee, S. W. Cheong, and D. M. Ginsberg, "Novel Raman-active electronic excitations near the charge-transfer gap in insulating cuprates," *Phys. Rev. Lett.*, Vol. 71, p. 3709-3712, 1993.

[105] H. A. Mook, M. Yethiraj, G. Aeppli, T. E. Mason, and T. Armstrong, "Polarized neutron determination of the magnetic excitations in $YBa_2Cu_3O_7$," *Phys. Rev. Lett.*, Vol. 70, p. 3490-3493, 1993.

[106] R. J. McQueeney, Y. Petrov, T. Egami, M. Yethiraj, G. Shirane, and Y. Endoh, "Anomalous dispersion of LO phonons in $La_{1.85}Sr_{0.15}CuO_4$ at low temperatures," *Phys. Rev. Lett.*, Vol. 82, p. 628-631, 1999.

[107] J. P. Falck, A. Levy, M. A. Kastner, and R. J. Birgeneau, "Charge-transfer spectrum and its temperature-dependence in La_2CuO_4," *Phys. Rev. Lett.*, Vol. 69, p. 1109-1112, 1992.

[108] S. G. Han, Z. V. Vardeny, K. S. Wong, O. G. Symko, and G. Koren, "Femtosecond optical-detection of quasi-particle dynamics in high-Tc $YBa_2Cu_3O_{7-\delta}$ superconducting thin-films," *Phys. Rev. Lett.*, Vol. 65, p. 2708-2711, 1990.

[109] G. L. Eesley, J. Heremans, M. S. Meyer, G. L. Doll, and S. H. Liou, "Relaxation time of the order parameter in a high-temperature superconductor," *Phys. Rev. Lett.*, Vol. 65, p. 3445, 1990.

[110] T. Gong, L. X. Zheng, W. Xiong, W. Kula, Y. Kostoulas, R. Sobolewski, and P. M. Fauchet, "Femtosecond optical-response of Y-Ba-Cu-O thin-films - the dependence on optical frequency, excitation intensity, and electric-current," *Phys. Rev. B*, Vol. 47, p. 14495-14502, 1993.
[111] J. A. Valdmanis, G. Mourou, and C. W. Gabel, "Picosecond electrooptic sampling system," *Appl. Phys. Lett.*, Vol. 41, p. 211-212, 1982.
[112] C. H. Lee, ed. *Picosecond optoelectronic devices*. 1984, Orlando: Academic Press.
[113] D. H. Auston, "Picosecond optoelectronic switching and gating in silicon," *Appl. Phys. Lett.*, Vol. 26, p. 101-103, 1975.
[114] S. L. Huang, E. A. Chauchard, C. H. Lee, H. L. A. Hung, T. T. Lee, and T. Joseph, "On-safer photoconductive sampling of MMICS," *IEEE Trans. Microwave Theory Tech.*, Vol. 40, p. 2312-2320, 1992.
[115] K. H. Schoenbach, M. Kristiansen, and G. Schaefer, "A review of opening switch technology for inductive energy-storage," *P Ieee*, Vol. 72, p. 1019-1040, 1984.
[116] F. Z. Arye Rosen, ed. *High-Power Optically Activated Solid-State Switches*. 1994, Artech House, Boston.
[117] W. L. Cao, Y. Q. Liu, C. H. Lee, S. N. Mao, X. X. Xi, and T. Venkatesan, "Nanosecond Inductive Energy-Storage Pulsed Power-System Using Ybco Superconductor Opening Switches," *Ieee Photonics Technology Letters*, Vol. 5, p. 109-111, 1993.
[118] Y. S. Lai, E. E. Funk, W. L. Cao, C. H. Lee, Z. Y. Shen, P. Pang, D. J. Kountz, and W. L. Holstein, "Ultra-wide-band pulse generation and radiation using a high Tc superconductor opening switch," *Appl. Phys. Lett.*, Vol. 65, p. 1048-1050, 1994.
[119] O. Auciello, J. F. Scott, and R. Ramesh, "The physics of ferroelectric memories," *Phys Today*, Vol. 51, p. 22-27, 1998.
[120] J. F. Scott and C. A. P. Dearaujo, "Ferroelectric memories," *Science*, Vol. 246, p. 1400-1405, 1989.
[121] A. I. Kingon and E. R. Myers, eds. *Ferroelectric Thin Films*. Vol. 200. 1990, Material Research Society Proc.
[122] M. Alexe, C. Harnagea, D. Hesse, and U. Gosele, "Patterning and switching of nanosize ferroelectric memory cells," *Appl. Phys. Lett.*, Vol. 75, p. 1793-1795, 1999.
[123] C. S. Ganpule, A. Stanishevsky, S. Aggarwal, J. Melngailis, E. Williams, R. Ramesh, V. Joshi, and C. P. de Araujo, "Scaling of ferroelectric and piezoelectric properties in $Pt/SrBi_2Ta_2O_9/Pt$ thin films," *Appl. Phys. Lett.*, Vol. 75, p. 3874-3876, 1999.
[124] C. Harnagea, M. Alexe, J. Schilling, J. Choi, R. B. Wehrspohn, D. Hesse, and U. Gosele, "Mesoscopic ferroelectric cell arrays prepared by imprint lithography," *Appl. Phys. Lett.*, Vol. 83, p. 1827-1829, 2003.
[125] W. H. Ma, C. Harnagea, D. Hesse, and U. Gosele, "Well-ordered arrays of pyramid-shaped ferroelectric $BaTiO_3$ nanostructures," *Appl. Phys. Lett.*, Vol. 83, p. 3770-3772, 2003.

[126] I. Szafraniak, C. Harnagea, R. Scholz, S. Bhattacharyya, D. Hesse, and M. Alexe, "Ferroelectric epitaxial nanocrystals obtained by a self-patterning method," *Appl. Phys. Lett.*, Vol. 83, p. 2211-2213, 2003.
[127] J. Junquera and P. Ghosez, "Critical thickness for ferroelectricity in perovskite ultrathin films," *Nature*, Vol. 422, p. 506-509, 2003.
[128] U. Chon, K. B. Kim, H. M. Jang, and G. C. Yi, "Fatigue-free samarium-modified bismuth titanate ($Bi_{4-x}Sm_xTi_3O_{12}$) film capacitors having large spontaneous polarizations," *Appl. Phys. Lett.*, Vol. 79, p. 3137-3139, 2001.
[129] S. R. Shannigrahi and H. M. Jang, "Fatigue-free lead zirconate titanate-based capacitors for nonvolatile memories," *Appl. Phys. Lett.*, Vol. 79, p. 1051-1053, 2001.
[130] G. Asano, H. Morioka, H. Funakubo, T. Shibutami, and N. Oshima, "Fatigue-free $RuO_2/Pb(Zr,Ti)O_3/RuO_2$ capacitor prepared by metalorganic chemical vapor deposition at 395 degrees C," *Appl. Phys. Lett.*, Vol. 83, p. 5506-5508, 2003.
[131] G. S. Wang, X. J. Meng, J. L. Sun, Z. Q. Lai, J. Yu, S. L. Guo, J. G. Cheng, J. Tang, and J. H. Chu, "$PbZr_{0.5}Ti_{0.5}O_3/La_{0.5}Sr_{0.5}CoO_3$ heterostructures prepared by chemical solution routes on silicon with no fatigue polarization," *Appl. Phys. Lett.*, Vol. 79, p. 3476-3478, 2001.
[132] E. L. Colla, I. Stolichnov, P. E. Bradely, and N. Setter, "Direct observation of inversely polarized frozen nanodomains in fatigued ferroelectric memory capacitors," *Appl. Phys. Lett.*, Vol. 82, p. 1604-1606, 2003.
[133] B. S. Kang, J. G. Yoon, T. W. Noh, T. K. Song, S. Seo, Y. K. Lee, and J. K. Lee, "Polarization dynamics and retention loss in fatigued $PbZr_{0.4}Ti_{0.6}O_3$ ferroelectric capacitors," *Appl. Phys. Lett.*, Vol. 82, p. 248-250, 2003.
[134] H. Morioka, G. Asano, T. Oikawa, H. Funakubo, and K. Saito, "Large remanent polarization of 100% polar-axis-oriented epitaxial tetragonal $Pb(Zr_{0.35}Ti_{0.65})O_3$ thin films," *Appl. Phys. Lett.*, Vol. 82, p. 4761-4763, 2003.
[135] J. Ishida, T. Yamada, A. Sawabe, K. Okuwada, and K. Saito, "Large remanent polarization and coercive force by 100% 180 degrees domain switching in epitaxial $Pb(Zr_{0.5}Ti_{0.5})O_3$ capacitor," *Appl. Phys. Lett.*, Vol. 80, p. 467-469, 2002.
[136] S. N. Ryoo, S. G. Yoon, and S. H. Kim, "Improvement in ferroelectric properties of $Pb(Zr_{0.35}Ti_{0.65})O_3$ thin films using a $Pb_2Ru_2O_{7-x}$ conductive interfacial layer for ferroelectric random access memory application," *Appl. Phys. Lett.*, Vol. 83, p. 2880-2882, 2003.
[137] J. Li, H. Liang, B. Nagaraj, W. Cao, C. H. Lee, and R. Ramesh, "Application of an ultrafast photonic technique to study polarization switching dynamics of thin-film ferroelectric capacitors," *Journal of Lightwave Technology*, Vol. 21, p. 3282-3291, 2003.
[138] J. Li, B. Nagaraj, H. Liang, W. Cao, C. H. Lee, and R. Ramesh, "Ultrafast polarization switching in thin-film ferroelectrics," *Appl. Phys. Lett.*, Vol. 84, p. 1174-1176, 2004.
[139] W. J. Merz, "Domain formation and domain wall motions in ferroelectric $BaTiO_3$ single crystals," *Phys Rev*, Vol. 95, p. 690-698, 1954.
[140] E. A. Little, "Dynamic behavior of domain walls in Barium Titanate," *Phys Rev*, Vol. 98, p. 978-984, 1955.

[141] R. C. Miller and A. Savage, "Velocity of sidewise 180-degrees domain-wall motion in $BaTiO_3$ as a function of the applied electric field," *Phys Rev*, Vol. 112, p. 755-762, 1958.
[142] S. B. Hong and N. Setter, "Evidence for forward domain growth being rate-limiting step in polarization switching in < 111 >-oriented-Pb($Zr_{0.45}Ti_{0.55}$)O_3 thin-film capacitors," *Appl. Phys. Lett.*, Vol. 81, p. 3437-3439, 2002.
[143] C. H. Lee, "Picosecond optics and microwave technology," *IEEE Trans. Microwave Theory Tech.*, Vol. 38, p. 596-607, 1990.
[144] S. K. Dey, *Sol-Gel Science and PE-MOCVC of dielectric perovskite films*, in *Ferroelectric thin films: synthesis and basic properties*, O. Auciello, Editor. 1995, Gordon and Breach: Dodrecht. p. 329.
[145] C. Araujo, J. F. Scott, R. B. Godfrey, and L. Mcmillan, "Analysis of switching transients in KnO_3 ferroelectric memories," *Appl. Phys. Lett.*, Vol. 48, p. 1439-1440, 1986.
[146] I. Jenkins, *Switching dynamics in lead based ferroelectric thin films*. 2000, University of Maryland.
[147] T. K. Song, S. Aggarwal, Y. Gallais, B. Nagaraj, R. Ramesh, and J. T. Evans, "Activation fields in ferroelectric thin film capacitors: Area dependence," *Appl. Phys. Lett.*, Vol. 73, p. 3366-3368, 1998.
[148] Y. Ishibashi, "A model of polarization reversal in ferroelectrics," *J. Phys. Soc. Jpn.*, Vol. 59, p. 4148-4154, 1990.
[149] Ishibash.Y and Y. Takagi, "Ferroelectric domain switching," *J. Phys. Soc. Jpn.*, Vol. 31, p. 506-&, 1971.
[150] V. Y. Shur, E. L. Rumyantsev, S. D. Makarov, A. L. Subbotin, and V. V. Volegov, "Transient current during switching in increasing electric field as a basis for a new testing method," *Integrated Ferroelectrics*, Vol., p. 223-230, 1995.
[151] V. Y. Shur, E. L. Rumyantsev, and S. D. Makarov, "Kinetics of polarization switching in finite-size ferroelectric samples," *Physics Solid State*, Vol. 37, p. 917-919, 1995.
[152] V. Shur, E. Rumyantsev, and S. Makarov, "Kinetics of phase transformations in real finite systems: Application to switching in ferroelectrics," *J. Appl. Phys.*, Vol. 84, p. 445-451, 1998.
[153] Ishibash.Y, *Polarization reversals in ferroelectrics*, in *Ferroelectric thin films: synthesis and basic properties.*, C. Araujo, J.F. Scott, and G.W. Taylor, Editors. 1995. p. 135.
[154] P. K. Larsen, G. L. M. Kampschoer, M. J. E. Ulenaers, G. A. C. M. Spierings, and R. Cuppens, "Nanosecond switching of thin ferroelectric-films," *Appl. Phys. Lett.*, Vol. 59, p. 611-613, 1991.